Design and Optimization Methodology of Sub-dermal Electroencephalography Dry Spike-Array Electrode

by

Salam Ramy Gabran

A thesis
presented to the University of Waterloo
in fulfillment of the
thesis requirement for the degree of
Master of Applied Science
in
Electrical and Computer Engineering

Waterloo, Ontario, Canada, 2006

©Salam Ramy Gabran, 2006

Author’s Declaration

I hereby declare that I am the sole author of this thesis. This is a true copy of the thesis, including any required final revisions, as accepted by my examiners.

I understand that my thesis may be made electronically available to the public.

Salam Ramy Gabran

Abstract

Monitoring bio-electric events is a common procedure, which provides medical data required in clinical and research applications. Electrophysiological measurements are applied in diagnosis as well as evaluation of the performance of different body organs and systems, e.g. the heart, muscles and the nervous system. Furthermore, it is staple feature in operation rooms and extensive care units. The performance of the recording system is affected by the tools and instrumentation used and the bio-electrode is a key-player in electrophysiology, hence, the improvements in the electrode recording technique will be directly reflected in the system's performance in terms of the signal quality, recording duration as well as patient comfort.

In this thesis, a design methodology for micro-spike array dry bio-electrodes is introduced. The purpose of this methodology is to meet the design specifications for portable long-term EEG recording and optimize the electrical performance of the electrodes by maximizing the electrode-skin contact surface area, while fulfilling design constraints including mechanical, physiological and economical limitations. This was followed by proposing a low cost fabrication technique to implement the electrodes. The proposed electrode design has a potential impact in enhancing the performance of the current recording systems, and also suits portable monitoring and long term recording devices. The design process was aided by using a software design and optimization tool, which was specifically created for this application.

The application conditions added challenges to the electrode design in order to meet the required performance requirements. On the other hand, the required design specifications are not fulfilled in the current electrode technologies which are designed and customized only for short term clinical recordings.

The electrode theory of application was verified using an experimental setup for an electrochemical cell, but the overall performance including measuring the electrode impedance is awaiting a clinical trial.

Acknowledgements

Words are not enough for expressing my gratitude to my advisors, Dr. Magdy Salama and Dr. Ehab ElSaadany for their sincere encouragement, insight and guidance. They were consistently generous providing endless hours of their valuable time for discussions. Their encouragement, patience and trust always shed light when it was dark and charged me with motivation when mine was consumed. I am privileged for conducting research with you.

I would love to thank Dr. Charles George, and Dr. Raafat Mansour for reviewing my thesis. I am also grateful to Dr. Mansour for including me in his busy schedule for discussions as well as granting me access to the CIRFE lab.

I am indebted to the α-SiDIC group; Richard Barber for granting me access to the α-SiDIC lab, Dr. Isaac Chan for sparing me long hours of his precious time for teaching me, Mahdi Baroughi, Majid Garghi and Saeed Fathololoumi for their valuable help.

Many thanks to the CIRFE group members. Special thanks to Bill Jolley, Tania Ooagarah and Reena Al-Dahleh.

I would like to thank Dr. Mark Pritzker for granting me access to the Electrochemistry lab and Maria Huerta for her valuable help with the EIS equipment.

Many thanks to the ECE stuff members; their integrity, care and beautiful good morning smiles always charged us at the beginning of the day. Special thanks to Wendy Boles for always being supportive, patient and caring even with the last-minute requests.

Cheers and thanks to all my friends who made grad life fun and enjoyable. George Shaker for being a great friend. My fellow research group members and special thanks to Shawn and Joseph. My friends Tony, Hany, Dina, Hatem, Naghmeh, Saeed, Kamyar, Tarek and M. ElDery; you were a second family to me and I will always appreciate your friendship, encouragement and companionship.

A world of thanks to Dr. Adel Sadek for his help, motivation and encouragement.

Finally, I owe it all to my mom, dad and brother. Their endless love, unconditional sacrifice and priceless encouragement were my motivation and the foundation of my success. My family extends to my heavenly father, Lord and savior because he allowed all this to come true.

Dedication

To my mother, father and brother.

Without their unconditional love, support, sacrifice and prayers I wouldn't have gone so far.

Table of Contents

List of Figures

List of Tables

Chapter 1

Introduction

1.1 Motivation

Long-term portable electrophysiological signal recording is a medical practice required for various clinical and research application. However, current electrode technologies are not optimized for portable and long term recording applications. This requires developing a new design of bio-electrodes suitable for such applications. Moreover, improving bio-electrodes used in electrophysiological signal recording systems will be directly reflected in the system's performance in terms of the signal quality, recording duration as well as patient comfort. For instance, the electrode design can suppress electrode displacement artifacts, decrease the double layer offset voltages and expand the recording time. Improving the electrode technology and its characteristics will not only improve the performance of existing systems, but will also render the asymptotic performance parameters achievable. Moreover, the electrode design proposed in this thesis has a potential impact in enhancing the performance of the current recording systems, and also suits portable monitoring and long term recording devices.

1.2 Design specifications

The electrode design presented in this thesis is customized -but not limited- to be used with portable medical assistive device developed as a technological treatment for narcoleptic patients who suffer from a brain disorder characterized by uncontrollable sleepiness attacks accompanied by hallucinations and paralysis. This encephalon disorder requires constant monitoring of the brain activities in order to be capable of predicting potential narcolepsy attacks, which can occur during exercising the normal day chores and activities. An introduction to narcolepsy and a general view of the device design are illustrated in appendix A.

Accordingly, the thesis provides a study that identifies the design specifications which make an electrode design competent for portable and long term recording. In the following lines, a qualitative view of the design specifications is introduced. The mechanical design should minimize electrode displacement artifacts and facilitates the electrode application unlike the wet electrode technology which requires skin preparation and gel conductive application. Prolonged electrode-skin interaction must not impose health hazards related to cytotoxicity, and at the same time, should maintain the electrical characteristics of the system stable and constant. Furthermore, a portable electrode is prone to mechanical failure if misapplied by the patient or snatched while fixed to the patient's scalp; therefore, its structural design must handle the forces involved. In order to provide convenience to the patient, the electrode application should not induce pain nor cause bleeding, at the same time it should be aesthetically acceptable. Finally, an economic fabrication technology is required.

These design specifications are not fulfilled in the current wet electrode technology, which are designed and customized only for short term clinical recordings.

1.3 Contribution

The main contributions of this thesis can be summarized as:

1.3.1 Design methodology

In this thesis, a design methodology for micro-spike array dry bio-electrodes is introduced. The purpose of this methodology is to meet the design specifications for portable long-term EEG recording and optimize the electrical and clinical performance of the electrodes while fulfilling the different constraints including mechanical, physiological and economical limitations. The design process was aided by using a software design and optimization tool, which was solely created for this application.

Identifying the design specifications was based on an elaborate study of the electrode characteristics including material biocompatibility, electrochemical and corrosive responses, analyzing the electrical properties of the recording system and finally a mechanical analysis of the electrode's structure.

1.3.2 Design optimization

In order to improve the electrode performance, the design was optimized to maximize the surface area of contact between the electrode surface and the extra-cellular fluid. Accomplishing this objective will minimize the electrode-skin interface impedance which influences the electrode electrical performance. The optimization analysis identifies the optimal geometry, which will maximize the contact area while fulfilling the design constraints. A Matlab based optimizer was created and used during the design optimization.

1.3.3 Electrode design

The proposed methodology and optimization tools were used to design and optimize a set of electrodes customized for the narcolepsy assistive device illustrated in appendix A. this includes micro-fabrication recipe using micro-molding and electroplating techniques.

1.4 Thesis organization

The theory of electrophysiological measurements is introduced in chapter 2, identifying the signals to be measured, current recording technology and the recommended practices to improve the signal pick-up. Chapter 3 elaborates on conventional (contemporary) EEG electrodes and compares it to the proposed electrode technology illustrating the advantages and benefits of the new technology. The design procedure starts in chapter 4 by surveying the different parameters involved in the electrode design. This aims to construct the constraints and design guidelines. This chapter is divided into sections, exploring the physiological, cytotoxic, mechanical and geometrical parameters. Chapter 5 presents the electrical analysis and modeling of the electrode designed and the fabrication procedures are briefed in chapter 6. The work done in this thesis is highlighted in Figure 1.1. And finally, the conclusion at chapter 7 summing up the electrode design and comparing it to other designs highlighting the improvement introduced by the design optimization methodology presented in the thesis.

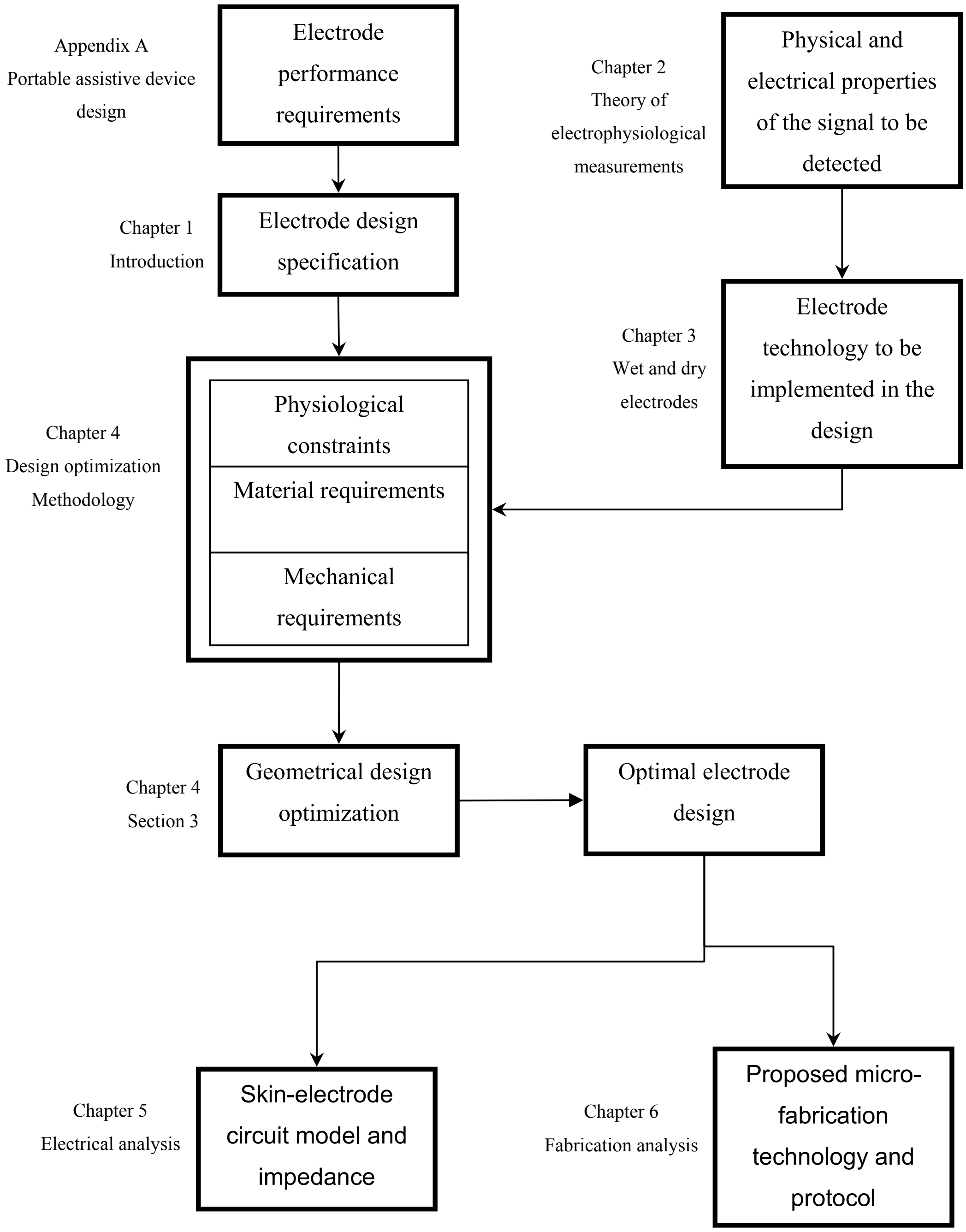

Figure 1.1 – Thesis organization

Chapter 2

Theory of electrophysiological measurements

2.1 Theory of electrophysiological measurements

2.1.1 Introduction

Brain bioelectric activity is a result of chemical reactions which convert the chemical energy into electrical form. These reactions produce ionic currents in the nerve cells where each cell is a single lumped dipole source. The number of nerve cells building the brain is estimated to be in the order of 10^{11} 1]. Because the nerve cells are densely packed, consequently; in electrophysiology the conducting medium extends continuously to create a volume conductor and a volume dipole moment density function can be defined. This continuity extends to include the capacitance which is localized to cellular membranes, however, it extends continuously in multi-cellular formations throughout a three-dimensional region to form a distributed capacitance.

2.1.2 Resting and action potentials

An action potential is a wave of electrical discharge that travels along the membrane of cells carrying fast internal messages between tissues. They result from ion flow through voltage gated channels. The number of open channels changes as the membrane potential changes and thus the membrane conductance changes as well. Action potentials are information carriers which decode the information in the frequency of action potential and a firing pattern of nerve cells is generated. Generation and encoding of action potential occurs in the dendritic and somatic (cell body) portion of neurons, while axonal membranes merely propagate a series of action potentials.

The membrane of a cell has a selective permeability to different ions and this leads to unequal exchange of ions across it. The result is a net transfer of charge into the membrane capacitance and the consequent establishment of a membrane electric field. A state of equilibrium is achieved yielding a resting potential which is a potential difference across the membrane with the negative polarity inside the membrane and the positive polarity outside. The resting potential across the cell membrane ranges from 60 to 100mV.
Ionic current excitation changes the permeability characteristics of the cell membrane leading to reversing the potential across the cell membrane and the cell is depolarized creating an action potential of approximately 20 mV.

Finally, the ionic currents decay and a steady state is reached again where the cell membrane is repolarized to the original ionic concentration. In nerve cells, the action potential is a 1 msec spike.

2.1.3 Volume Source in an infinite, homogeneous volume conductor

The bioelectric activity of nerve and muscle cells produces a non-conservative impressed current density $\overline{J^i}(x,y,z,t)$ due to the conversion of energy from chemical to electrical form. The elements forming this bioelectric source perform as electric current dipoles and the impressed current density is equal to the volume dipole moment density of the source. Outside the region of active cells $\overline{J^i}$ drops to zero [1].

An infinite and homogeneous volume conductor with conductivity σ will establish an electric field $\overline{E}$ and conduction current $\sigma\overline{E}$. This results in a total current density of [2]:

$$\overline{J} = \overline{J^i} + \sigma\overline{E} \tag{2.1}$$

where $\sigma\overline{E}$ is the return current which avoids buildup of charges due to the source current.

The electric field $\overline{E}$ is quasistatic and can be instantaneously expressed as the negative gradient of potential Φ :

$$\overline{J} = \overline{J^i} - \sigma\nabla\Phi \tag{2.2}$$

The tissue capacitance is very small and will be neglected, consequently; charges redistribution is instantaneous to source changes. Since the charge density is zero, thus the divergence of $\overline{J}$ (rate of change of the charge density) is zero as well, and equation 2.2 reduces to Poisson's equation:

$$\nabla\cdot\overline{J^i} = \nabla\cdot\sigma\nabla\Phi + \nabla\cdot\overline{J} = \sigma\nabla^2\Phi \tag{2.3}$$

where $\nabla.\overline{J^i}$ is the source function.

For a uniform and infinite region, the solution of equation 2.3 for the scalar function $\sigma\overline{E}$ is [3]:

$$4.\pi.\sigma.\Phi = -\int_{\upsilon}\left(\frac{1}{r}\right)\nabla\cdot\overline{J^i}.d\upsilon \tag{2.4}$$

The source element $-\nabla.\overline{J^i}.d\nu$ in equation 2.4 is a point source, and sets up a field $-\nabla.\overline{J^i}$ which is defined to be the flow source density (IF). Equation 2.4 can be transformed to derive the field solution for points outside the region occupied by the volume source [3]. The result is a representation of the potential distribution Φ caused by bioelectric source $\overline{J^i}$ within an infinite, homogeneous volume conductor with conductivity σ :

$$4.\pi.\sigma.\Phi = \int_{\upsilon}\overline{J^i}\cdot\nabla\left(\frac{1}{r}\right).d\upsilon \tag{2.5}$$

In equation 2.5, $\overline{J^i}.d\nu$ behaves as a dipole element producing a field varying as its dot product with $\nabla\left(\frac{1}{r}\right)$, and hence $-\nabla.\overline{J^i}.d\nu$ can be considered a volume dipole density.

2.1.4 Volume Source in an Inhomogeneous Volume Conductor

To deal with inhomogeneousities, the volume conductor will be broken down into a finite assembly of homogeneous, resistive, and isotropic regions each is defined with a boundary S_j. In this case, the current density $-\nabla.\overline{J^i}.d\nu$ is linearly related to the electric field intensity $-\nabla.\overline{J^i}.d\nu$ [4] and both the electric potential Φ and the normal component of the current density are continuous on these boundaries:

$$\Phi'\left(S_j\right) = \Phi''\left(S_j\right) \tag{2.6}$$

$$\Phi_j^{'}\nabla\Phi^{'}\left(S_j\right)\square\overline{n_j} = \sigma_j^{''}\Phi^{''}\left(S_j\right)\square\overline{n_j} \tag{2.7}$$

where the primed and double-primed notations represent the opposite sides of the boundary and $\overline{n_j}$ is directed from the primed region to the double-primed one.

If $d\upsilon$ is a volume element, and Ψ and Φ are two scalar functions in each homogeneous region, it follows from Green's theorem [5] that:

$$\sum_j \int_{S_j} \left[\sigma_j^{'}\left(\Psi^{'}\nabla\Phi^{'} - \Phi^{'}\nabla\Psi^{'}\right) - \sigma_j^{''}\left(\Psi^{''}\nabla\Phi^{''} - \Phi^{''}\nabla\Psi^{''}\right)\right].d\overline{S_j} = \sum_j \int_{\upsilon_j} \left(\Psi\nabla\square\sigma_j\nabla\Phi - \Phi\nabla\square\sigma_j\nabla\Psi\right).d\upsilon_j \tag{2.8}$$

Taking Φ is the electric potential, and $\Psi = \frac{1}{r}$ to be the reciprocal of the distance from an arbitrary field point to the element of volume in the integration. Then substituting equations 2.3, 2.6, and 2.7 into equation 2.8 [6], the result is a formula which expresses the electric potential in an inhomogeneous volume conductor containing internal volume sources:

$$4.\pi.\sigma.\Phi\left(r\right) = \int_{\upsilon} \overline{J^i}\square\nabla\left(\frac{1}{r}\right).d\upsilon + \sum_j \int_{S_j} \left(\sigma_j^{''} - \sigma_j^{'}\right).\Phi\nabla\left(\frac{1}{r}\right)\square d\overline{S_j} \tag{2.9}$$

The first term in equation 2.9 is identical to equation 2.5, $\int_{\nu} \overline{J^i}.\nabla\left(\frac{1}{r}\right).d\nu$ which represents the contribution of the volume source. While the effect of inhomogeneities is introduced by $\left(\sigma_j^{''} - \sigma_j^{'}\right).\Phi\overline{n_j}$, this is an equivalent double layer source in the direction $\overline{n_j}$ normal to the surface. Equation 2.9 can be written as:

$$4.\pi.\sigma.\Phi\left(r\right)=\int_{\upsilon}\overline{J^{i}}\square\nabla\left(\frac{1}{r}\right).d\upsilon+\sum_{j}\int_{S_j}\left(\sigma_{j}^{''}-\sigma_{j}^{'}\right).\Phi\overline{n_{j}}\square\nabla\left(\frac{1}{r}\right)d\overline{S_{j}} \tag{2.10}$$

Equation 2.10 exhibits two field sources. The first expression involving $\overline{J_i}$ that represents the contribution of volume source density which is considered the primary source. While the second term is the surface source density which represents the contribution of the inhomogeneities and is invoked by the volume source thus it is considered a secondary source.

2.1.5 Discussion

The bioelectric impressed current density $\overline{J_i}$ associated with neuronal activation produces an electric field, which can be measured on the surface of the head or directly on the brain tissue. This electric field is described by equation 2.10. For the EEG, the impressed current density results from the action of chemical transmitters on postsynaptic cortical neurons. Due to the complexity of brain structure and its electrophysiological behavior, the source function $\overline{J_i}$ can not be evaluated qualitatively from equation 2.10. On the other hand, it is possible to evaluate the source function for the electrocardiogram (ECG) and electromyogram (EMG). As a result, clinical electroencephalogram (EEG) is empirical and the quantitative EEG is based on a statistical treatment [7]. And consequently, a clinical trial is required to verify the overall electrode performance.

2.2 The Electroencephalogram (EEG)

2.2.1 Introduction

Electroencephalography is the neurophysiologic exploration of the electrical activity of the brain by recording the spatio-temporal average of the synchronous electrical activity of radially orientated neurons in the cerebral cortex [8]. These complex patterns are generated by the extra-cellular current created as a result of the graded potentials on the dendrites of neurons in the cerebral cortex and other parts of the brain.

Another form of EEG recordings is detecting the evoked responses caused by external stimulation to any of the body senses. These patterns appear as superimposed disturbances in the EEG pattern. Being repeatable, it is easy to distinguish the evoked responses from the remainder of EEG activity and from the noise. Unlike ECG, associating an EEG recording with a single electrical phenomenon within the brain can not be done, because the recordings represent a summation of electrical activities of a large number of individual neurons.

2.2.2 EEG Electrical properties

The EEG is a non-periodic waveform with amplitude that ranges between 1mV to 2mV when measured on the surface of the brain and drops to a range between 10μV to 100μV when measured on the scalp. The bandwidth occupied by the EEG signal starts at a near DC frequency of 0.5Hz and extends to 120Hz.

EEG patterns are dependant on the subject. Among the factors that influence the EEG spectrum is the age of the subject. The EEG amplitude decreases as age increases and this is due to the thickness of the skull which is a main factor which adds to the EEG path impedance. Therefore, automated EEG recording and analysis must include training phase to adopt the system to the patient's EEG pattern features.

Comparing the electroencephalogram to other electrophysiological signals, including the electrocardiogram (ECG), electromyogram (EMG) and the electro-oculogram (EOG) as presented in table 2.1 illustrates that the EEG has the lowest amplitude and thus, it is more susceptible to noise and artifacts.

Table 2.1– Electrophysiological signals

Signal	Frequency range (Hz)	Amplitude range(mV)
EEG	0.1 – 80	0.001 – 1
ECG	0.01 – 100	0.05 – 3
EOG	0.01 – 10	0.001 – 0.3
EMG	50 – 3000	0.01 – 100

2.2.3 EEG Spectrum [9] [10]

The frequency content of the EEG patterns is more informative than the amplitude information. Moreover, the phase relationships between similar EEG patterns from different parts of the brain are of great interest. Consequently, the EEG spectrum was divided into distinct frequency bands [11] as shown in Table 2.2 to be manipulated and analyzed in the frequency domain using spectral analysis techniques.

Table 2.2 – EEG spectrum

	Frequency range	Voltage range	
Delta δ	0.5 → 4Hz	Less than 100μV peak to peak	Strongest over the central region. Indication of deep sleep and unconscious states.
Theta θ	4 → 8Hz	Less than 100μV peak to peak	Strongest over the central region. Accompanies feelings of emotional stress.
Mu μ	9Hz		Associated with physical movement and intention to move.
Berger	10Hz		Eyes are closed and person is relaxed; creative thought processes.
Alpha α	8 →13Hz	Less than 10μV peak to peak	Arise from posterior part of the brain in the waking person with eyes closed. Very relaxing, opening eyes and focusing attention reduces alpha waves. Strong Alpha can generate explosions of imagery, grids, squares etc. Also found at onset of sleep
Beta β	13 →22Hz	Less than 20μV peak to peak	Over entire brain but predominant over the central region at rest. High states of wakefulness and desynchronized alpha patterns produce beta waves.
	14Hz		Micro-sleep and micro seizures in some people.
	18Hz		Threshold of the three major sensory systems, sight, sound, touch
Gamma γ	22 → 50Hz	Less than 2μV peak to peak	Results from attention or sensory stimulation.
	24Hz		At this flicker rate on TV, films, screens, 5% of people feel very strange
	40Hz		Found in hypnosis (Gruzelier 2001)
Lambda λ	60 → 120Hz		

2.2.4 EEG diagnosis

EEG signals are associated with awareness and consciousness levels. An increase in the activity is reflected in the detected EEG spectrum as its frequency is shifted to higher levels with a drop in the amplitude. A drop in the dominant frequency indicates sleep and dreaming evokes rapid eye movement (REM) patterns. Deep sleep is characterized by large and slow deflections delta waves. Different waveforms representing sleep stages are shown in figure 2.1.

2.2.5 Applications of EEG in research and clinical venues [12]

The EEG is used extensively in different clinical areas [13] which include neurology, neurosurgery, anesthesiology, psychiatry and pediatrics. The EEG signal can be used to:

- Monitor organic brain disease and diagnose mental disorder.
- Monitor alertness, coma and brain death.
- Locate areas of damage following head injury, stroke or tumor.
- Monitor cognitive engagement (alpha rhythm).
- Control anesthesia depth (“servo anesthesia”).
- Investigate epilepsy and locate seizure origin.
- Monitor brain development.
- Test drugs for convulsive effects.
- Investigate sleep disorder and physiology.
- Diagnosing the newborn health status.

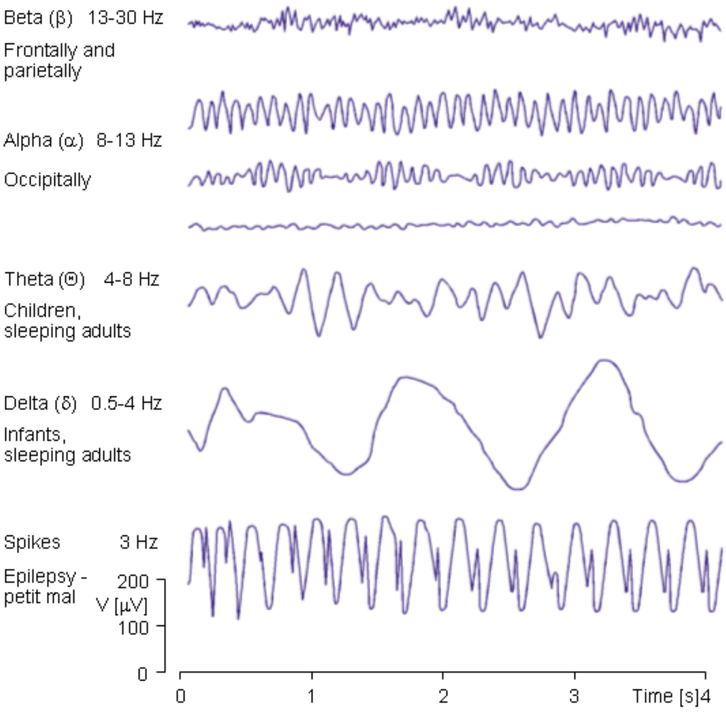

Figure 2.1 – Sleep stages

2.2.6 Artifacts

Artifacts can be considered noise signals that contaminate and distort the EEG signals. These are non-cerebral signals which are produced as a result of eye movements, muscle activity, skin stretch and drug administration. Displacement artifacts are caused by electrode dislocation.

Artifacts are different from external noise like EMI and 50/60 Hz mains interference. Usually artifacts have amplitudes comparable with the EEG signals thus diminishing or eliminating artifacts is required to improve the EEG signal quality and enhance computer-based EEG evaluation which adds to the complexity of the signal processing.

The distance between the skull and the brain and their different resistivities render the EEG data collected from any point on the human scalp susceptible to be superimposed by other activities generated within a large brain area. This spatial smearing of EEG data by volume conduction does not involve significant time delays.

One way to decrease the effect of artifacts is to shorten the electrode-preamplifier distance, and by preventing the disturbance of the electrode-skin interface [14].

2.2.7 EEG Recording locations

Recording EEG signals is not limited to the scalp but extends to different recording locations [10]:

Scalp: Wet silver/silver-chloride electrodes are used.

Sphenoidal: Alternating insulated silver and bare wire and chloride tip inserted through muscle tissue by a needle.

Nasopharyngeal: A silver rod with a silver ball at its end is inserted through the nostrils.

Electro-cortico-graphic: Direct recording from the brain surface using cotton wicks soaked in saline solution.

2.2.8 EEG Recording

When an active cell is stimulated, it acts as a constant current source and generates ionic current that is transferred through the body fluids. This current induces electrical potentials within the human body and the amplitude decays as the signal travels away from the active cell [15]. As a conclusion, by detecting the ionic currents, bio-potentials can be evaluated.

The common method to detect EEG signals is using surface electrodes placed on the scalp in a standard pattern according to the 10-20 electrode placement system. Placement of electrodes on the scalp is commonly dictated by the requirements of the measurement to be processed. Usually, the recording is obtained by placing electrodes on the scalp, usually after preparing the scalp area by light abrasion and application of a conductive gel to reduce impedance. Each electrode is connected to an input of a differential amplifier (one amplifier per electrode pair), with a voltage gain ranging between 1,000 and 100,000 (60–100 dB). The amplitude of the EEG signal is typically about 20-100µV when measured on the scalp, and about 1-2 mV when measured on the surface of the brain. As for the time domain and frequency domain requirements, the bandwidth of the received signal is limited to get optimal signal-to-noise ratio [9]. Also, due to the aperiodic nature of the EEG waveforms, EEG recording is carried for sufficiently long epochs.

2.2.9 10-20 System

The 10-20 recording system is an international standard for EEG recordings established by the international federation of EEG societies. The 10-20 system specified 21 recording spots which were expanded by the 10-10 system to 74. This is sufficient for most clinical use but sometimes it is desirable to place more electrodes in a certain area of interest. However, choosing the recording spots is based on the application in order to be as close as possible to the neurons desired for monitoring. As for portable recording, minimizing the recording spots is required. Modern versions of EEG recording systems based on the 10-20 system allow up to 345 recording spots [16] [17] (figure 2.2).

More details about electrode placement are available in appendix B.

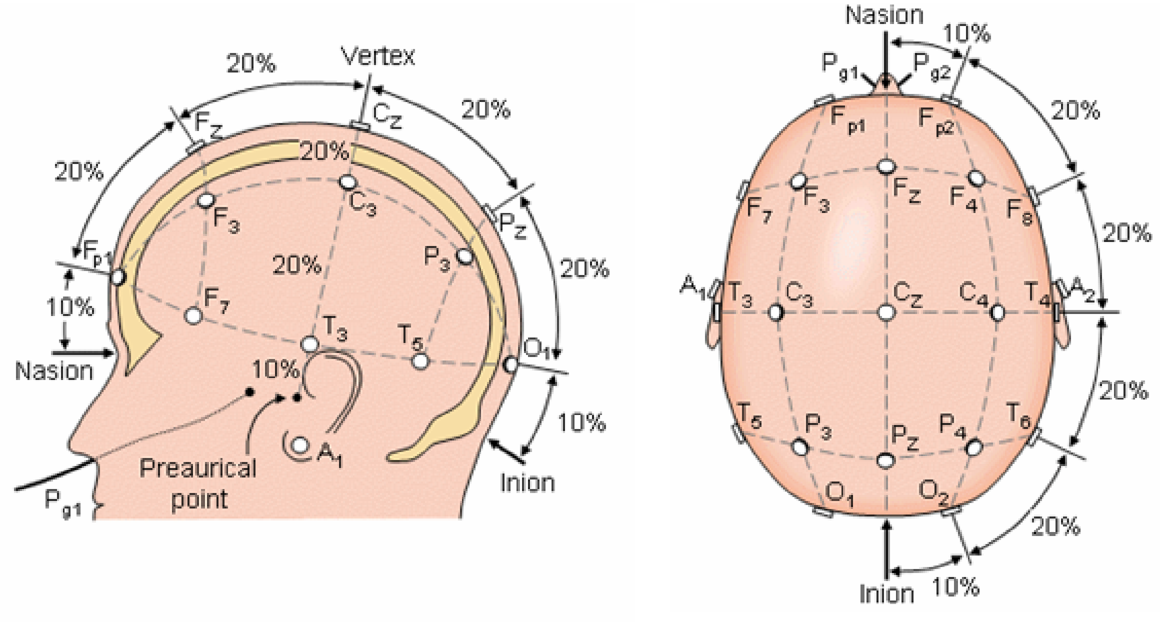

Figure 2.2 – The 10-20 system [7]

2.2.10 EEG Measurement techniques

The recorded signals making up the EEG are the differential potentials electrode pairs and this recording is done through two approaches as shown in figure 2.3:

- Referential measurement

  This technique records the potential difference between an active scalp electrode and an inactive reference electrode usually placed on the ear. The ear is used as a reference although it picks up some temporal brain activity. On the other hand, other sites like the chin and nose suffer from electrocardiogram (ECG) contamination. Theoretically, the reference spot should be at a point infinitely far away from the source of electrical activity. The problem with EEG recording is that electrodes placed too far from the brain will be influenced by ECG and movement artifacts.
- Bipolar measurement

  The potential difference is measured between two active electrodes.

2.2.11 Interference [11]

During clinical EEG recordings, usually detected EEG spectrum is susceptible to interference which can be caused by:

Electric fields: the main sources for electric field interference are the power lines in the walls, floor, ceiling and cords. Capacitance between power lines and equipment couples current into the patient, wires and machines. A high CMRR differential amplifier is required to diminish the effect of this type of interference.

Magnetic induction: Magnetic fields generated by the equipment induce voltage into the loop formed by the patient's leads. Reducing the field interference requires moving the equipment and leads or reducing the coil area by twisting the lead wires together.

In order to decrease the effect if interference which is likely to contaminate signals in a portable device, differential recording will be used utilizing bio-amplifier circuits based on instrumentation amplifier circuits.

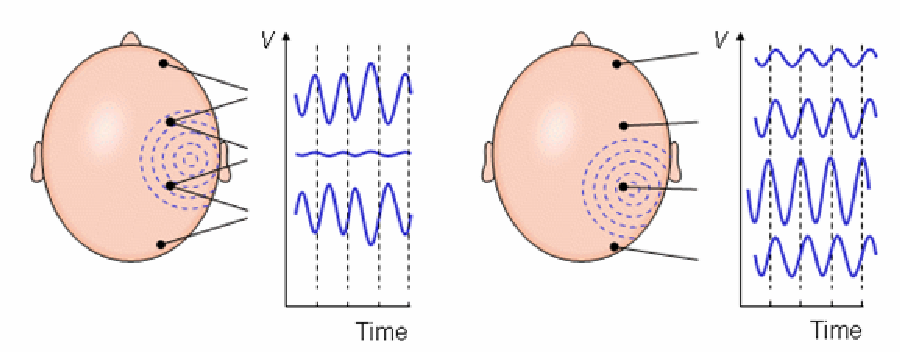

Figure 2.3 – Bipolar (left) and unipolar measurements (right) [7]

2.2.12 EEG Electrodes sensitivity distribution

The sensitivity distribution of bipolar surface electrodes on the scalp were evaluated by Rush and Driscoll [18] [19] and plotted on a concentric spherical head model in the form of lead field isopotential lines. This distribution was recalculated by Puikkonen and Malmivuo [20] but the isopotential lines of the lead field were replaced by lead field current flow lines. This display simplifies identifying the direction of the sensitivity using the lead field current flow lines. Also, the magnitude of the sensitivity can be seen from the density of the flow lines. Suihko, Malmivuo and Eskola [21] calculated the isosensitivity lines and the half-sensitivity volume which indicate the area where the lead field current density is at least one half from its maximum value.

The lead field current flow lines for different electrode placements are demonstrated in figures 2.4 through 2.9 according to the angle between the electrodes. The two electrodes are connected with 10 continuous lead field flow lines including three broken flow lines indicating the distribution in the normal plane [7] [22].

Bipolar, Close Spaced

Having a narrow angle of 20^{o} or 40^{o}, this type of placement emphasizes the area of the head immediately under the electrodes. This layout is more sensitive to dipoles oriented inline between the electrodes and the signal amplitude will generally be lower than other placements due to the small area of the head being measured.

Bipolar, Wide Spaced

Increasing the angle will cause deeper penetration into the head, and as well as emphasizing the areas immediately under the electrodes. The effect of the skull resistivity is obvious; where in a homogenous model, the sensitivity would be highly concentrated at the electrodes. But in the 180° case; the skull causes the sensitivity to be homogeneously distributed throughout the brain region. The closer the electrodes are to each other, the smaller the part of the sensitivity that locates within the brain region. As the electrodes come closer, the lead field current is routed through the skin, thus decreasing the sensitivity to the brain region and increasing the noise [7].

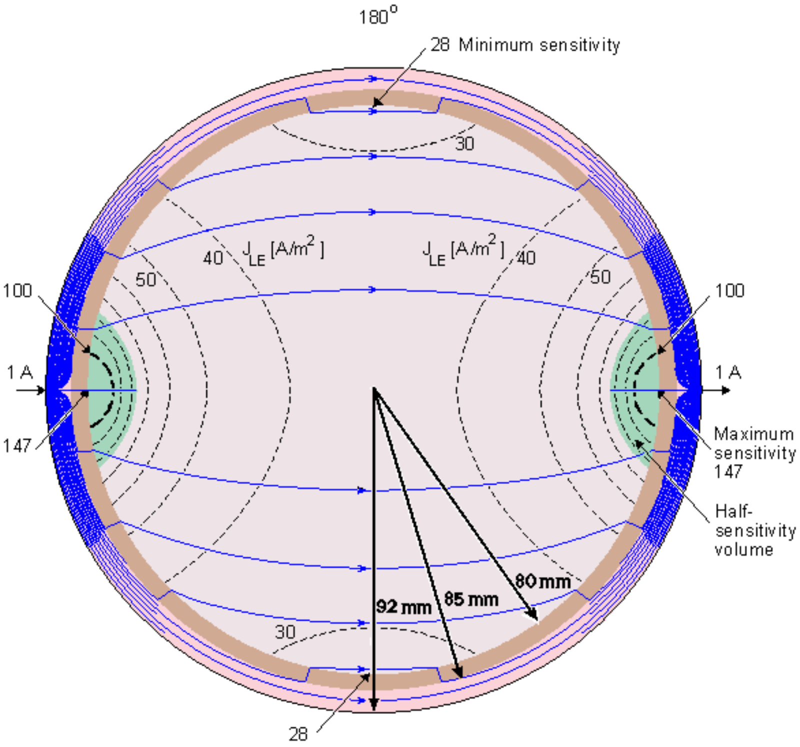

Figure 2.4 – Sensitivity distribution of EEG electrodes in the spherical head model. The electrode pair is indicated by black arrows at the surface of the scalp separated by an angle of 180° [7]

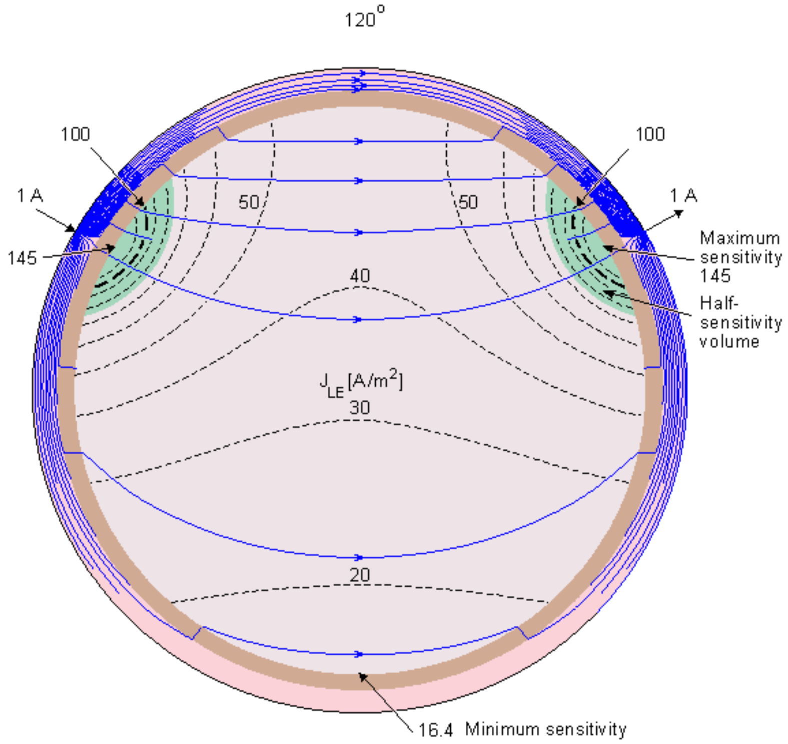

Figure 2.5 – Sensitivity distribution of EEG electrodes in the spherical head model. The electrode pair is indicated by black arrows at the surface of the scalp separated by an angle of 120° [7]

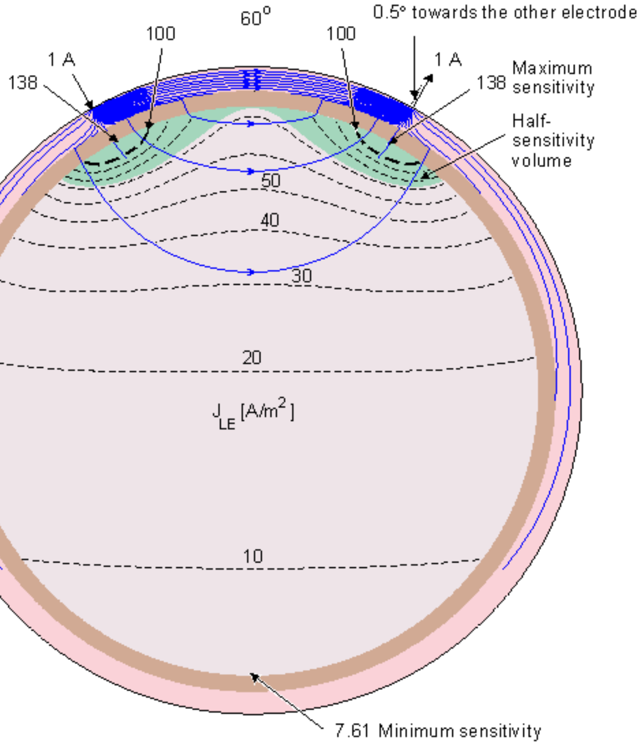

Figure 2.6 – Sensitivity distribution of EEG electrodes in the spherical head model. The electrode pair is indicated by black arrows at the surface of the scalp separated by an angle of 60° [7]

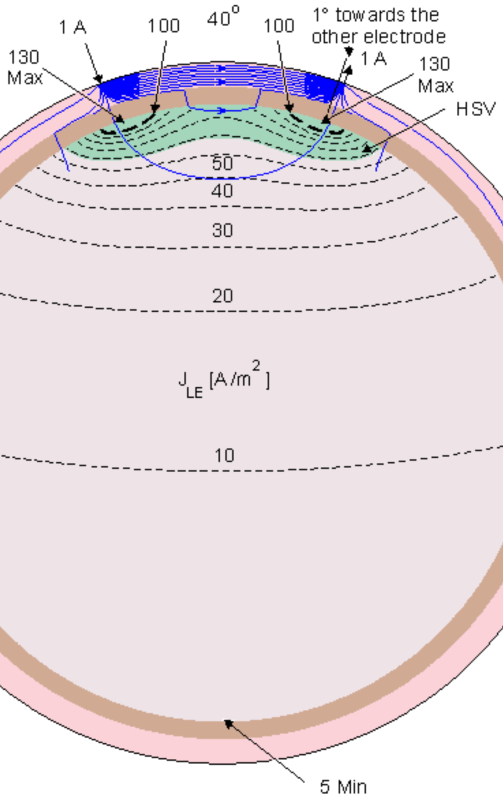

Figure 2.7 – Sensitivity distribution of EEG electrodes in the spherical head model. The electrode pair is indicated by black arrows at the surface of the scalp separated by an angle of 40° [7]

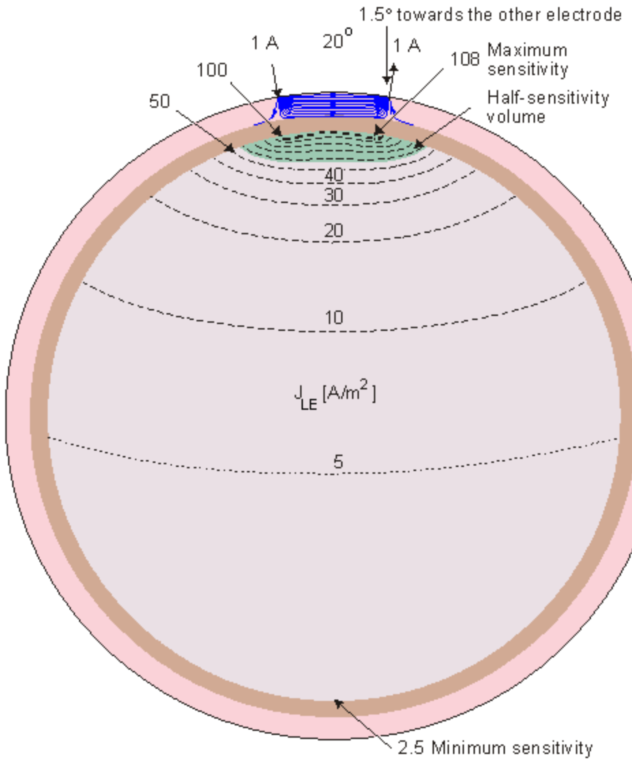

Figure 2.8 – Sensitivity distribution of EEG electrodes in the spherical head model. The electrode pair is indicated by black arrows at the surface of the scalp separated by an angle of 20° [7]

2.2.13 Discussion

EEG signals are characterized by having extremely low voltage levels and the recording technique has to maximize the voltage signal acquired and maximize the signal to noise ratio as well. Placing the electrodes at distant pick-up locations will cause the sensitivity to be homogeneously distributed throughout the brain region and this is due to the effect of skull resistivity. The proposed electrode locations are C3/A2 for channel 1 and O2/A1 for channel 2. Moreover, the near DC components require using DC suppressed high gain amplifiers and the high gain should be achieved in a single stage to avoid further contamination with noise.

2.3 Magneto-encephalography (MEG) vs. Electroencephalography

2.3.1 Magneto-encephalography (MEG)

Magneto-encephalography is the measurement of the magnetic fields produced by electrical activity in the brain. It measures the magnetic fields generated by the intercellular currents of neurons in the brain. MEG is as useful as EEG in monitoring and diagnosing brain activities based on the fact that both techniques record the electrical activity of the brain in a similar way (Jaakko Malmivuo).

The magnetic field generated by a single neuron is extremely low in amplitude; and when several thousands of closely packed cells are synchronously active, the resultant extracranial magnetic field is in the order of pico Tesla. Detecting MEG is based on same principal of recording the induced magnetic fields based on the right hand rule of physics but in this case it is applied to the longitudinal neuronal current flow.

The magneto-encephalogram is detected using SQUID (super conducting quantum interface device) magnetometers which is based on Josephson junction and characterized by the extremely high sensitivity with a threshold in the order of 10fTesla.

2.3.2 Discussion

Although the skull is more transparent to the magnetic fields emitted by the brain, other drawbacks of MEG preclude its application in portable devices. SQUIDS are superconductors and are operated at cryogenic temperatures. Moreover, the MEG has extremely low amplitude which is 6 orders of magnitude weaker than the earth's steady magnetic field. Thus MEG is recorded in magnetically and radiofrequency shielded rooms. Accordingly, MEG recording is limited to clinical activities and EEG recording is proposed for portable applications.

2.4 Conclusion

In this chapter, the theory of electrophysiological measurements was introduced and the electroencephalogram was chosen as the signal of interest. Due to the complexity of brain structure and its electrophysiological behavior, the source function $\overline{J^i}$ can not be evaluated qualitatively from equation 2.10 (section 2.1.4). Thus a source model for the EEG spectrum can not be accurately formulated.

Recording EEG spectrum is susceptible to two sources of noise; artifacts and electromagnetic interference. Minimizing the effect of electrode displacement artifacts is required for portable recording. The proposed subdermal spiked array electrode enhances the mechanical attachment and adhesion of the electrode to the skin and moreover, this can be improved by optimizing the geometrical architecture of the electrode which will be discussed later in section 4.5. As for the wet gel electrodes and dry surface electrodes, their design is suitable for clinical recording where the patient is laying still (chapter 3). Differential recording utilizing high CMRR bio-amplifier circuits based on instrumentation amplifiers will be used to decrease the effect of electromagnetic interference. Moreover, due to the low voltage amplitude of the EEG signal, the electrode impedance has to be minimal which will be discussed in section 4.2.

Finally, sleep clinic experiments shown that monitoring EEG spectrum for predicting narcolepsy can be done through differential recording of two channels; C3/A2 for channel 1 and O2/A1 for channel 2. This requires four recording spots and suits the design specifications which requires minimizing the number of electrodes used.

Chapter 3

Wet and dry electrodes

3.1 Introduction

Electrodes are the sensors which detect the vital signs and electrophysiological signals emitted by the body organs. The sources of EEG and biopotentials are ionic currents which are different from the electric currents and can not be fed directly into electronic circuits, consequently; the electrode used in EEG detection is a transducer which converts bioelectric potential into electrode potential proportional to the exchange of ions between the electrode surface and the electrolytes of the body.

3.2 Types of electrodes

According to structure and application, conventional electrodes are classified as:
Microelectrodes: measure bioelectric potentials near or within a single cell.
Wet electrodes: measure ECG, EEG, EMG potentials from the surface of the skin.
Needle electrodes: penetrate the skin to record EEG potentials from a local region of the brain or EMG potentials from a specific group of muscles.

The state of the art can be categorized into:

- Dry-contact electrodes [23] [24].
- Non-contact ultra-high-impedance electric field probes [15] [25] [26].
- Dry-contact electro-optic sensors [27] [28].

Surface wet electrodes

Silver/Silver-Chloride surface wet electrodes are the most popular for EEG and ECG monitoring. This type of electrodes requires applying electrolyte rich with chlorine ions for proper operation. Silver/Silver-Chloride electrodes are characterized by their stability and extremely low noise.

This technology has its intrinsic drawbacks which preclude its compatibility for portable and long term application. When a metal electrode is applied on an unprepared surface of the skin, very high electrode-skin-electrode impedances (ESEI) result since no direct electrochemical electrode-electrolyte interface with the body fluids can be established. Therefore, standard biopotential electrodes (not having micro-spikes) require skin preparation prior to the application of the electrode which involves stratum corneum abrasion and use of electrolytic gel. Stratum corneum abrasion is a painful process to reduce the thickness of the SC. The electrolyte gel diffuses into the skin to create a continuum of conductive medium to overcome the low conductance of the stratum corneum epidermal layer. Moreover, it decreases the electrode displacement artifacts by offering good adhesion between the electrode and the skin. Wet electrodes require long stabilization time; after applying the conductive gel, it is left to diffuse into the scalp for 15 minutes before EEG measurements are started. It is obvious that the process is time consuming and non-comfortable for the patient. Wet electrodes are not suitable for long term recording because the gel dries away in 2 hours decreasing the electrical conductivity and the mechanical stability as well. Moreover, the wet electrodes can not be used in a portable device because cosmetically it is not appropriate. An electrochemical aspect which influences the electrode impedance is the interfaces introduced by the wet electrode system. These are the electrode-gel interface and the gel-skin interface. Having two interfaces increases the electrode-skin impedance, thus decreasing the recorded signal amplitude which results in a low signal-to-noise ratio.

Figure 3.1 shows EEG metal cap wet electrodes which are made of pure silver, tin or tin coated with gold or silver. These are non-disposable electrodes about 9mm in diameter.

Figure 3.1 – EEG metal cap wet electrodes

Wet electrode theory

After an electrode is immersed the electrolyte, it will begin to discharge some metallic ions into the solution, while some of the ions in the solution start combining with the metallic electrodes. This is, incidentally, the chemical phenomenon on which the electroplating and anodizing processes are based. After a short while, a charge gradient builds up creating a potential difference, or electrode potential which is a result of the difference in diffusion rates of ions into and out of the metal. Ions migrate toward one side of the region or another, forming two parallel layers of ions of opposite charge. This electrode double layer and its ionic differences are the source of the electrode half-cell potential which with the formation of the charge layers produces equilibrium.

The double layer of charge at the interface acts as a capacitor. Since measurement of bioelectric potentials requires two electrodes, the voltage measured is really the difference between the instantaneous potentials of the two electrodes. If the two electrodes are different, however, they may produce a significant dc voltage that can cause current to flow through both electrodes as well as through the input circuit of the amplifier to which they are connected. The DC voltage due to the difference in electrode potentials is the electrode offset voltage and the resulting current is often mistaken for a true physiological event. In addition to the electrode offset voltage, chemical activity taking place within an electrode can cause voltage fluctuations to appear without any physiological input. Such variations are noise that can be reduced by proper choice of materials or electrode treatment, such as electrolytic coatings to improve stability.

Dry-contact electrodes

These are mainly used for EMG and proved to have better performance in comparison with ordinary gel electrodes [15] [28] but not suitable for EEG monitoring and portable applications due to the electrode size and electrode displacement artifacts.

3.3 Theory of operation

The dry electrode is a micro-fabricated array of high aspect ratio micro needles to penetrate through the epidermis layer of the scalp. The first layer is the stratum corneum layer which is approximately 10 to 30µm of dead cells, followed by the stratum germinativum which is made of viable cells but void of blood capillaries or nerve cells and is about 50 to 100µm (refer to section 4.1). Thus, spikes penetrating the skin more than 30µm but less than 100µm produce a pain-free electrode-electrolyte interface at the SG and transform the ionic current induced by active cells into an electronic current [15].

Dry electrodes are characterized by better electrical performance; where signal pickup is improved as the skin-electrode impedance drops remarkably without the need for skin preparation. The electrode-skin-electrode impedance (ESEI) of spiked electrodes is stable over an extended period of time [24]. Also, penetrating the skin will minimize the effects of skin variations and body motion [15]. Mechanically, according to needles architecture, they can adhere better to the scalp, which will diminish the electrode motion artifacts and increase the signal monitoring period as well. Besides, gel electrodes introduce electrode-electrolyte interface and electrolyte-skin interface while dry electrodes introduce only electrode-skin interface thus the noise and artifacts sources are minimized. The small size and ease of use with no required skin preparation promote this type of electrodes to be used in portable and long term EEG monitoring. Finally, being CMOS compatible, the micro-electrodes can be integrated with CMOS circuits in a monolithic structure, thus the electrode can be integrated with a pre-amplifier.

Advantages of dry electrodes can be summarized as [23]:

- An array of micro pins stick to the scalp.
- Do not require conducting gel.
- Fast setup and cleaning time.
- Improve mechanical contact.

- Improve conductivity and signal pick up (since they penetrate into the skin).
- Compatibility with CMOS technology.

Referring to table 3.1, the comparison between the wet and dry electrodes surmise that dry electrodes are more convenient to use and will enhance the EEG monitoring system performance.

Table 3.1 – Wet and dry electrode comparison

Wet electrodes	**Dry electrodes**
-Large size to satisfy electrical and mechanical constraints. -Require application of gel. -Require skin preparation (abrasion). -Long setup and cleaning time. -Introduce electrode motion artifacts.	-Do not require conducting gel. -Fast setup and cleaning time. -Improve mechanical contact. -Improve conductivity and signal pick up. -Diminish electrode motion artifacts. -Cosmetically concealable. -CMOS compatible.

3.4 Conclusion

Wet and dry surface electrode technologies are limited for short term clinical recording. Moreover, wet electrode application requires skin preparation which has to be done by a trained technician. On the other hand, the dry electrode design proposed in this thesis can potentially satisfy the design specifications in terms:

- Suitability for long term recording which raises two main issues involving electrode stability and tissue reaction due to prolonged interaction periods.
- Size and concealability.
- Less sensitive to electrode displacement artifacts.
- Ease of application without the need for skin preparation or conductive gel application.

Optimizing the performance of the electrodes requires exploring the different parameters involved in the electrode design. This includes the geometrical layout, electrode material and the mechanical strength which will be illustrated in the following chapters.

Chapter 4

Design optimization methodology

Part 1 – Physiological concepts

4.1 Skin anatomy

4.1.1 Introduction to skin functions

Skin is the largest organ in the human body and it is responsible for diverse vital roles involving human body protection and regulation. The skin functions in thermoregulation, protection, metabolic functions and sensation. It provides a protective barrier to interface with the hostile environment; and guards internal tissues from exposure to trauma, ultraviolet radiation and bacteria. Skin is involved in maintaining the proper temperature for the body and protects it from temperature extremes. It also provides sensory perception from the environment as well as immunologic surveillance.

4.1.2 Skin anatomy

The integument (skin) is divided into two mutually dependent layers as shown in figure 4.1; the epidermis and the dermis, each providing a distinct role in the overall function of the skin [29].

Epidermis

The epidermis is the most superficial layer of the skin and creates the first barrier of protection from the invasion of foreign substances into the body. The thickness of the epidermis varies in different types of skin. It is the thinnest on the eyelids at 50 μm, grows to 100 μm on the forehead [24] and reaches it's thickest on the palms and soles at 1500 μm.

The epidermis contains no blood vessels and is entirely dependent on the underlying dermis for nutrient delivery and waste disposal via diffusion through the dermo-epidermal junction. The epidermis is a stratified squamous epithelium consisting primarily of keratinocytes in progressive stages of differentiation from deeper to more superficial layers.

The epidermis is divided into five layers (strata) from bottom to top:

- The stratum germinatum (SG) (stratum basale)

- The stratum spinosum (SS)
- The stratum granulosum (SGR)
- The stratum lucidum
- The stratum corneum (SC) in which a keratinocyte gradually migrates to the surface and is sloughed off in a process called desquamation.

The basal cell layer is called the stratum germinatum because it is constantly germinating new cells which are necessary for the regeneration of the layers of the epidermis. The stratum germinatum (SG) is the bottom layer of the epidermis. In this layer the cells divide and push the formed cells into the upper layers. As the cells move, they flatten and eventually die. The stratum corneum which is the top layer of the epidermis is made of dead, flat cells that shed about every 2 weeks. These germinal cells are separated from the dermis by a thin layer of basement membrane [29] [30].

Above the basal cell layer is the squamous cell layer, also called the stratum spinosum or “spiny layer” because the cells are held together with spiny projections. They have begun to produce keratin which is a tough protective protein that makes up a large part of the structure of the skin, hair and nails. It is the thickest layer of the epidermis. The squamous cell layer also contains cells called Langerhans cells, if the skin becomes damaged, these cells latch onto invading antigens, substances that are foreign to the body, and alert the im-mune system to their presence..

The keratinocytes from the squamous layer are then pushed up through two thin epidermal layers called the stratum granulosum and the stratum lucidum. As the cells migrate, they enlarge, flatten, and bond together, then eventually become dehydrated and die. The process fuses the cells into layers of tough durable material which continue to rise toward the skin’s surface forming the stratum corneum which is the outermost, visible layer of the epidermis. The stratum corneum is made up of 10 to 30 thin layers of these dead cells [30].

Stratum Corneum – elaborated

The stratum corneum is made up of 15 to 20 layers of dead cells. These cells are the largest and most abundant of the epidermis. This layer ranges in thickness from 15-100 or more cells depending on anatomic location and is the primary protective barrier from the external environment. SC has a thickness that ranges between 10 µm to 15 µm [28] [31] [32] and reaches 1000 µm on the sole of the foot. It is not soluble in water, but it absorbs large amounts of water, thus in the case of using conductive gels, the moisture will increase the thickness of the SC layer and consequently increasing its impedance [33].

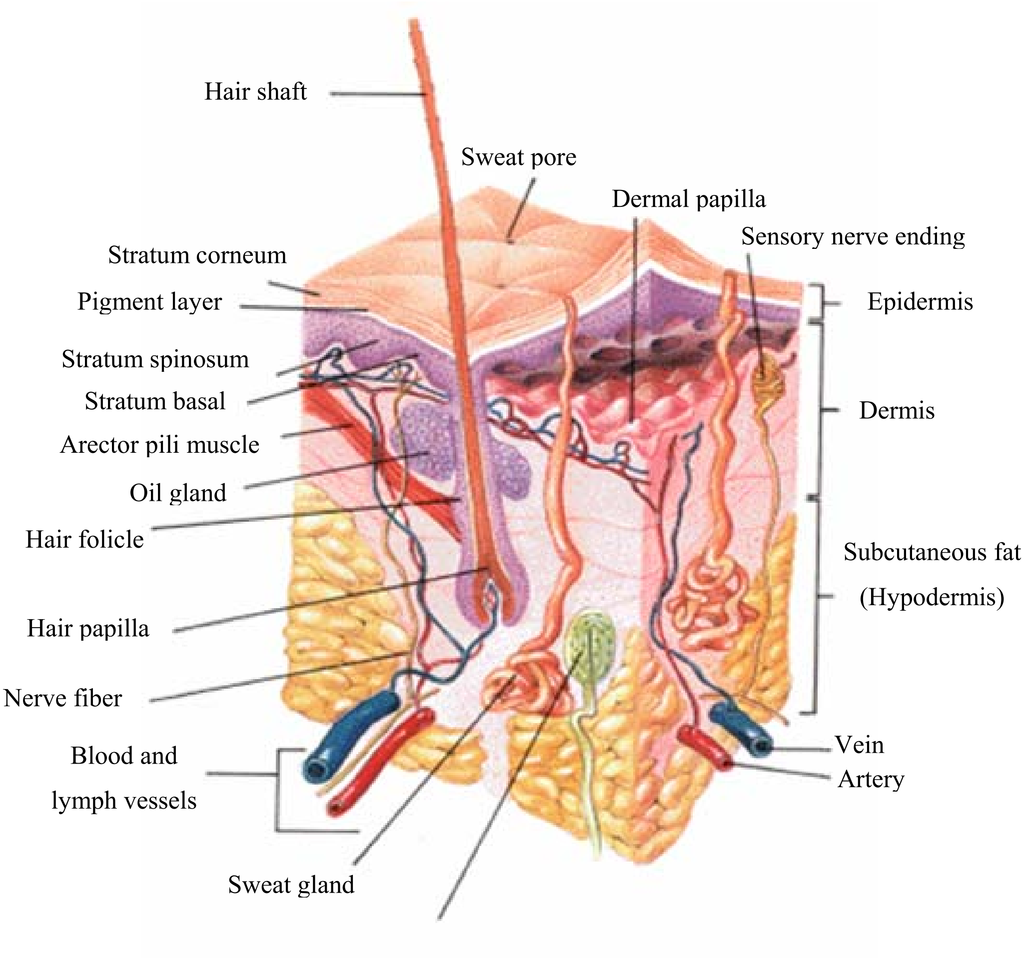

Figure 4.1 – Skin anatomy [29]

SC can be considered as solid state electrolyte with few free ions that contribute to the DC conduction. It has broad α-dispersion while the viable cells have separate α and β dispersion. At low frequencies (<10 KHz), the skin impedance is dominated by the SC layer. As frequency increases, the impedance is dominated by the viable cells [33].

Dermis

The dermis is a more complex structure and is composed of 2 layers, the more superficial papillary dermis and the deeper reticular dermis. It varies in thickness depending on the location of the skin from 300 µm on the eyelids up to 3000 µm on the back.

The dermis is responsible for thermoregulation and supporting the vascular network to supply the avascular epidermis with nutrients. It dermis contains mostly fibroblasts which are responsible for secreting collagen, elastin and ground substance that give the support and elasticity of the skin. It also has immune cells to protect against foreign bodies passing through the epidermis, thus the dermis is the first defense against disease. Much of the body’s water supply is stored in the dermis. When the amount of stored water is increased, the skin becomes tight and stretched as it expands to accommodate the surplus. Finally, the scavenger cells in the dermis are a part of the immune system which engulf and destroy foreign organisms which make it past the epidermis [30] [34].

It is composed of three types of tissue that are present throughout; these are collagen, elastic tissue and reticular fibers. The dermis is typically subdivided into two zones, a papillary dermis and a reticular layer. The papillary dermis (PD) contains vascular networks that have two important functions; the first being to support the avascular epidermis with vital nutrients and secondly to provide a network for thermoregulation. The vasculature is organized so that by increasing or decreasing blood flow, heat can either be conserved or dissipated. The vasculature interweaves in areas called dermal papillae (DP). The papillary dermis also contains the free sensory nerve endings and structures called Meissner’s corpuscles in highly sensitive areas.

The papillary dermis is thinner, consisting of loose connective tissue containing capillaries, elastic fibers, reticular fibers, and some collagen. While the reticular dermis consists of a thicker layer of dense connective tissue containing larger blood vessels, closely interlaced elastic fibers, and coarse bundles of collagen fibers arranged in layers parallel to the surface. The reticular layer of the dermis is important in giving the skin its overall strength and elasticity, as well as housing other important epithelial derived structures such as glands and hair follicles [34] [35].

4.1.3 Discussion

The anatomical structure of the scalp outlined a set of design rules and constraints for the needles and electrodes architectures.

The theory of the electrode application is to penetrate through the insulating stratum corneum (SC) layer to improve the electrical properties of the electrode-skin interface as well as benefit from the dry electrodes mechanical and clinical advantages.

The SC and SG layers thickness imply that the needles should be more than 30µm in length to cross the SC layer but should not exceed 100µm to avoid penetrating through the dermis. Avoiding the contact with the dermis layer keeps the needles away from the nerve cells, blood capillaries, sweat glands and lymph nodes. This will prevent pain and bleeding.

Lastly, due to the interaction of proteins with the skin penetrating needles, bio-fouling should be considered to satisfy the long term recording working condition. Proteins tend to adhere to the needles being a foreign body which will encourage further skin adhesion forming an organic layer on the needles that increases the electrical resistivity affecting the electrode functionality.

4.2 Skin electric model

4.2.1 Introduction

This section deals with the characterization of the skin electrical properties and outlines an equivalent electrical model. The electrical properties of the biological tissue are distinguished by showing a wide range of impedance values and different electrical properties [36] and the variability of skin properties affect the impedance measurements of the system. These variations result due to physiological, psychological or pathological reasons, for example the difference in skin structure or a skin disease. Moreover, the skin impedance of a certain spot can vary due to homeostatic effects, and the skin electrical properties are function of frequency as well [37] [38] [39] [40].

4.2.2 Impedance measurement

The traditional method to determine the impedance of a system involves sweeping the measuring signal frequency along the system bandwidth. But the skin exhibits non-stationary electrical properties due to electrical current flow and the measured response will be distorted. Another measuring technique implies applying a waveform comprised of a range of frequencies digitally constructed to overcome the need of stepped sweeping. A large number of frequencies have to be applied simultaneously to overcome the rapid changes in the skin and skin-electrode impedance [41].

4.2.3 Skin impedance

A simple three component model (TCM) equivalent circuit and its Argand diagram are shown in figures 4.2 and 4.3 [41].

The outer layer of Stratum Corneum exhibits distinct electrical properties from the viable tissue which gives the epidermis the greatest influence on the electrode-skin interface, while the deeper layers of the epidermis and dermis do not exhibit unique electrical characteristics. The epidermis can be considered as a leaky capacitor while the dermis is considered to be resistive.

At high frequencies between 100KHz and 1MHz, the skin response doesn’t show remarkable impedance variations. The series resistance in the three element skin model is estimated to be fixed at approximately 120Ω [42]. Moving to a lower frequency band between 1kHz and 100kHz; wider dispersion is characterized by a 10-40nF capacitor which corresponds to the capacitance of the SC [43].

Finally, near DC and up to 100Hz; the low-frequency impedance of the skin reaches high values and the low-frequency impedance is modeled by a shunt RC circuit with a resistance value of 5KΩ. This resistor corresponds to the resistance of the SC and a conventional technique to decrease the skin impedance is through abrading the SC layer which helps in achieving a scalp-electrode impedance less than 5KΩ [42] [43] [44]. A fact worth mentioning is that the rate of sweating influences the low frequency impedance of this layer and causes a 50% drop in its value. Moreover, sweat ducts introduce electrical shunt paths for DC current and are hence considered conductive (Martinsen et al. 1998). The sweat duct polarization is insignificant and the polarization admittance of the skin is exclusively linked to the stratum corneum which implies that low frequency AC impedance measurements only reflect the stratum corneum properties [45].

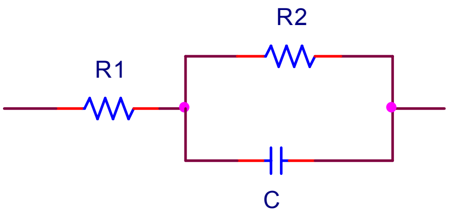

Figure 4.2 – Three components skin circuit model

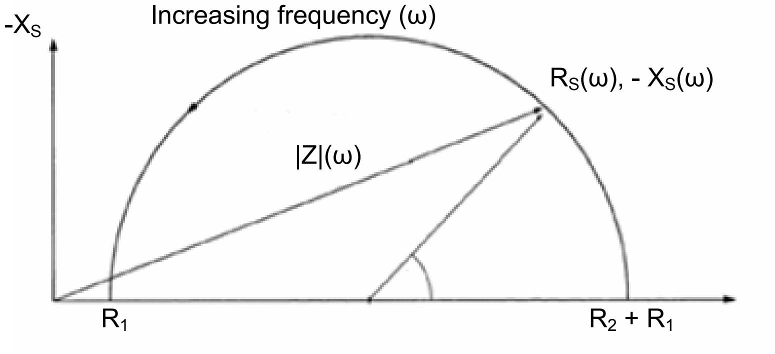

Figure 4.3 – TCM Argand diagram

Figure 4.4 plots different measurements for the skin impedance; two plots are instantaneous measurements at t = 0 and t = 90 seconds, while the intermediate plot lists the measurements taken by frequency sweeping.

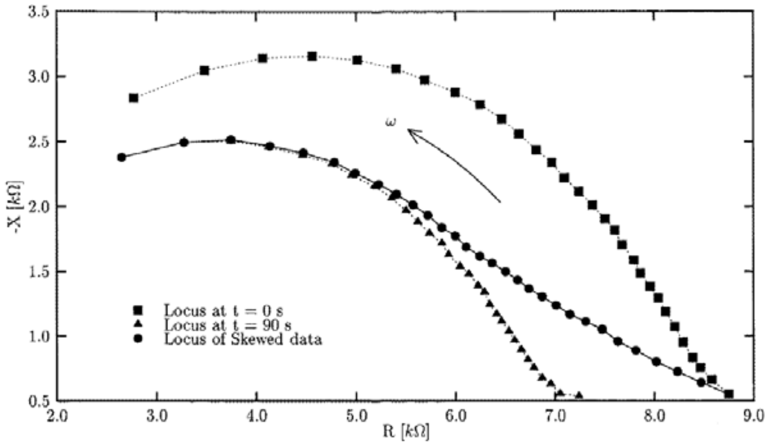

Figure 4.4 – Skin impedance plots of simultaneous measurements vs. frequency sweeping [41]

4.2.4 Simple skin circuit model

A more detailed skin model of a circular area of 1cm^2 is illustrated in figure 4.5. The epidermis is represented by three series networks each is formed of RC shunt circuit. The dashed lines represent different depths in case skin abrasion is applied to remove the stratum corneum, where the skin impedance will drop. The dermis is simply modeled as a resistive element [45].

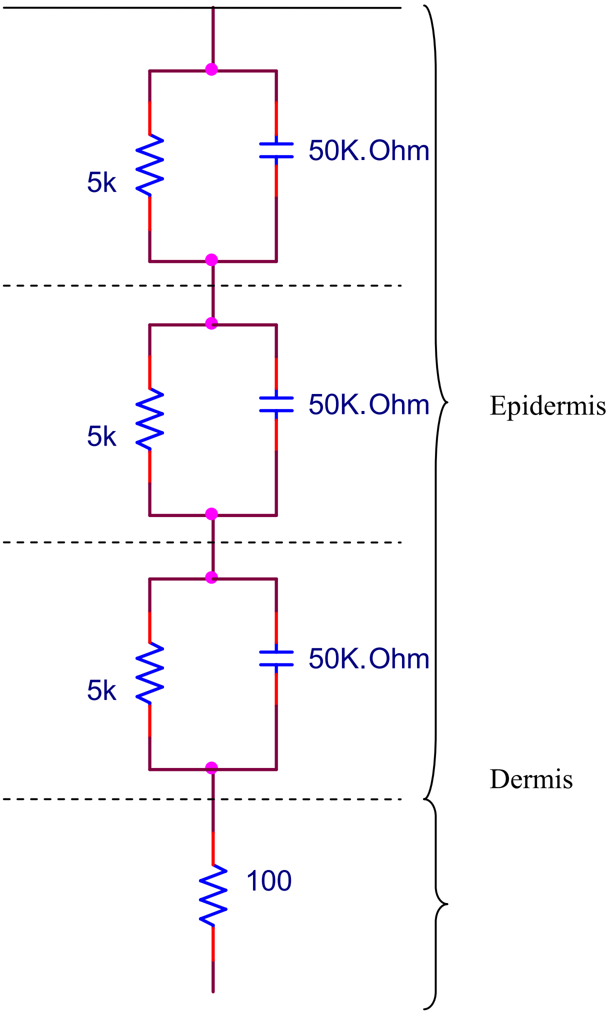

Figure 4.5 – Skin circuit model

4.2.5 Tissue resistivity

The human body may be considered as a resistive, piecewise homogeneous and linear volume conductor. Most of the tissue is isotropic; however, brain tissue is anisotropic. A list of different tissue resistivities is available in table 4.1.

Table 4.1 – Resistivity values for various tissues

Tissue	Resistivity (ρ) [Ωm]	Remarks
Brain	2.2 [46]	Gray matter
	6.8 [47]	White matter
	5.8 [47]	Average
Cerebrospinal fluid	0.7 [48]	
Blood	1.6 [49]	Hct = 45
Plasma	0.7 [47]	
Heart muscle	2.5 [50]	Longitudinal
	5.6 [50]	Transverse
Skeletal muscle	1.9 [51]	Longitudinal
	13.2 [51]	Transverse
Liver	7 [50]	
Bone	25 [52]	
	177 [46]	Longitudinal
	15 [53]	Circumferential
	158 [53]	Radial (at 100 kHz)
	215 [53]	

4.2.6 Modeling the Head

The brain is composed of excitable neural tissue and the brain tissue acts as bioelectric source and a volume conductor. It can be modeled as series of concentric spheres representing the brain, skull, and scalp as shown in figure 4.6 [37]. This symmetric model does not consider the anisotropy and inhomogeneity of the brain tissue and the cortical bone [38].

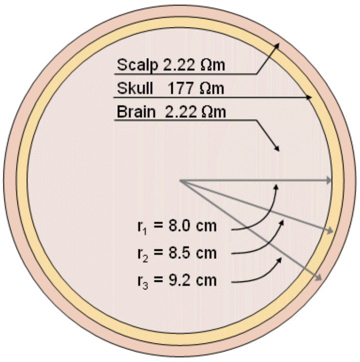

Figure 4.6 – Modeling the head [7]

4.2.7 Discussion

The skin impedance contributes to the source impedance of the signal input to the bio-amplifier and is dominated at low frequencies by the stratum corneum layer. Having low source impedance is favorable when feeding a voltage amplifier. Also, lowering the skin impedance helps in improving the signal amplitude provided that the targeted EEG signal suffers extremely low amplitudes which makes it susceptible for distortion resulting from noise and artifacts.

One way to overcome the stratum corneum contribution to the impedance is to get rid of it by abrasion which is an uncomfortable procedure. Applying conductive gel is another solution suitable for short term recording as the gel eventually dries. The proposed design short-circuits the SC impedance through a painless procedure wile preserving the electrode-skin impedance stability allowing long term recording. Moreover, decreasing the electrode impedance to its minimum value is achieved by choosing the optimal structural geometry for the electrode as will be discussed in section 4.5 and the proper choice of the electrode material that also satisfies the mechanical and bio-compatible requirements.

Part 2 – Material requirements

4.3 Materials and biocompatibility

4.3.1 Introduction

A biocompatible material has physical and chemical properties such that when interacts with living tissues if used in medical devices or implants; does not produce a toxic, injurious, or immunological response.

Biocompatibility of synthetic materials in the body is complicated and involves processes traditionally related to medical science, surface science, materials science, and molecular biotechnology. Inserting an artificial material in living tissue will initiate a race for the surface; a bio-layer consisting of water, proteins and other bio-molecules from the physiological liquid is formed on the implant surface. Subsequently, cells from the surrounding tissue migrate to the area around the implant due to stimulation by cytokines and growth factors in the bio-layer. The interaction between an implant surface and the cells is thus mediated through this bio-layer [54].

Devices intended for long-term in vivo applications have to satisfy rigorous biocompatibility and bio-stability requirements [55]. As long as the electrode is intended for long term use that can extend up to 12 hours, it can be regarded as a medical implant to ensure medical safety issues.

4.3.2 Bio-compatibility evaluation

Biological performance of a material is evaluated by two perspectives; material response to living systems and host response. The host response is a local or systemic reaction other than the intended therapeutic response of living systems to the material [54], it evokes changes in the homeostatic mechanisms which stabilize the internal body equilibrium and can be assessed by evaluating the biological responses [56]. A biocompatible material results in minimal biological response.

In brief, material biocompatibility can be described in terms of the acute and chronic inflammatory responses and of the fibrous capsule formation after an implantation or long term application of a synthetic material [57] [58].

Choosing materials for biomedical applications is subject to the following criteria [59]:

- Tissue reaction
- Corrosion
- Design and functionality
- Mechanical properties
- Surgical implications

4.3.3 Metal-Fluid interaction

The dissolution of a metal implant in the body fluids activates the immune system. But the low molecular weight and simplicity of metallic ions stall the activation of humoral or cell-mediated responses.

When the metallic electrode comes in contact with the body tissue, a metal-fluid interface is formed and an organo-metallic compound will be produced by the chemical reactions. Some of these organo-metallic complexes are be carcinogenic. Moreover, the occurrence and removal of this compound directly influences the rate of corrosion [60].

Details about the chemistry of corrosion its different forms is available in appendix C.

4.3.4 Choosing the appropriate metal for the electrode

From a surgical prospective, the use of metals in medical applications implied complications with post-surgical infections. Controlling the occurrence of infection helped in clarifying the relationships between material properties and the success of implants [61].

Tissue compatibility, corrosion resistance, and mechanical strength are critical for the application. Noble metals, gold and silver, met the first two criteria. Metals such as brass, copper, and steel had adequate strength for many applications but exhibited poor corrosion behavior and tissue compatibility. Finally, silver is considered for the application.

Ag-AgCl Electrodes

The most popular surface electrodes used in electrophysiological recordings are the non-polarizable Ag-AgCl electrodes. AgCl coated silver electrodes were introduced in [62] for subdermal recording. Ag-AgCl electrodes posses stable responses keeping low frequency in the form of voltage fluctuations produced by the chemical activity within an electrode at their minimum values [63].

On the other hand, Ag-AgCl electrodes have inherent drawbacks which render them not preferable for subdermal applications:

A chloride based conductive gel is required to create a working environment for the Ag-AgCl electrode. Although the gel can be applied by diffusion as the case with wet electrodes, but this process cannot be controlled. Moreover, it is not suitable for long term recording because the gel will diffuse away. Besides to the inapplicability of the chloride gel, the ionic solutions of the body will interfere with the chemical equilibrium of the Ag-AgCl ambient environment and will disturb the stability of the electrode.

Secondly, Ag-AgCl electrodes tend to react with high protein compounds like blood [64] and they have to be avoided in subdermal application.

As for long term application, they have poor long-term stability lose when used with biological tissue [65].

Silver

Silver is recognized a biocompatible metal suitable for the electrode provided that it exhibits high electrical conductivity. It possesses a good combination of mechanical and corrosion resistance properties as well excellent tissue compatibility. Physiologically, silver alloys are well tolerated by animal subjects [66] [67] [68] [69] and it has low immune response in the body which makes it favorable for biocompatible applications.

Silver thermodynamic stability can be inferred from its Pourbaix diagram in figures 4.7 and 4.8 as a function of the potential and ambient pH. Pourbaix diagram maps the possible stable phases of an aqueous electrochemical system which is based on Nernst equation (thermodynamic theory) where the electrode potential is evaluated relative to the standard electrode potential of an electrode couple. The extracellular fluid dominates the environment of the electrode with a pH ranging between 7.35 and 7.45 and a potential of 200mV, and being a noble element; silver electrodes show immunity against corrosion.

Finally, silver is compatible with the micro-fabrication techniques used in producing the electrodes.

Silicon

Doped silicon can be used as the electrode material but it experience severe biofouling over prolonged contact time with body fluids [70] [71] [72]. But intrinsic silicon can be used as a core and coated with a biocompatible metallic layer.

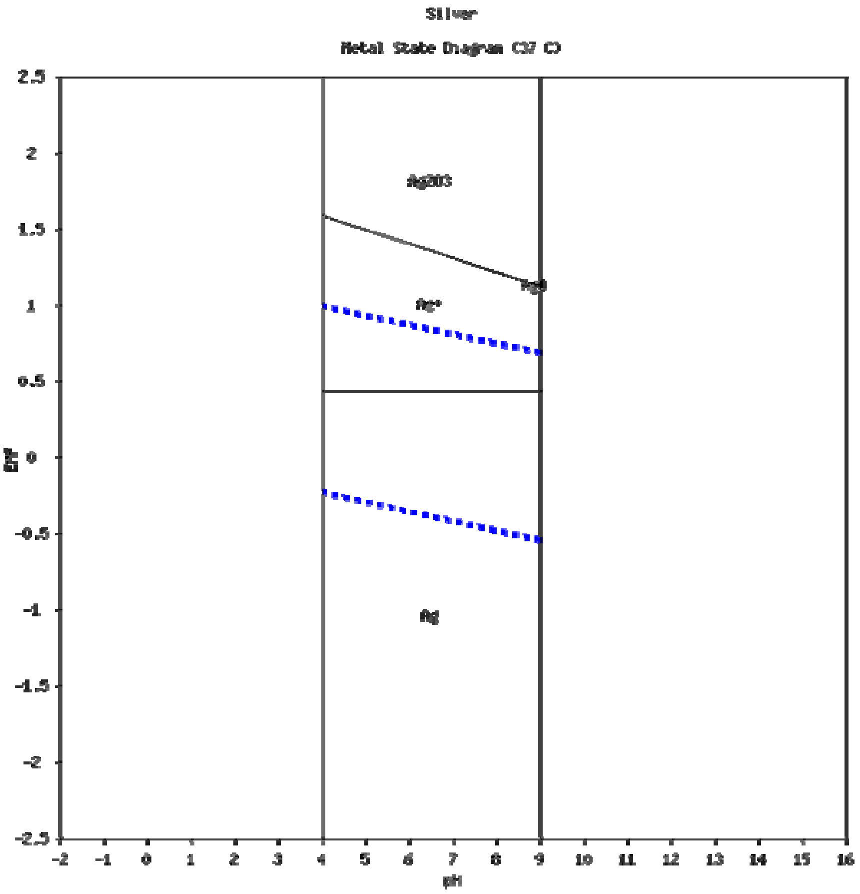

Figure 4.7 – Ag Pourbaix diagram at 37^{o}C [73]

A comparison between the mechanical and electrical properties of silver and gold in table 4.19 shows that silver has lower electrical resistivity and a higher ultimate stress.

4.3.5 Discussion

Although silver and gold are inert and thus suitable for medical applications and immune to corrosion, but silver demonstrates better electrical and mechanical properties compared to gold. Its high electrical conductivity improves the electrode performance and finally, it is compatible with the micro-fabrication technology proposed in chapter 6.

4.4 Bio-fouling and antifouling coating

4.4.1 Introduction

Bio-fouling is the tendency of the proteins in living tissue to adsorb to artificial and foreign objects inserted in the body. The adsorbed protein layer can initiate biological reactions including cell attachment and activation; this will disrupt the proper operation of the electrodes. Biological activity of adsorbed proteins can also cause platelet adhesion and blood clotting on foreign surfaces [74]. The electrode's destination is a biological environment, and being a foreign structure to the human body; this will provoke an interaction between the needles and body proteins and cells [7575] which will affect the electrode resistance, and in consequence; the signal levels [76].

Although biological micro-electromechanical systems (Bio-MEMS) and silicon-based microelectrodes show good performance in vitro, they experienced bio-fouling when used in vivo and the effect is exaggerated in the case of long term application [77] [78] [79]. Since the electrodes will be used for long term EEG monitoring, thus; they have to be designed in a way to overcome potential bio-fouling problems.

4.4.2 Bio-fouling treatment

Cell adhesion can take place through two mechanisms:

1. Nonspecific attachment (the hydrophobic effect).
2. Specific protein-cell interactions.

Surface treatment of exposed surfaces enhances the electrodes biocompatibility and prevents bio-fouling by inhibiting surface reactions and avoiding protein adsorption [80] [81]. Surface coating the electrodes with biologically anti-fouling polymers counteracts the nonspecific affinity of proteins and cells to attach to surfaces [82] [83] [84] [85].

4.4.3 Materials

There are different polymers with hydrophilic properties. The list is long, for example: poly-hydroxy-ethyl-methacrylate, poly-acrylamide, poly-N-N-dimethyl-acrylamide, dextran, Poly-N-isopropylacrylamide (pNIPAM), poly-ethylene glycol (PEG) and Plasma polymerized tetra-glyme (pp4G).

Not all the polymers are compatible with the human body due to toxicity limitations; moreover, some biocompatible materials are not suitable for the electrode application. For example, the function of pNIPAM is temperature dependant, where its hydrophilic properties are revealed at temperatures below 31ºC. While as the temperature rises above 31ºC it turns to be hydrophobic.

PEG is a non-toxic hydrophilic hydrogel and is suitable for biomedical applications [85] [8386]. It is approved by the FDA for use in biotechnology. The stability of Poly-ethylene-glycol (PEG) thin films decreases in vivo because it is affected by aqueous solutions [87]. Commercially, PEG is used in emulsifiers and cleansers to dissolve oil and grease.

PP4G (CH_3-(O-CH_2-CH_2)$_4$-O-CH_3) can produce a PEG-like material with high protein resistivity, surface adhesion and biocompatibility [80] [88] [89] [90] [91]. PP4G has excellent adhesion to different silicon, oxide and metallic substrates [92] [93], durable and can be patterned with photolithography.

4.4.4 Technique

There are different techniques to coat a surface with PEG, for example, physical adsorption and covalent immobilization (chemical coupling) which creates stable coatings based on strong covalent bonds [87].

A surface coating technique proposed in [89] uses glow discharge plasma polymerization of tetra-glyme (CH_3-O-(CH_2-CH_2-O)$_4$-CH_3) to create a thin film of PEG-like material. This technique also allows the patterning of the protein resistive layer.

4.4.5 Electric properties

The effect of a PP4g coat on the AC resistivity coated electrode is acceptable. A thin PP4G raised the electric resistivity from 5e9 $\Omega\mu m^2$ to 7e9 $\Omega\mu m^2$ measured at 10 Hz. Thus a pp4G coated electrode will provide both bio-compatibility and good electric conductivity [80].

4.4.6 Bio-fouling on a larger scale

Bio-fouling can also be described as the undesirable accumulation of microorganisms, plants and animals on artificial surfaces. The sources for this undesired process include sticky bio-films of bacteria and seaweeds. It has adverse effects on marine and sub-aquatic activities, for example; bio-fouling on a ship reduces it hydrodynamics thus degrading the speed and maneuverability. Moreover, on static structures like piers and offshore oil and gas platforms, bio-fouling can enhance the corrosion of metal by seawater, reducing the metal's susceptibility to environmental fracture, and increasing the risk of mechanical failure.

4.4.7 Discussion

Due to the prolonged electrode application, biofouling has to be considered due to the tendency of proteins and cells to adhere to foreign bodies inserted in the human body. To meet the required design specifications and the required performance, coating the electrode with a thin film of PEG-like material can maintain the electrode performance during long term recordings.

Part 3 – Design optimization

4.5 Geometrical electrode parameters design optimization

4.5.1 Introduction

The objective of the optimization analysis is maximizing the contact surface area between the electrode and the surrounding extra-cellular tissue to decrease the electrode-skin impedance and consequently, maximize the electrical performance of the electrode. This aims to improving the physiological, electrical, mechanical and economical performance of the electrode.

As the geometric structure of the electrode affects its impedance, accordingly; tuning the needle geometry can improve the electric characteristics. This will improve the signal strength and reduce the effect of noise and artifacts, and consequently the performance and accuracy of the succeeding system stages will be enhanced, i.e.; digital signal processing and analysis.

Decreasing the electrode impedance can be achieved through:

- Using materials with high conductivity (metals or highly doped silicon). Choosing the material is subject to physiological constrains due to biocompatibility issues.
- Increasing the surface area of contact.

4.5.2 Problem formulation

The objective of the optimization problem is to maximize the contact surface area between the electrode and the viable skin layers which make up the electrolyte. This will be accomplished through the following steps:

- Maximizing the needles height.
- Maximizing the total perimeter of all needles in the array.
- Maximizing the needles packing.

The area of contact is evaluated as the lateral surface area of the electrode. Equation 4.1 expresses the total lateral surface area ($A_{Contact}$) as a function of the needle's geometry:

$$A_{Contact} \propto (n) \times (h) \times (P_{Needle}) \quad (4.1)$$

n: number of needles

h: individual needle height

P_{Needle} : perimeter of needle

This is an approximated relation that neglects the contribution of the needle's tip as well as the portion of the base substrate which is in contact with the scalp due to its high contact resistance relative to the subdermal area of the electrode.

The tunable parameters controlling the design are the needle perimeter and needles packing, on the other hand; the height and material can be treated as constants parameters governed by the physiological and biomaterial issues discussed in the previous sections.

Equation 4.1 can be written as:

$$A_{\text{Contact}} \propto (n) \text{ x } (P_{\text{Needle}}) \tag{4.2}$$

And the optimization objective evolves to pursue maximizing the total needles perimeter as expressed in equation 4.3

$$P_{\text{Total}} \propto (n) \text{ x } (P_{\text{Needle}}) \tag{4.3}$$

The optimization problem seeks the optimal combination of needles' geometry and packing on an electrode that will yield a maximal total perimeter and consequently a maximal lateral surface area according to the set of constraints which rule the system.

4.5.3 Previous research and problem definition

Boyce et al defined this problem as maximum and minimum area polygon (MAXP) given a set of vertices. Fekete and Pulleyblank (1993) discussed the problem of optimizing the area of a simple polygon defined by a given set of vertices P and described it as "Minimum Area Polygon" (MAP) problem.

Calculating the area of a polygon with rational vertices can be easily accomplished by adding the area of the triangles in a triangulation, which is not the case with determining the perimeter where it is more complicated [91].

It was also proven that the problem of finding a minimum weight polygon for a given vertex set is NP-complete which means that it is NP-hard to find a minimum area simple polygon with a given set of vertices. Nondeterministic Polynomial (NP)-completeness is the complexity class of decision problems for which answers can be checked for correctness by an algorithm whose run time is polynomial in the size of the input and no other NP problem is more than a polynomial factor harder. In more simple words an NP-complete problem can be verified quickly, and a quick algorithm to solve this problem can be used to solve all other NP problems quickly. When a decision version of a combinatorial optimization problem is proved to belong to the class of NP-complete problems, then the optimization version is NP-hard. The problem can be tackled using the Grid Avoiding Polygon (GAP) and Pick's theorem.

Pick's theorem (Pick et al, 1899)

The theorem formulates the area of simple lattice polygons which do not have of self-intersections. As shown in figure 4.8; polygons covered by the theorem have their vertices located at nodes of a square lattice equally spaced nodes with unit steps.

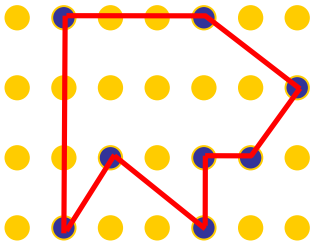

Figure 4.8 – Pick's theorem

If P is a simple polygon given by a set of vertices and a set of edges where all its vertices are only contained in two edges and nonadjacent edges do not intersect. Let I(P) be the number of grid points contained in the interior of P, and B(P) is the number of grid points on the boundary of P.

Then, the area of polygon P can be written as:

$$\text{Area} = \frac{1}{2}B(P) + I(P) - 1 \tag{4.4}$$

A grid point contained in the boundary contributes (1/2) to the area of the polygon, while grid point in the interior contributes 1. To minimize the area, grid points other than the given vertices are avoided, and this results in a polygon of area:

$$\text{Area} = \left\lceil \frac{n}{2} - 1 \right\rceil \tag{4.5}$$

4.5.4 Implemented optimization technique

The technique developed in the proposed design optimization is based on modeling the problem by a set of fundamental linear and trigonometric functions relating the parameters of the edges and vertices of the geometric shape to its dimensions, perimeter and area.

Global and local optimization

The optimization problem was broken down into a set of local optimization problems limiting the number of varying parameters in each problem. The outcome was a set of local optimal solutions competing to offer the ideal set of states for the variable parameters. This approach improved building and tuning the optimization model and provide better understating of the influence of each variable parameter and constraint on the performance of the system.

The maximal total lateral surface area

Maximizing the perimeter independently will lead to the expansion of the cross-sectional area of some geometric shapes. This uncontrolled increase in the needle's cross-section area is not desired because the available chip area will be consumed inefficiently, and will result in poor packing, i.e. fewer needles can be contained per chip.

Thus the perimeter optimization problem evolves to a "maximum perimeter minimum area" problem. This introduced a new variable to the problem which is the degree of the polygon describing the needle's cross-section that will provide the maximal perimeter while keeping the cross-sectional area as small as possible. Moreover, the geometric shape must optimize the packing to increase the density of needles per chip.

Design phases and choosing the optimal geometry

The first optimization phase involved circular cross-section needles forming an array of cylindrical prisms. The second phase was searching for the optimal solution within uniform convex polygon cross-sections (in a convex polygon, if any two vertices are connected by a line segment, it will not intersect any side). The third phase focused on triangular cross-sections, and this was followed by examining hollow structures to increase the area of contact. Finally, more complicated geometries are explored, this included formations of crosses and square needles.

4.5.5 Problem design procedure

The solution procedure begins with defining the objective function, and then the variable parameters influencing the design are identified, followed by creating the ruling equations and finally, outlining the constraints.

In parallel, the asymptotic boundaries of the optimal solution were evaluated using analytical methods to confirm the optimization model. The consistency of the analytical approach results proved the validity of the model, while inconsistency will trigger remodeling the system. Finally, the valid model is used in the different design phases. The block diagram in figure 4.9 highlights the main steps of the optimization procedure.

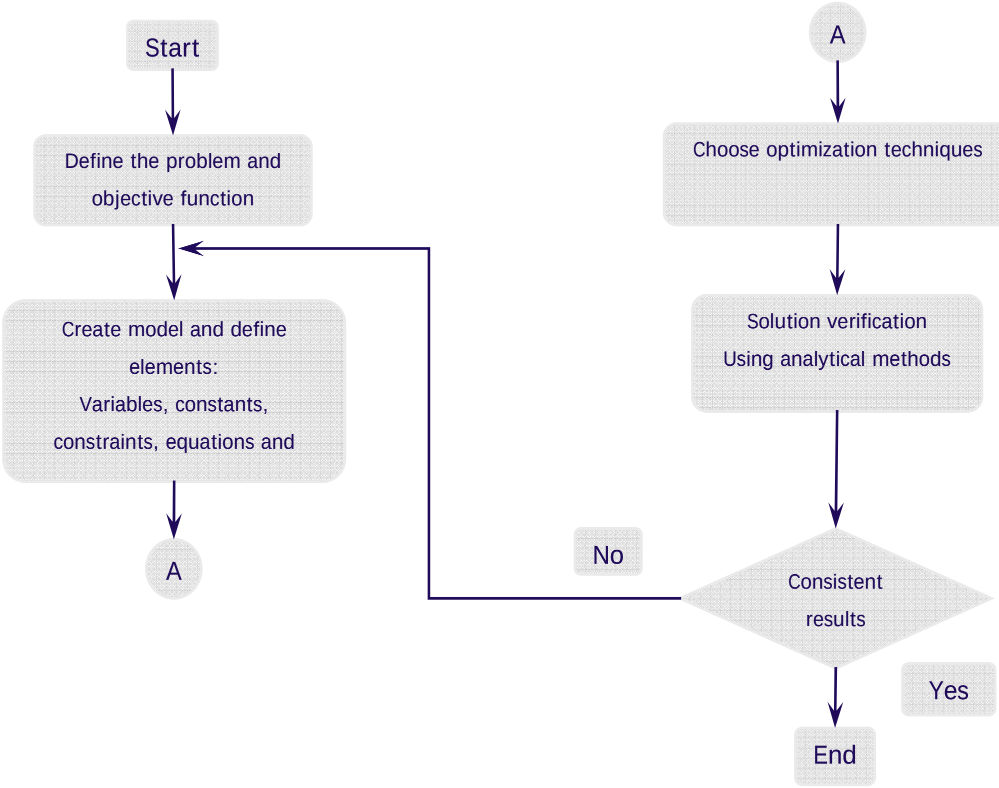

Figure 4.9 – Optimization process flowchart

4.5.6 Problem formulation

Figure 4.10 shows more details about the optimization technique:

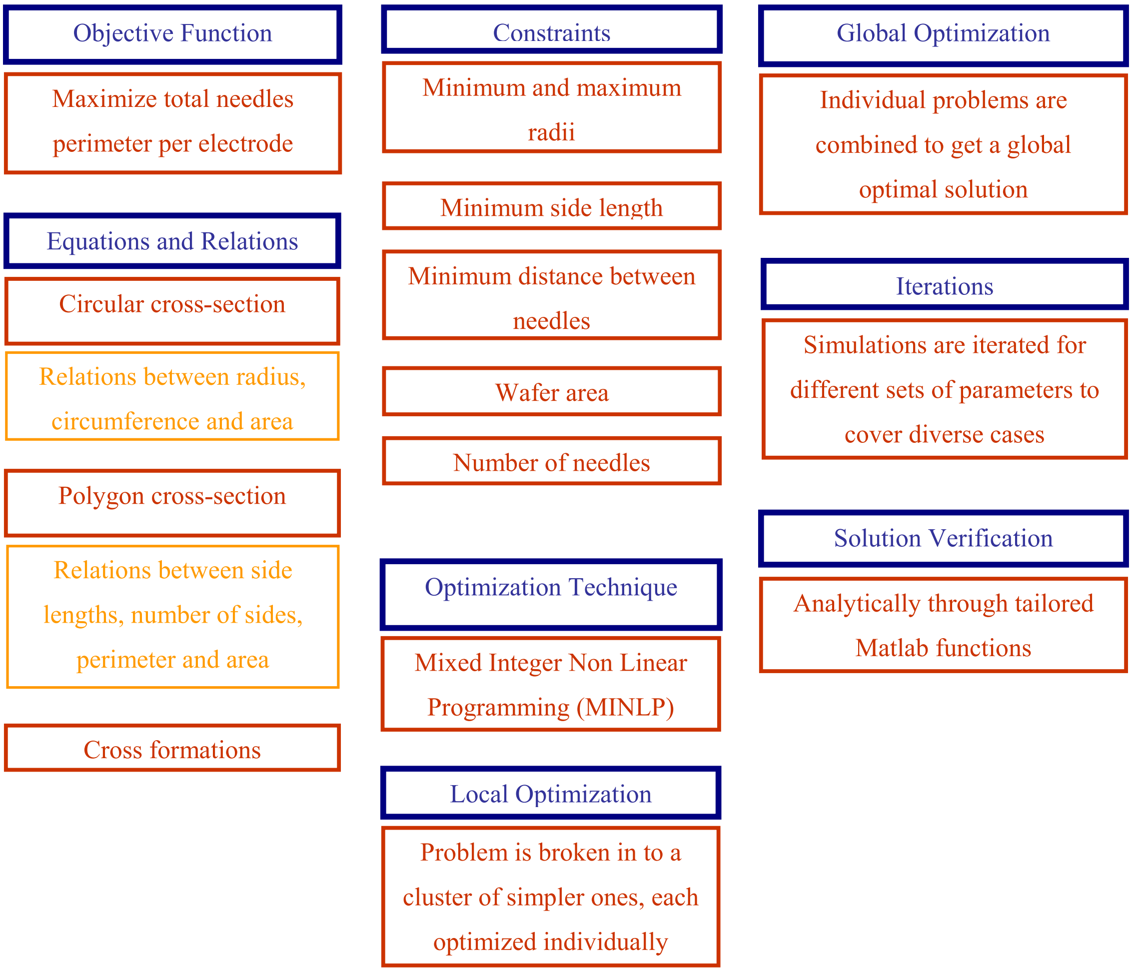

Figure 4.10 – Problem formulation

Objective function

The primary objective is to maximize the total perimeter of the needles per electrode expressed by equation 4.4, where a single electrode is formed of an array of needles. This can be achieved by packing a number of needles with cross-sectional geometry and size in a pattern to achieve maximum total perimeter in a square array.

The outcome of the analysis proposed is a set of state variables which would achieve the optimal architecture. This set of variable includes number of needles, cross-section geometry of needles, needles orientation, needle perimeter and the total area.

$$\max\left\{c^{T}\chi : A\chi \leq b, \chi \geq 0\right\} \tag{4.6}$$

where:

$c \in \mathbb{R}^{n}$ is the cost function expressed by equation 4.4 representing the total electrode perimeter which is subject to the constraint matrix $A \in \mathbb{R}^{mxn}$ which is to be satisfied by the variable vector $\chi \in \mathbb{R}^{n}$.

Equations and relations

The correlation between the geometrical parameters of the needles is formulated in sets of equations which are integrated into the optimizer and will be discussed in section 4.5.

Constraints

Pursue of the optimal needle architecture was curbed by a long list of constraints which includes physiological, mechanical, economical and fabrication limitations.

Physiological constraints

Physiological issues imposed uncompromisable constraints that have to be satisfied. Bio-compatibility and toxicity limited the choice of materials, while skin anatomy controlled the boundaries of the needles' dimensions. Material constraints are not included in the optimization model as they are more dominant on the structural and mechanical analyses.

Fabrication constraints

These depend on the micro-fabrication process technology used to manufacture the electrodes. A competent fabrication technology has to offer the required aspect ratio, minimum feature size, compatibility with the electrode materials and in the same time a reasonable price tag.

The technique used limited the minimum feature to 10 μm which represents the minimum needle diameter, minimum thickness of hollow needles and minimum needle spacing. Some of these constraints were formulated as the lower and upper bounds for variables' values, while others were included in the modeling equations for orientation and packing.

Aesthetic constraints

The electrodes were designed to have a minimal size to be aesthetically concealable. This required maximum packing of the needles to achieve maximum perimeter while keeping the area minimal.

Mechanical constraints

The mechanical performance of a needle is a function of cross-section, dimensions and material properties. Mechanical constraints are set by the normal and shear stresses and buckling loads, where the minimum dimensions of the needles that would give the needle the required mechanical strength are the lower bounds for the needles dimensions in the optimizer.

4.5.7 Optimization tools and techniques

The nature of the optimization model implied using Mixed Integer Non Linear Programming (MINLP) method to deal with the wide range of data and variable types including binary, integer and rational variables, besides to the various equations and relations.

The optimization model was created and simulated using GAMS optimization tool. Furthermore, due to the limitations of GAMS, two optimization tools were created in C++ and Matlab. The C++ optimization tool was used as a prototype to verify the optimization algorithm, and the results produced by GAMS were successfully replicated as shown in tables 4.1 and 4.2 and in figures 4.11 and 4.12. Finally, the code was further developed to run in a Matlab graphical user interface (GUI). Screenshots from the Matlab optimizer are shown in figures 4.13 and 4.14

Table 4.2 – GAMS optimization results

Circular cross-sections (circle.gms)										
nN		R		W	A_M	A_{Tot}	P	P_{Tot}	nN	R
lo	up	lo	up							
1	200	0.5-9	200	500	1250.00	2.5E5	93.900	18779.928	200	14.952
1	400	0.5-9	200	500	625.000	2.5E5	57.200	22880.090	400	9.108
1	1E3	0.5-5	200	500	314.070	2.5E5	31.407	25000	796	5.001
1	200	0.5-34	200	1E3	5000	1E6	219.199	43839.856	200	34.904
1	400	0.5-23	200	1E3	2500	1E6	145.800	58320.181	400	23.217
1	1E3	0.5-12	200	1E3	1000	1E6	80.671	80671.406	1000	12.846

Table 4.3 – Matlab optimizer optimization results

Circular cross-sections (circle11.m)								
nN		R		W	A_{Tot}	P_{Tot}	nN	R
lo	up	lo	up					
1	200	1	100	500	248820	18723.9	200	14.9
1	400	1	100	500	249832	22870.8	400	9.1
1	1000	1	100	500	249970	24994.5	780	5.1
1	200	1	100	1E3	995282	43731	200	34.8
1	400	1	100	1E3	999328	58308	400	23.2
1	1000	1	100	1E3	999552	80485.7	993	12.9

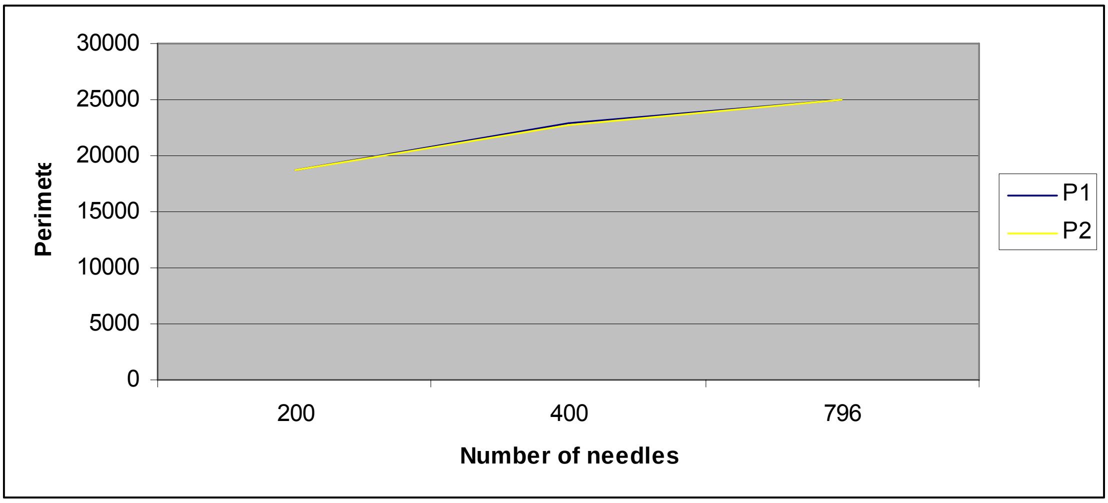

Figure 4.11 – Comparing GAMS (P1) and Matlab (P2) optimizer results – Perimeter vs. Number of needle

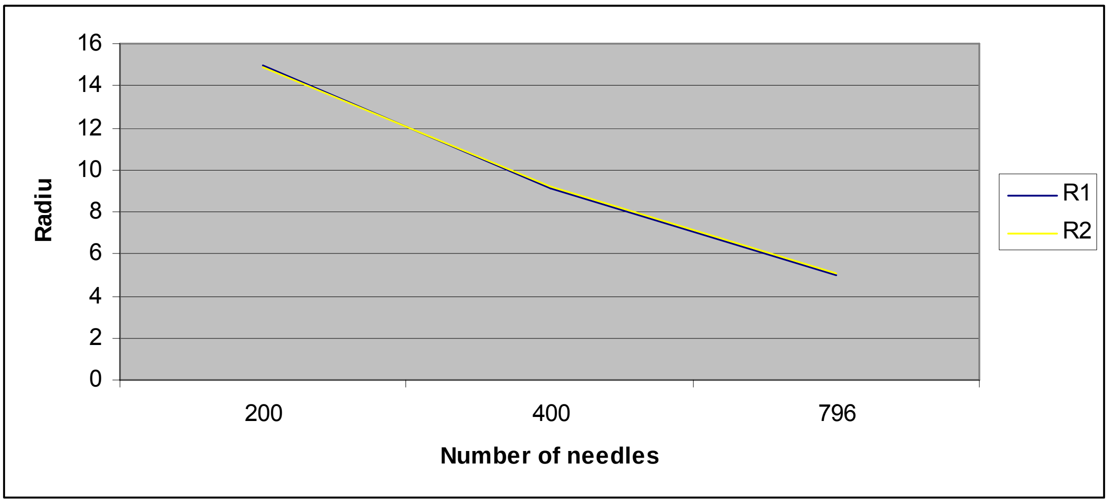

Figure 4.12 – Comparing GAMS (R1) and Matlab (R2) optimizer results – Radius vs. Number of needle

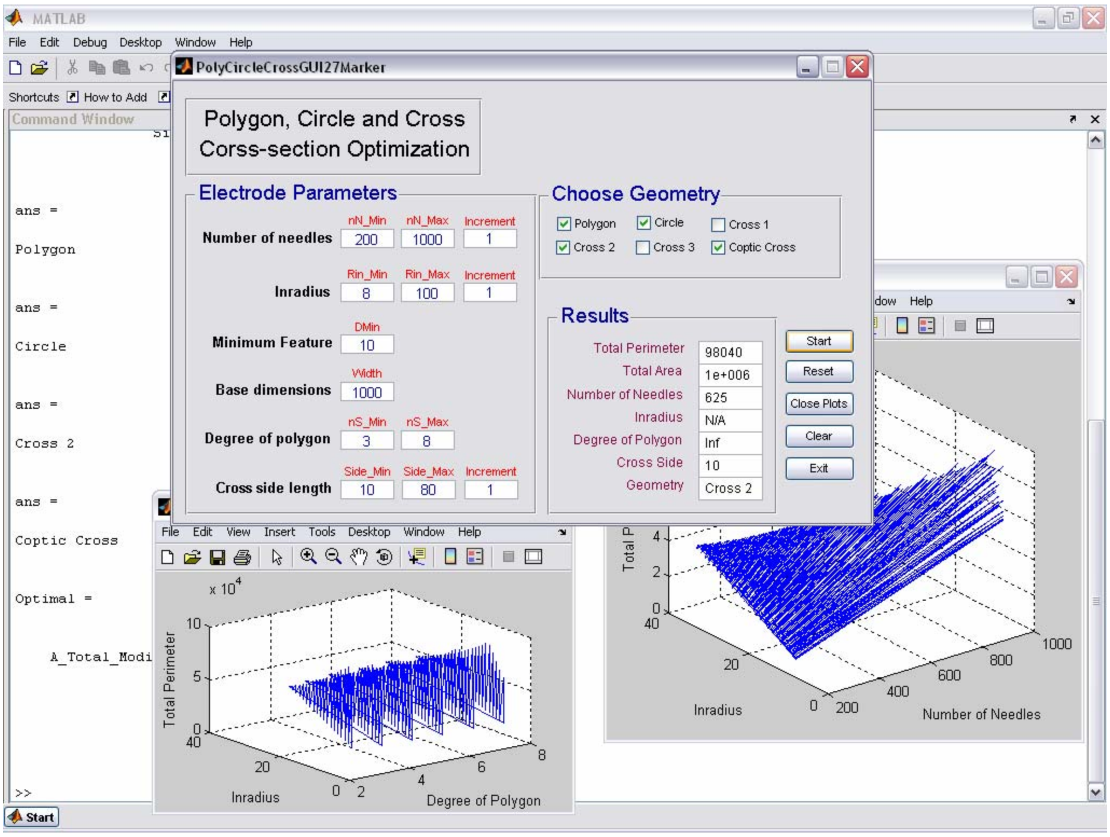

```
ans =

Polygon


ans =

Circle


ans =

Cross 2


ans =

Coptic Cross


Optimal =

   A_Total_Modi

>>
```

Polygon, Circle and Cross
Corss-section Optimization

Electrode Parameters

	nN_Min	nN_Max	Increment
Number of needles	200	1000	1
	Rin_Min	Rin_Max	Increment
Inradius	8	100	1
	DMin		
Minimum Feature	10		
	Width		
Base dimensions	1000		
	nS_Min	nS_Max	
Degree of polygon	3	8	
	Side_Min	Side_Max	Increment
Cross side length	10	80	1

Choose Geometry

☑ Polygon ☑ Circle ☐ Cross 1
☑ Cross 2 ☐ Cross 3 ☑ Coptic Cross

Results

Total Perimeter	98040
Total Area	1e+006
Number of Needles	625
Inradius	N/A
Degree of Polygon	Inf
Cross Side	10
Geometry	Cross 2

Figure 4.13 – Matlab optimizer screenshot

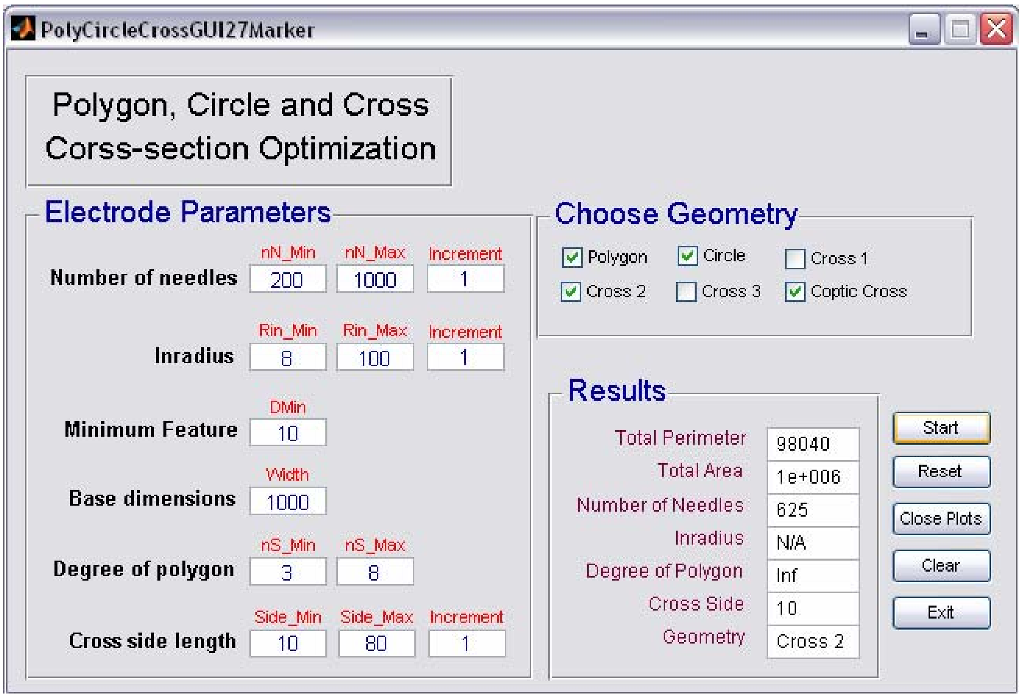

Polygon, Circle and Cross
Corss-section Optimization

Electrode Parameters

Number of needles: nN_Min 200, nN_Max 1000, Increment 1
Inradius: Rin_Min 8, Rin_Max 100, Increment 1
Minimum Feature: DMin 10
Base dimensions: Width 1000
Degree of polygon: nS_Min 3, nS_Max 8
Cross side length: Side_Min 10, Side_Max 80, Increment 1

Choose Geometry

☑ Polygon ☑ Circle ☐ Cross 1
☑ Cross 2 ☐ Cross 3 ☑ Coptic Cross

Results

Total Perimeter	98040
Total Area	1e+006
Number of Needles	625
Inradius	N/A
Degree of Polygon	Inf
Cross Side	10
Geometry	Cross 2

Figure 4.14 – Matlab optimizer screenshot

Local and global optimization

The problem was broken down to a group of sub-problems, each is optimized individually. The complexity of the model was increased gradually to accommodate more constraints. The results of local optimal solutions were useful in providing better understanding of the influence of each variable parameter and constraint on the performance of the system as well as for verifying the model consistency by comparing the fundamental blocks of the model with the analytically evaluated asymptotes and boundaries. Finally, after tuning the model parameters and equations, the local optimization problems were integrated into a single global optimization problem.

Iterations

The purpose of iterating the simulations during the process of model creation is to tune the model parameters to stabilize the system and the results converge towards the boundary values and asymptotes.

Parametric programming

Testing the influence of changing a group of parameters simultaneously was used in defining the boundaries and evaluating solutions at different operating points.

4.5.8 Case I: Optimization of circular cross sections

Starting with a simple case, the needles were realized by circular cross-sections to form an array of identical cylindrical prisms. The main purpose of this phase is to create a reliable optimization model and to understand the dynamics of the problem. Treating the circle as a polygon with a degree of ∞, the results were analyzed to identify the optimal polygon. Furthermore, the cylindrical prisms electrode will be taken as a datum to assess the performance of other geometries.

Equations and relations

The geometry of a circle was defined with a set of geometrical equations expressing the relation between the circle parameters and its dimensions (area and perimeter), the model was formulated.

$$\text{Cross -section area of a single needle} = \pi.R^2 \qquad (4.7)$$

$$\text{Perimeter of a single needle} = 2.\pi.R \qquad (4.8)$$

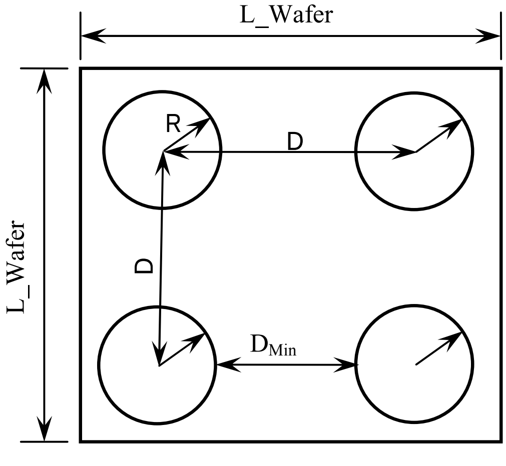

Figure 4.15 – Circular needles array

Maximum packing

Maximum packing is limited by the minimum feature size, and the minimum spacing between adjacent needles is identified as D_{Min}. The model was further developed to include maximum packing algorithm. To maximize the needles packing, information about the minimum feature size are included in the model.

$$\text{Radius}_{\text{Modified}} = \text{Radius} + \text{Half } D_{\text{Min}} \tag{4.9}$$

defining:

nN: an integer representing number of needles

W_Wafer: Wafer width defined as the wafer side length

Cross_Section_Area: cross-section area a single needle

Perimeter: perimeter of a single needle

Wafer_Area: surface area of the wafer

thus:

$$\text{Total cross-section area} = \text{nN.}\left(\text{Cross\_Section\_Area}\right) \tag{4.10}$$

$$\text{Total\_Perimeter} = \text{nN.}\left(\text{Perimeter}\right) \tag{4.11}$$

$$\text{Wafer\_Area} = \left(\text{W\_Wafer}\right)^2 \tag{4.12}$$

Constraints

The total area of all the needles were monitored to prevent overlapping the needles, and the total area was limited to the available wafer area which is the upper bound and the maximum achievable area.

$$\sum \text{Needles\_Area} \leq \text{Available wafer area} \tag{4.13}$$

where:

Needles_Area: total cross-section area of the needles

Available wafer area: total surface area of the wafer

Another set of constraints are required to avoid packing the needles in a dimension such that they will cross the wafer boundaries.

$$\sum \text{Needles\_Diameters} + \sum \text{Needle\_Spacing} \leq \text{W\_Wafer} \tag{4.14}$$

where:

Needles_Diameter: diameter of a single needle assuming a circular cross-section

Needle_Spacing: needles’ pitch

This inequality is sufficient for both dimensions because the wafer is square.

$$\text{Needle\_Pitch} - \text{Needle\_Diamater} \geq \text{Minimum needle spacing} \tag{4.15}$$

Iterations and correlation analysis showed that these constraints can be replaced with a single rule that produced more accurate results. The variables in this case are modified to include information about minimum features and spacing constraint.

$$\sum \text{Modified needles area} \leq \text{Available wafer area} \tag{4.16}$$

Results

Figure 4.16 plots a selected group of the optimal electrode parameters set which define the geometry and dimensions of the needles. The optimal results generated by GAMS listed in table 4.2 were duplicated using the Matlab-based design optimizer which are listed in table 4.3. This verifies the accuracy and reliability of the Matlab-based optimizer which was used in the design procedure.

In tables 4.2 and 4.3, A_{Tot} represents the total area consumed by the needles which is calculated based on the modified geometry which takes in consideration the minimum feature size. It is obvious that A_{Tot} attained its maximum values, proving that the technique achieved maximum needle packing. The design was implemented for two different electrode base areas; 500µ x 500µ and 1000µ x 1000µ. Doubling the electrode base area yields an expansion in the total perimeter by a factor that reaches 3.227 taking the maximum number of needles to be 1000, and the expansion factor is also boosted by increasing the number of needles in the array.

The maximum number of needles was also varied to evaluate the electrode performance under different sets of constraints. It was found that the total perimeter is a function of the product of the number of needles and the radius. The total perimeter is directly proportional to the number of needles, such that doubling the wafer size expands the total perimeter by a factor that increases with the number of needles. These results are shown in tables 4.4, 4.5 and figure 4.17. The effect of different electrode parameters as generated by the Matlab optimizer is plotted in figure 4.18 through 4.20.

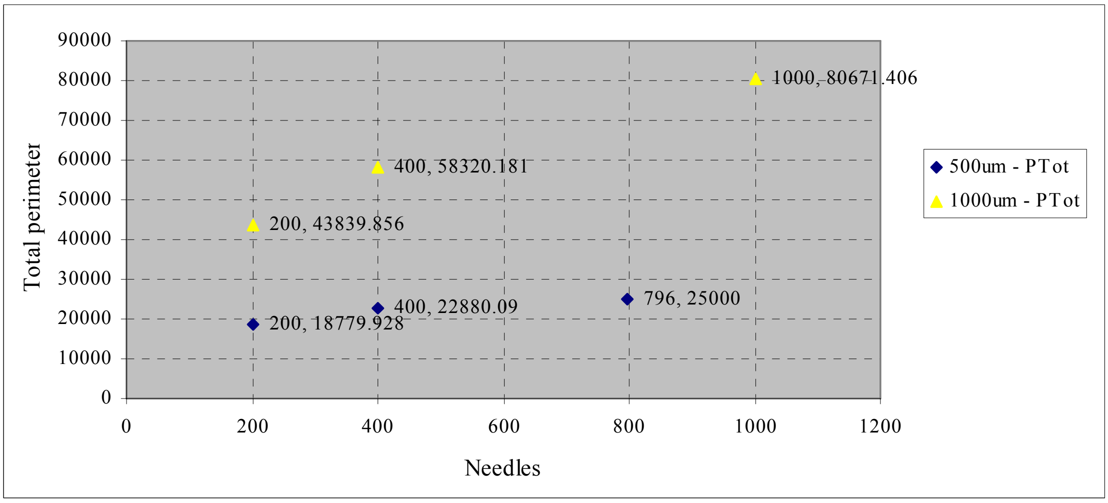

Figure 4.16 – Optimization results for circular cross-sections

Table 4.4 – Optimization results for circular cross-sections

W [µm]	nN	Total perimeter [µm]	Needle count – radius product
500	200	18779.928	2990.400
500	400	22880.090	3643.200
500	796	25000.000	3980.796
1E3	200	43839.856	6980.800
1E3	400	58320.181	9286.800
1E3	1000	80671.406	12846.000

Table 4.5 – Comparing 500 µm and 1000 µm electrode bases

# of needles	500 µm	1000 µm	P_{1000}/P_{500}
200	18779.928	43839.856	2.334
400	22880.090	58320.181	2.549
1000 | 796	25000	80671.406	3.227

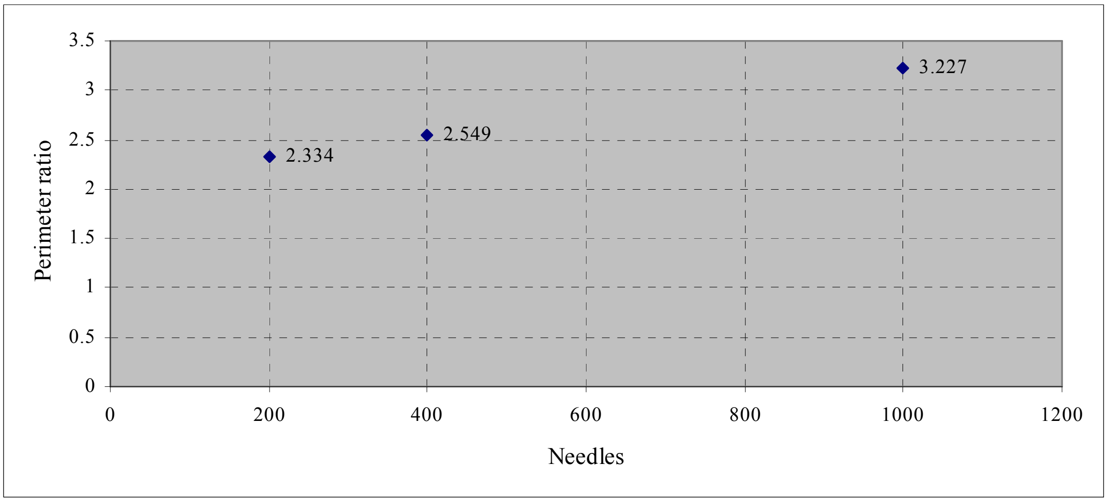

Figure 4.17 – Comparing 500 µm and 1000 µm electrode bases

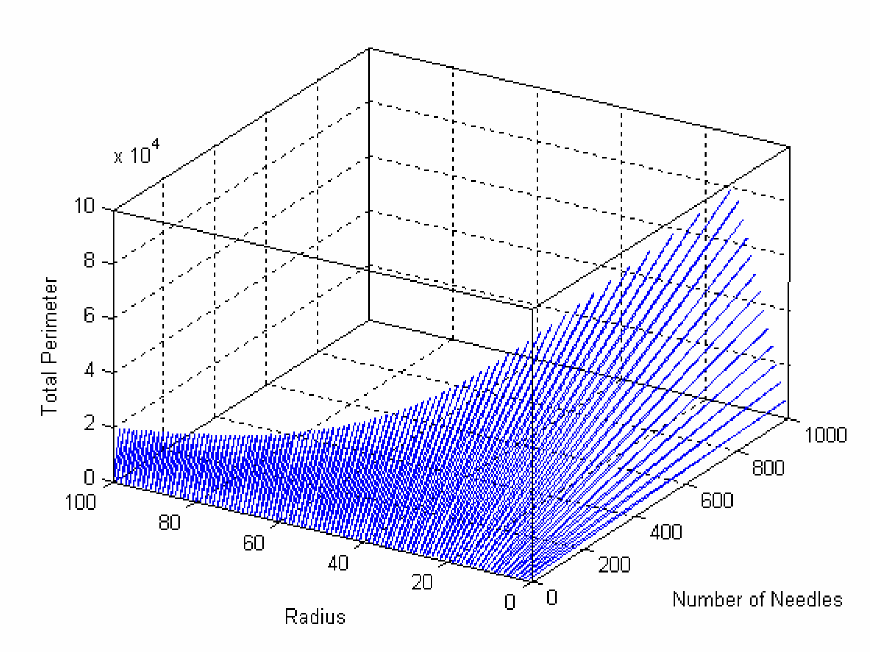

Figure 4.18 – Effect of radius and number of needles on the total perimeter

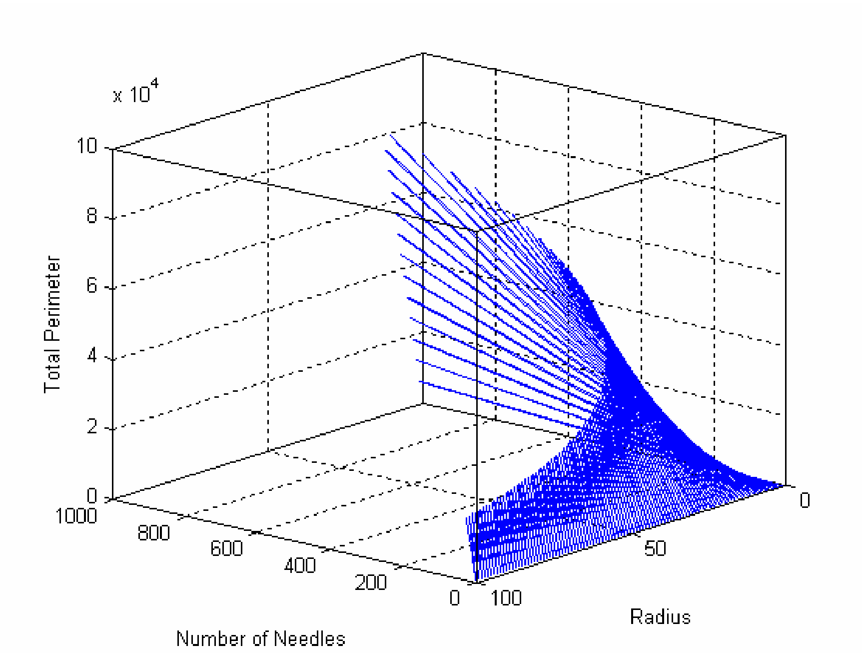

Figure 4.19 – Effect of radius and number of needles on the total perimeter

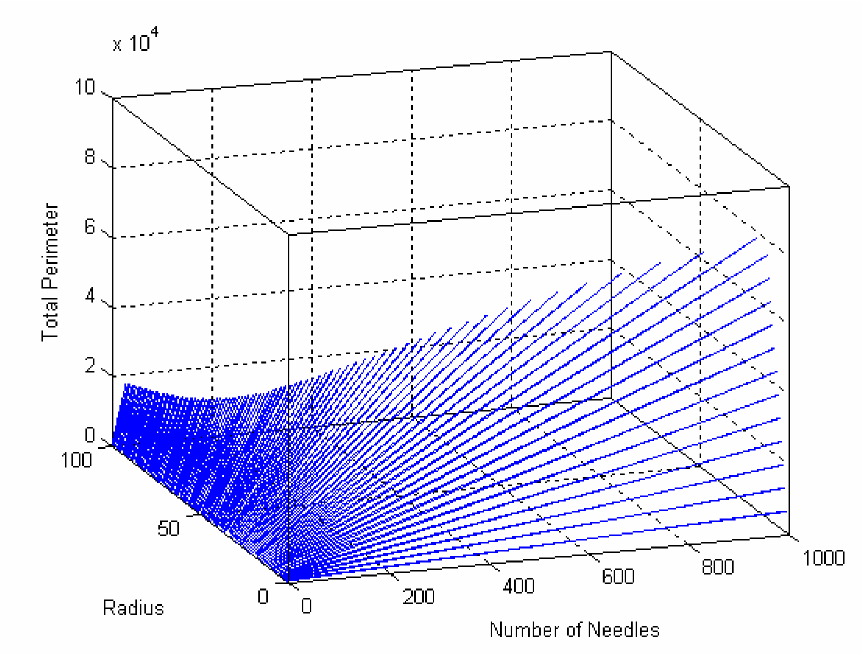

Figure 4.20 – Effect of radius and number of needles on the total perimeter

Results verification - Analytical approach

A model correlating the electrode parameters to its dimensions was used to verify the optimization results. The results provided the asymptotic boundaries for the optimal solution.

Starting with the circumference and area of the circle:

$$P = 2.\pi.r \tag{4.17}$$

$$A = \pi.r^2 \tag{4.18}$$

Let n be the number of smaller circles with radius r_n, thus;

$$P_n = 2.\pi.r_n \tag{4.19}$$

$$A_n = \pi.r_n^2 \tag{4.20}$$

Breaking down circle in figure 4.21 into n circles to achieve the same perimeter P:

$$r = n.r_n \tag{4.21}$$

and the total perimeter is:

$$P = 2.\pi.r = n.2.\pi.r_n = n.P_n \tag{4.22}$$

Summing the areas of the circles:

$$A_{total} = n.\pi.r_n^2 = n.\pi.\left(\frac{r_n}{n}\right)^2 = \pi.\frac{r_n^2}{n} \tag{4.23}$$

The same perimeter can be contained in a smaller area. The total perimeter increases as a function of the number of circles which is consistent with the simulation results where the radius proposed by the run was the minimum radius allowed by the fabrication process.

The cylindrical prism array layout is illustrated in figure 4.22 where the gray areas are the needles and the dashed circumference is void which depends on the minimum needle spacing.

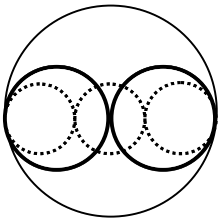

1	D
2	D/2
3	D/3

Figure 4.21– Relation between number of circles and perimeter

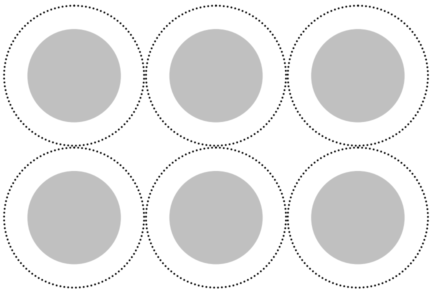

Figure 4.22 – Cylindrical electrode architecture

4.5.9 Case II: Global optimization for polygonal cross sections

The model created in case-I was further developed to be used in modeling polygonal cross-sections. The outcome of this phase will identify the uniform polygon which maximizes the perimeter for an identified area.

To be able to design for maximum packing and abide by the given constraints; the area and perimeter of polygon were described in terms of the radii of the inscribed and circumscribing circles (figure 4.23).

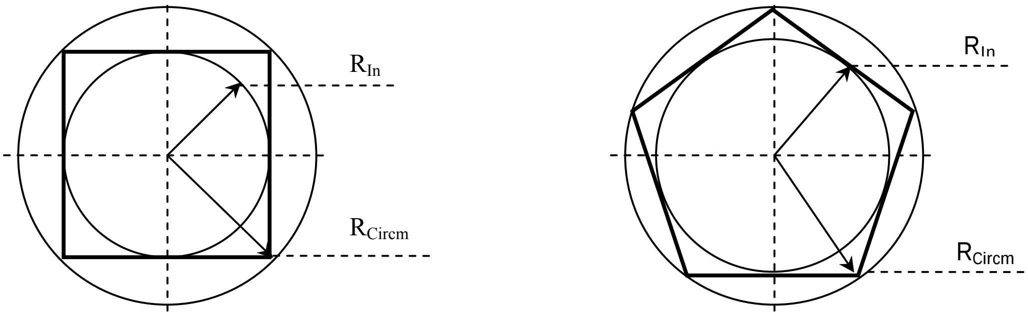

Figure 4.23 – Square and pentagonal needles

Equations

R_{In} = inradius of the inscribed circle

R_{Circm} = circumradius of the circumscribing circle

nS = number of sides

$$\text{Cross\_Section\_Area} \;=\; \text{nS}.\left(\text{R}_{\text{In}}\right)^2.\tan\left(\frac{\pi}{\text{nS}}\right)=\frac{\text{nS}.\left(\text{R}_{\text{Circm}}\right)^2}{2}.\sin\left(\frac{2.\pi}{\text{nS}}\right) \tag{4.24}$$

$$\text{Perimeter} = 2.\text{nS}.\text{R}_{\text{In}}.\tan\left(\frac{\pi}{\text{nS}}\right) = \text{nS}.\text{R}_{\text{Circm}}.\sin\left(\frac{\pi}{\text{nS}}\right) \tag{4.25}$$

nN = an integer representing number of needles

$$\text{Total\_Cross\_Section\_Area} \;=\; \text{nN}.\left(\text{Cross\_Section\_Area}\right) \tag{4.26}$$

$$\text{Total\_Perimeter} = \text{nN}.\left(\text{Perimeter}\right) \tag{4.27}$$

$$\text{Wafer\_Area}=\left(\text{L\_Wafer}\right)^2 \tag{4.28}$$

The area equation was modified to produce a maximum packed array of needles.

Results

The total perimeter is affected by different factors including needle geometry, dimensions, number as well as the electrode base area. Tables 4.6 and 4.7 show the effect of needle parameters on the total perimeter. In figure 4.24, it is obvious that the total perimeter increases as a function of the number off needles and the electrode base area.

Table 4.6 – Optimization results for polygonal cross-sections

Polygonal cross-sections (Polygon.gms)														
nS		nN		Rin		W	A_M	A_{Tot}	P	P_{Tot}	nS	nN	Rin	Rcircm
lo	up	lo	up	lo	up									
3	10	1	200	10	200	500	1250	2.5E5	109.189	21837.773	3	200	10.520	21.020
3	10	1	400	5	200	500	625.000	2.5E5	62.008	24803.060	3	400	5.974	11.937
3	10	1	1000	5	200	500	519.751	2.5E5	51.975	24999.986	3	481	5.007	10.006
3	10	1	200	26	200	1E3	5000	1E6	270.276	54055.121	3	200	26.039	52.031
3	10	1	400	16	200	1E3	2500	1E6	175.913	70365.271	3	400	16.948	33.865
3	10	1	1000	8	200	1E3	1000	1E6	92.182	92182.485	3	1E3	8.881	17.746

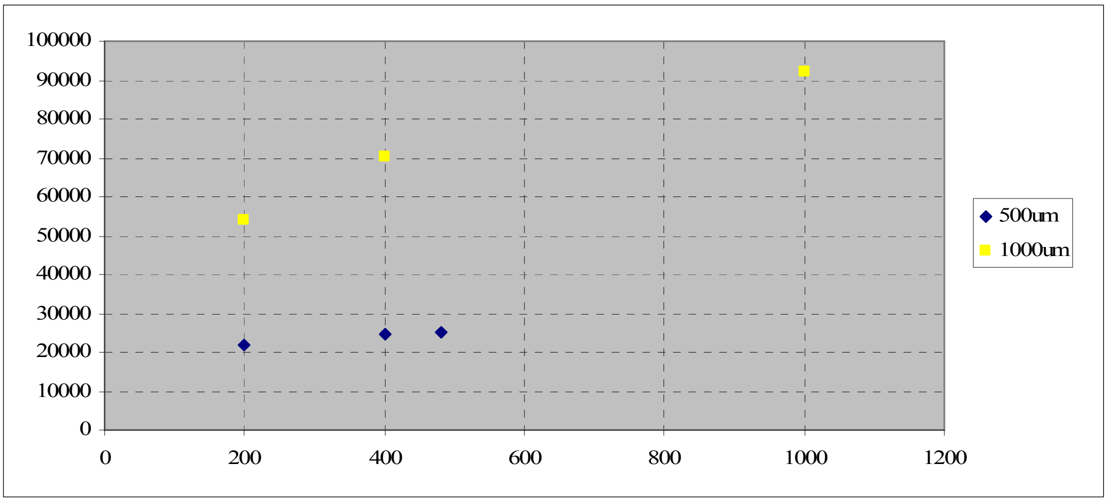

Figure 4.24 – Optimization results for polygonal cross-sections

Table 4.7 – Effect of electrode base area on electrode perimeter

W	nN	Total perimeter	Needles count – radius product
500	200	21837.773	2104.000
500	400	24803.060	2389.600
500	796	24999.986	2408.367
1E3	200	54055.121	5207.800
1E3	400	70365.271	6779.200
1E3	1000	92182.485	8881.000

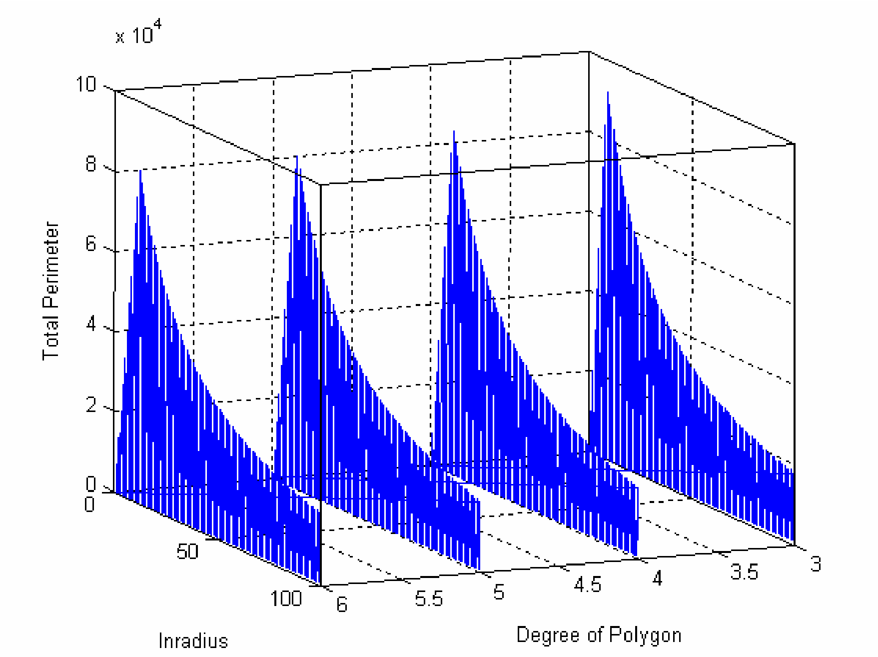

Figure 4.25 – Effect of dimensions and degree of polygon on the total perimeter

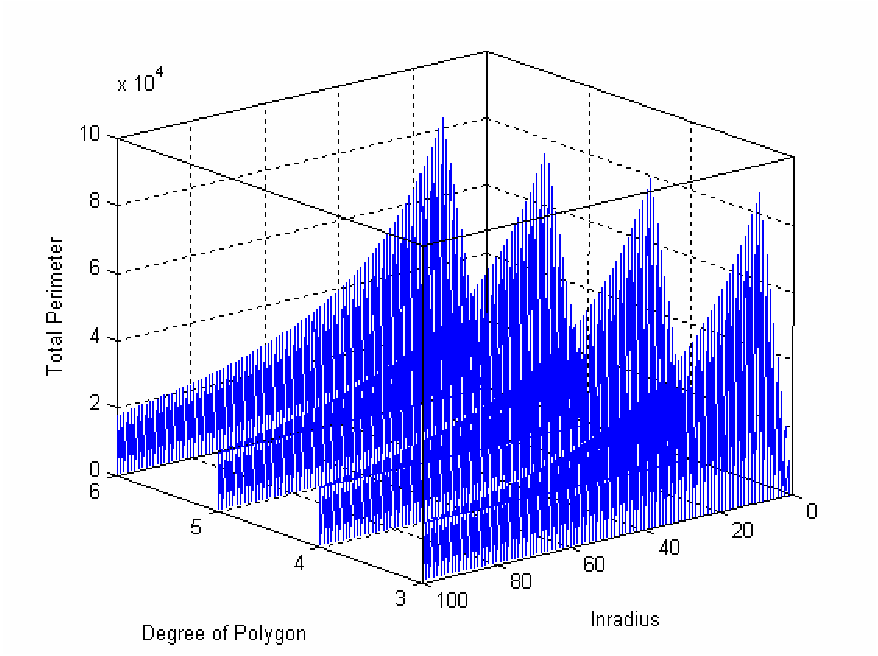

Figure 4.26 – Effect of dimensions and degree of polygon on the total perimeter

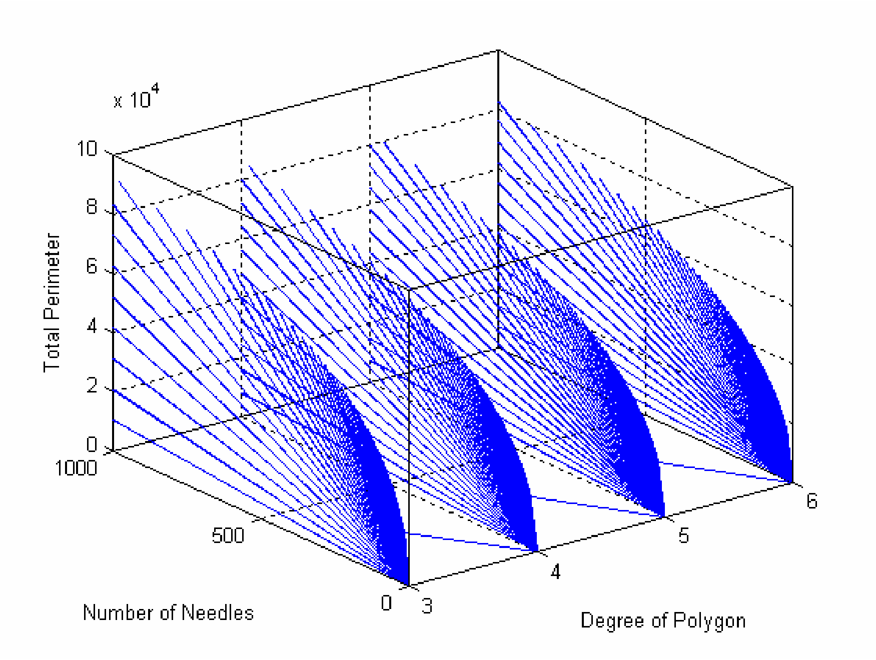

Figure 4.27 – Effect of number of needles and degree of polygon on the total perimeter

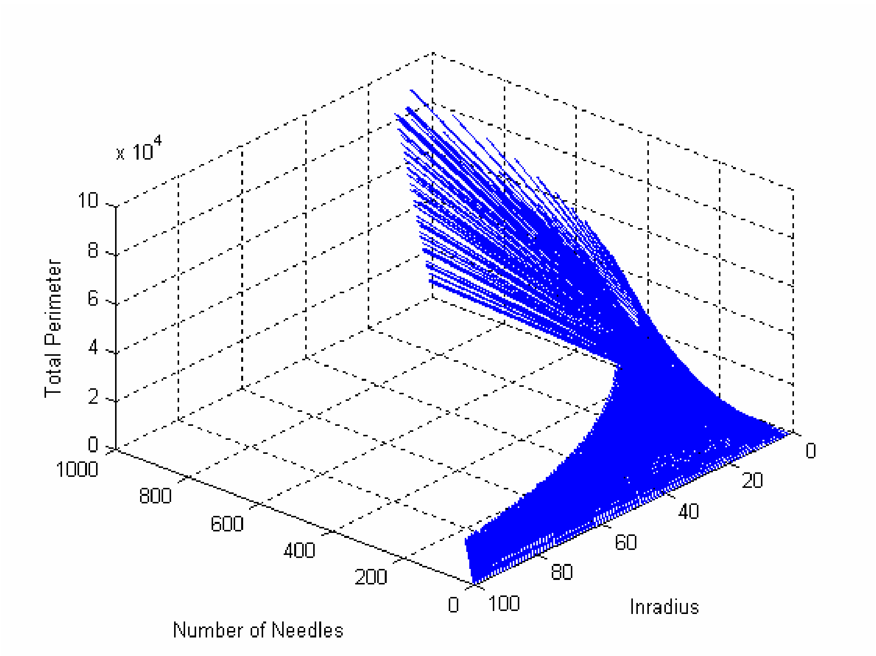

Figure 4.28 – Effect of dimensions and number of needles on the total perimeter

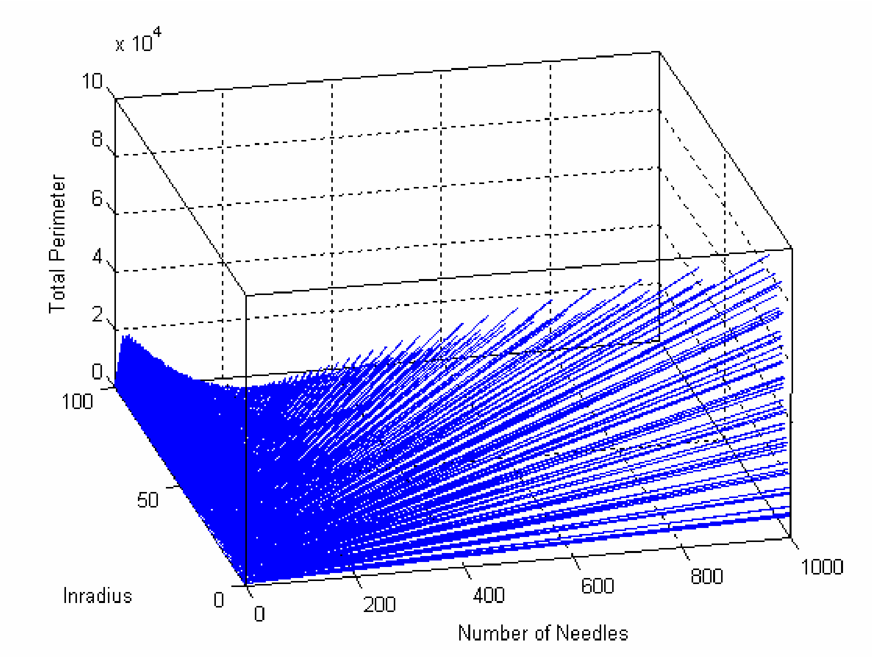

Figure 4.29 – Effect of dimensions and number of needles on the total perimeter

Another factor that affects the total perimeter is the electrode base area. Referring to table 4.8 and figure 4.30, doubling the electrode base area will expand the total perimeter by a factor that increases with the base area (figure 4.31). Increasing the base dimensions from 500μ x 500μ to 1000μ x 1000μ will expand the perimeter by a factor of 3.6873.

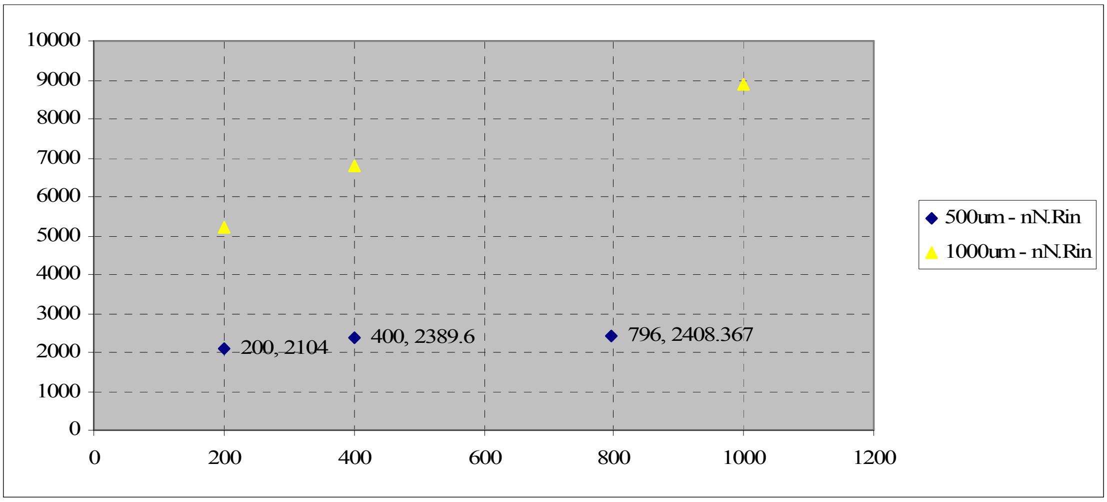

Figure 4.30 – Total perimeter for 500µm and 1000µm electrode base

Table 4.8 – Effect of electrode base on the total perimeter

# of needles	500 µm	1000 µm	
200	21837.773	54055.121	2.4753
400	24803.060	70365.271	2.8370
1000 - 796	24999.986	92182.485	3.6873

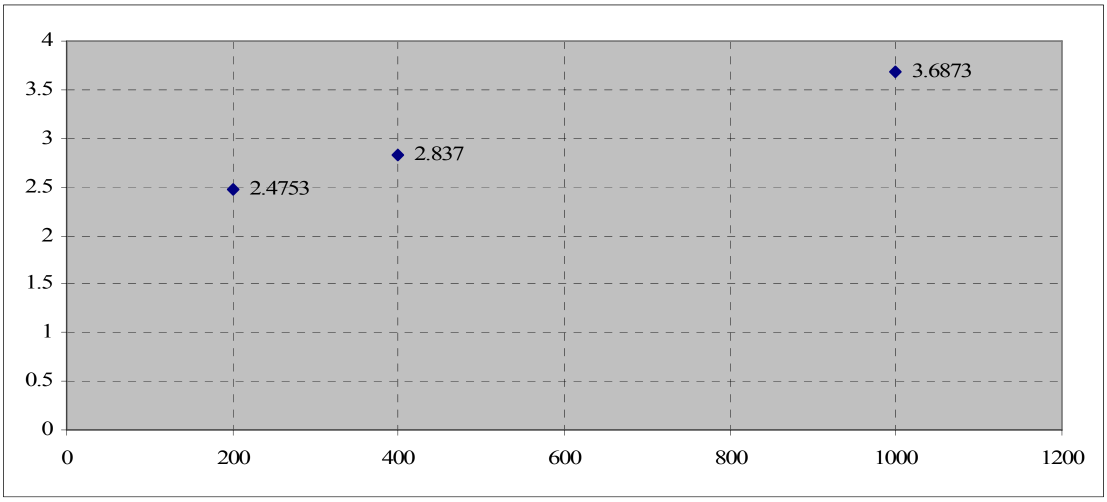

Figure 4.31 – Effect of electrode base on the total perimeter

Studying the dependence of the total perimeter on the electrode geometry required a sensitivity analysis where the geometry was changed keeping the rest of the parameters at fixed values. The results are shown in table 4.9. In the case of polygonal cross-sections, and strictly for the applied constraints; an array of triangular prisms will provide the maximum perimeter per electrode base area.

Table 4. 9 – Dependence of the total perimeter on the electrode geometry

nS	nN		Rin		W	A_M	A_{Tot}	P	P_{Tot}	nS	nN	Rin	Rcircm
	lo	up	lo	up									
3	1	200	0.5	200	1E3	5000	1E6	270.276	54055.121	3	200	26.039	52.031
4	1	200	0.5	200	1E3	5000	1E6	242.762	48552.392	4	200	30.369	42.932
5	1	200	0.5	200	1E3	5000	1E6	233.151	46630.292	5	200	32.112	39.683
6	1	200	0.5	200	1E3	5000	1E6	228.514	45702.868	6	200	33.003	38.103
7	1	200	0.5	200	1E3	5000	1E6	225.888	45177.661	7	200	33.524	37.205
8	1	200	0.5	200	1E3	5000	1E6	224.247	44849.358	8	200	33.855	36.642
9	1	200	0.5	200	1E3	5000	1E6	223.149	44629.705	9	200	34.080	36.264
10	1	200	0.5	200	1E3	5000	1E6	222.376	44475.207	10	200	34.239	35.999
∞	1	200	0.5	200	1E3	5000	1E6	219.199	43839.856	∞	200	34.904	34.904
3	1	400	0.5	200	1E3	2500	1E6	175.913	70365.271	3	400	16.948	33.865
4	1	400	0.5	200	1E3	2500	1E6	159.952	63980.889	4	400	20.010	28.287
5	1	400	0.5	200	1E3	2500	1E6	154.230	61692.054	5	400	21.242	26.251
6	1	400	0.5	200	1E3	2500	1E6	151.444	60577.656	6	400	21.872	25.252
7	1	400	0.5	200	1E3	2500	1E6	149.859	59943.761	7	400	22.241	24.682
8	1	400	0.5	200	1E3	2500	1E6	148.866	59546.505	8	400	22.475	24.325
9	1	400	0.5	200	1E3	2500	1E6	148.201	59280.288	9	400	22.633	24.084
10	1	400	0.5	200	1E3	2500	1E6	147.732	59092.833	10	400	22.746	23.915
∞	1	400	0.5	200	1E3	2500	1E6	145.800	58320.181	∞	400	23.217	23.217
3	1	1E3	0.5	200	1E3	1000	1E6	92.182	92182.485	3	1E3	8.881	17.746
4	1	1E3	0.5	200	1E3	1000	1E6	86.473	86472.593	4	1E3	10.818	15.292
5	1	1E3	0.5	200	1E3	1000	1E6	84.201	84200.809	5	1E3	11.597	14.331
6	1	1E3	0.5	200	1E3	1000	1E6	83.057	83057.374	6	1E3	11.996	13.849
7	1	1E3	0.5	200	1E3	1000	1E6	82.397	82396.612	7	1E3	12.228	13.571
8	1	1E3	0.5	200	1E3	1000	1E6	81.979	81978.797	8	1E3	12.377	13.395
9	1	1E3	0.5	200	1E3	1000	1E6	81.697	81697.222	9	1E3	12.477	13.277
10	1	1E3	0.5	200	1E3	1000	1E6	81.498	81498.200	10	1E3	12.548	13.193
∞	1	1E3	0.5	200	1E3	1000	1E6	80.671	80671.406	∞	1E3	12.846	12.846

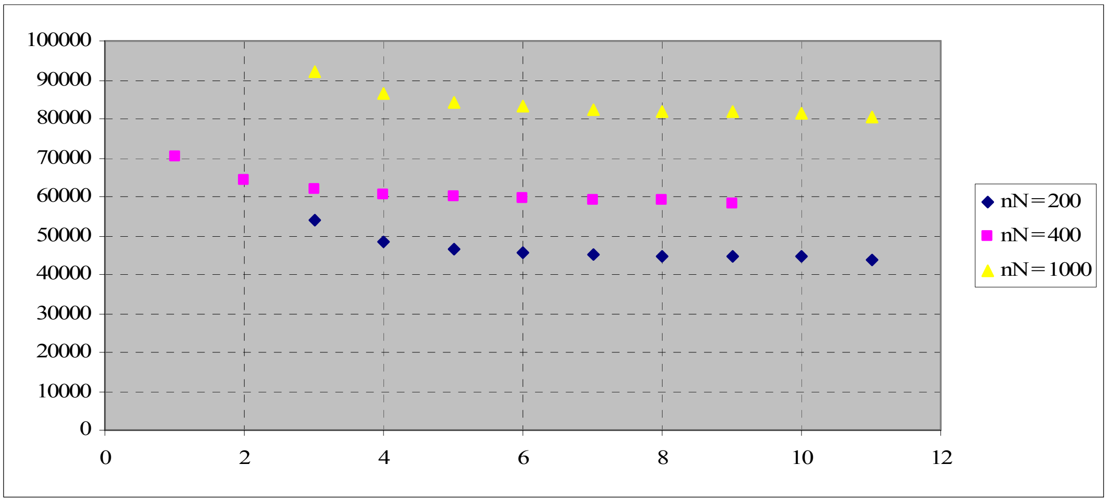

Figure 4.32 – Dependence of total perimeter on needle geometry

A comparison between triangular and cylindrical prisms in table 4.10 demonstrates the improvement achieved. The plotted results in figure 4.32 illustrate the increase in total perimeter provided by the triangular cross-sections.

Table 4.10 – Comparing triangular and circular cross-sections

nS	nN		Rin		W	A_M	A_{Tot}	P	P_{Tot}	nS	nN	Rin	Rcircm
	lo	up	lo	up									
3	1	200	1	200	500	1250	2.5E5	109.189	21837.773	3	200	10.520	21.020
3	1	400	1	200	500	625	2.5E5	62.008	24803.060	3	400	5.974	11.937
3	1	481	1	200	500	519.75	2.5E5	51.975	24999.986	3	481	5.007	10.006
3	1	1E3	1	200	500	417.36	2.5E5	417.362	24988.540	4	599	5.219	7.378
3	1	200	0.5	200	1E3	5000	1E6	270.276	54055.121	3	200	26.039	52.031
3	1	400	0.5	200	1E3	2500	1E6	175.913	70365.271	3	400	16.948	33.865
3	1	1E3	0.5	200	1E3	1000	1E6	92.182	92182.485	3	1E3	8.881	17.746
∞	1	200	0.5	200	500	1250.0	2.5E5	93.900	18779.928	∞	200	14.952	14.952
∞	1	400	0.5	200	500	625.00	2.5E5	57.200	22880.090	∞	400	9.108	9.108
∞	1	1E3	5	200	500	314.07	2.5E5	31.407	25000	∞	796	5.001	5.001
∞	1	200	34	200	1E3	5000	1E6	219.199	43839.856	∞	200	34.904	34.904
∞	1	400	23	200	1E3	2500	1E6	145.800	58320.181	∞	400	23.217	23.217
∞	1	1E3	12	200	1E3	1000	1E6	80.671	80671.406	∞	1E3	12.846	12.846

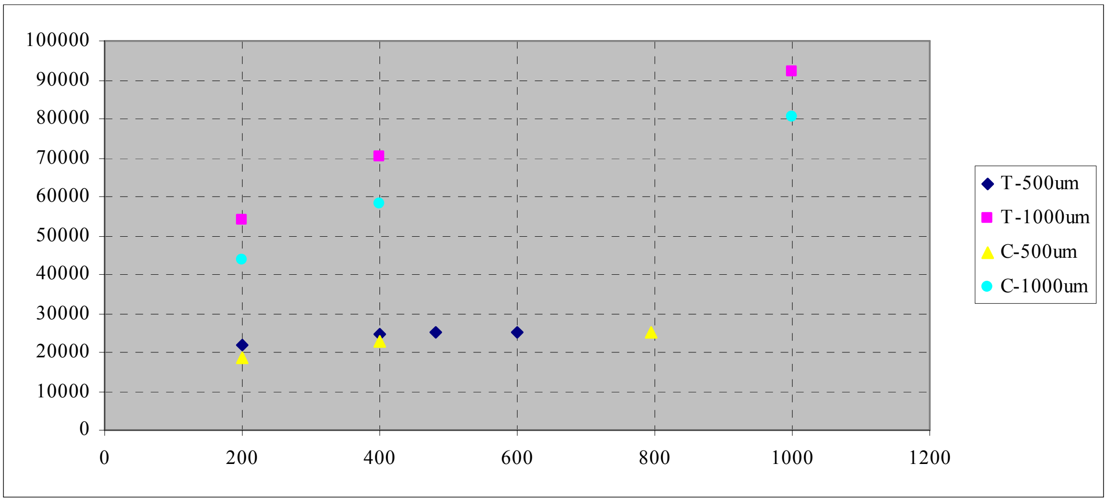

Figure 4.33 – Comparing triangular and circular cross-sections

The perimeter expansion factor when replacing cylindrical prisms with triangular ones is a function of the electrode base area as well as the number of needles. An array of 200 needles will provide a 23% gain in perimeter as shown in table 4.11. In the case of 1000 needles, the gain drops to a value of 14.27% because the perimeters have close values.

Table 4.11 – Perimeter expansion factor of triangular cross-section

L = 500 µm	nS = 3	nS = ∞	ratio
200	21837.773	18779.928	1.1628
400	24803.060	22880.090	1.0840

Table 4.12 – Perimeter expansion factor of triangular cross-section

L = 1000 µm	nS = 3	nS = ∞	ratio
200	54055.121	43839.856	1.2330
400	70365.271	58320.181	1.2065
1000	92182.485	80671.406	1.1427

Results verification - Analytical approach

The results of the analytical approach in figures 4.34 and 4.35 show that to achieve a required perimeter, a lower degree polygon will consume a smaller area than a higher degree polygon. Fixing the perimeter at a constant value; the area of the polygon increases as the number of sides increases (the degree of polygon increases). When the degree of polygon reaches a values of 30, the area approaches a saturation value which is equivalent to the area of a circle which is considered an infinite degree polygon. This is consistent with model results where the optimal perimeter is achieved in the case of a triangular cross section.

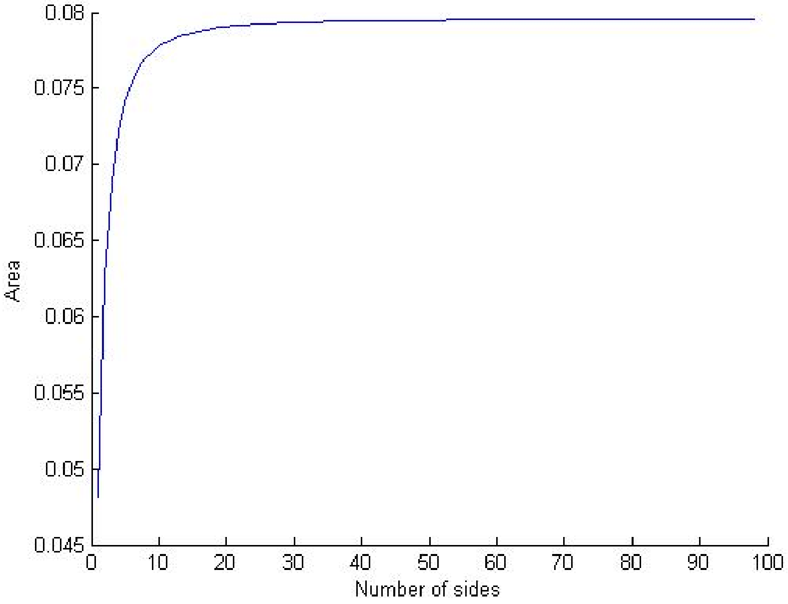

Figure 4.34 – Relation between number of sides and area for a constant perimeter

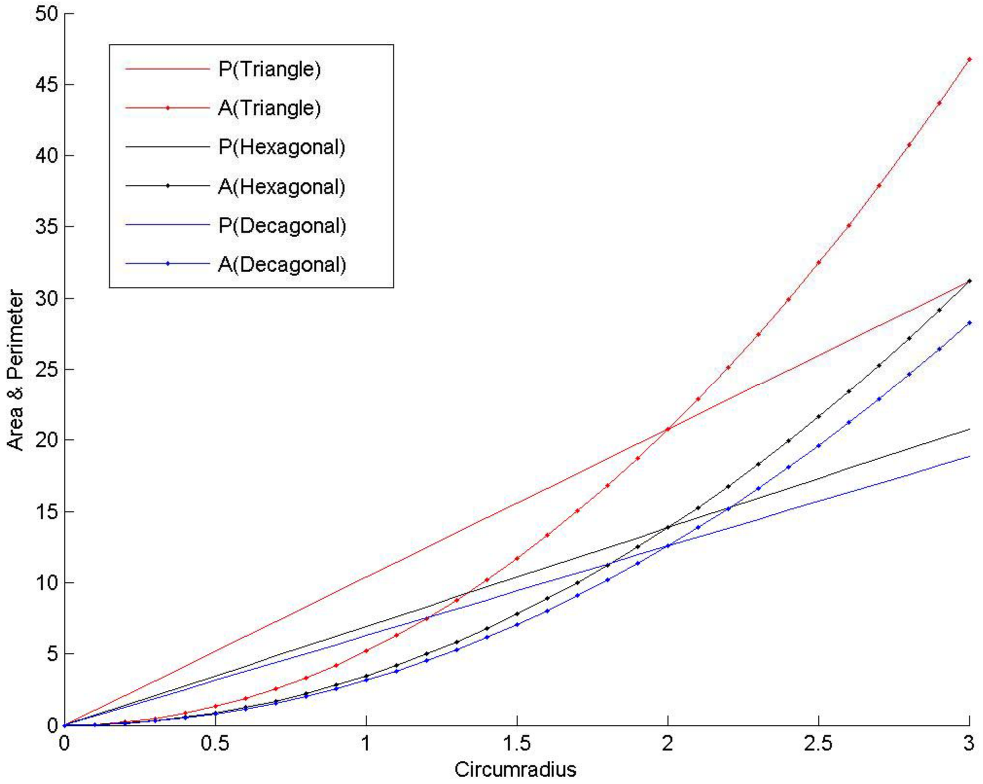

Figure 4.35 – Relation between number of sides, area and perimeter

4.5.10 Case III: Local optimization for equilateral triangles

Based on the results of case II; a triangular cross-section will provide the optimal solution to get the maximum perimeter in an available area. The simulation model in this phase is customized for triangular prisms then the results are compared with the global optimization results.

Equations

Heron's formula:

For triangle T in figure 4.36:

$$\text{Perimeter} = 2.S = A + B + C \tag{4.29}$$

$$\text{Area} = \sqrt{S.(S-A).(S-B).(S-C)} \tag{4.30}$$

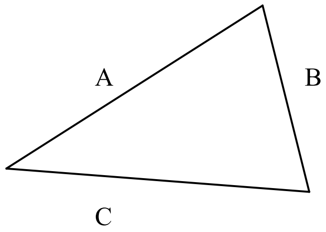

Figure 4.36 – Heron's formula

Constraints

Area constraint:

$$nN.(Area)<(Wafer\_Area) \tag{4.31}$$

Results verification - Analytical approach

$$A+B+C=2.S \tag{4.32}$$

$$Area=\sqrt{S.(S-A).(S-B).(S-C)} \tag{4.33}$$

The arithmetic mean inequality:

$$(S-A).(S-B).(S-C)\leq\left(\frac{(S-A)+(S-B)+(S-C)}{3}\right)^3 \tag{4.34}$$

$$(S-A).(S-B).(S-C)\leq\left(\frac{3.S-A-B-C}{3}\right)^3 \tag{4.35}$$

$$(S-A).(S-B).(S-C)\leq\left(\frac{3.S-(A+B+C)}{3}\right)^3 \tag{4.36}$$

$$(S-A).(S-B).(S-C)\leq\left(\frac{3.S-2.S}{3}\right)^3 \tag{4.37}$$

$$(S-A).(S-B).(S-C)\leq\frac{S^3}{27} \tag{4.38}$$

Equality occurs when:

$$S - A = S - B = S - C \tag{4.39}$$

Thus:

$$A = B = C \tag{4.40}$$

Since the product is always less than $\frac{S^2}{3.\sqrt{3}}$, this constant is the maximum for the product and the maximum area of a triangle with a fixed perimeter 2.S is:

$$\text{Area}=\sqrt{\frac{S.\left(S^3\right)}{27}}=\frac{S^2}{3.\sqrt{3}} \tag{4.41}$$

As a result; the equilateral triangle consumes the largest area to have a certain perimeter, but regardless of this result; it will be used in implementing the needles due to fabrication constraints. Resorting to the equilateral triangles, the architecture in figure 4.37 is the proposed optimal solution which maximizes the perimeter while keeping the area minimal and abiding by the constraints.

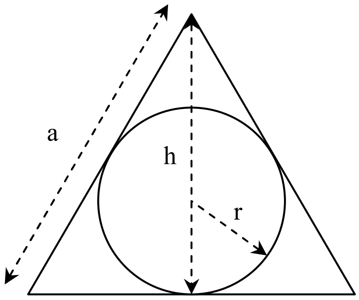

Figure 4.37 – Equilateral triangle

$$r=a.\frac{\sqrt{3}}{6} \tag{4.42}$$

$$h = a.\frac{\sqrt{3}}{2} \qquad (4.43)$$

The cell used to maximize the packing is sketched in figure 4.38. The shaded region is the electrode and it is surrounded by a shell which represents the smallest gap allowed between the adjacent needles whose value is controlled by fabrication constraints.

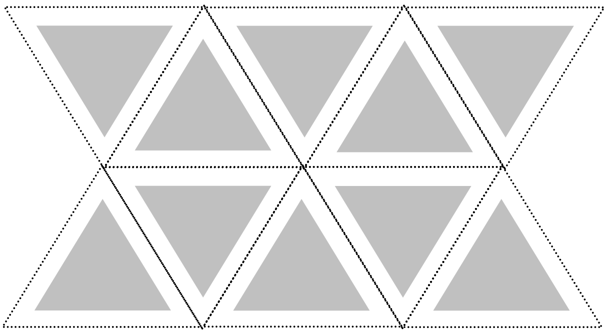

Figure 4.38 – Electrode architecture

Results

The simulation results show that increasing the number of needles while minimizing the radius of each needle will result in an increase in the total perimeter of all needles. This is confirmed by the analytical derivation and its results.

Regarding the geometry and cross-section; a certain perimeter can be achieved by different polygons, but the one that consumes the least area is the lowest degree polygon. In this case, a triangular cross-section provides the smallest area. This is consistent with the analytical results. This will result in increasing the density of needles and consequently, expanding the total perimeter.

4.5.11 Case IV: Hollow triangular needles

Another improvement to maximize the perimeter is using hollow needles (figure 4.39) to make use of the inner perimeter as well. The fabrication constraints impose the smallest feature size to be 10 μm. Thus the smallest radius of the inscribing circle of the triangular base is 15 μm, and the side lengths of the external and internal triangles will be 51.9615 μm and 17.3205 μm consequently.

Packing hollow needles with inradius of 5μm and a thickness of 10 μm in a 1000 μm x 1000 μm base requires 481 needles. The combined perimeter in this design is 99973.5 μm, which yields an 8.45% increase in the perimeter compared to the optimal solution of 1000 triangular prisms with a total perimeter of 92182.485 μm, and 24% when compared to cylindrical prisms.

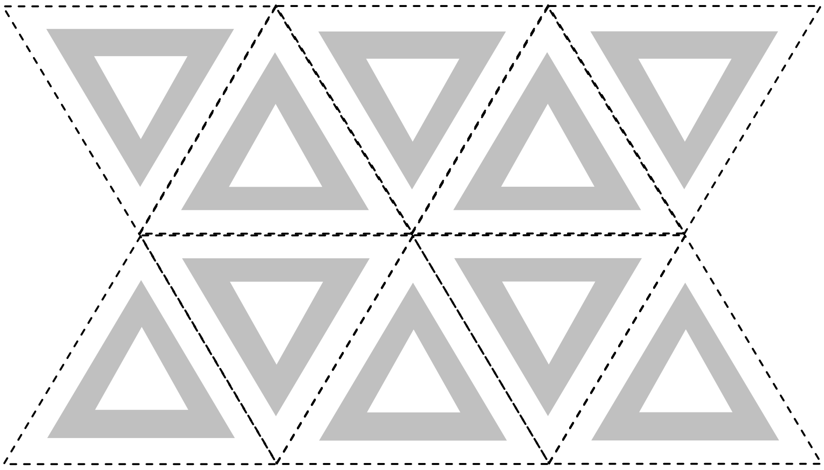

Figure 4.39 – Electrode architecture

4.5.12 Case V: Cross formations

More complicated geometries were explored seeking larger perimeters. These included ribbed structures, for example star shapes e.g. the Benz-star, the Cross and pentagrams. The Cross (4 point star) was characterized by the best packing.

Various layouts for Cross formations were proposed and experimented to identify the most appropriate layout. The formation starts with an assembly of basic crosses to exploit the available area in figure 4.40, then this was followed by filling the void between the crosses with square needles as described in figure 4.42, and finally T-sections was used as shown in figure 4.44.

Results

A sequence of parameter correlation analysis were executed (table 4.13) and the maximum perimeter was produced by Design-1 where a perimeter of 99960 μm is obtained by 833 needles on a 1000μ x 1000μ electrode base and minimum feature of 10 μm and this perimeter can reach 152100 μm if the fabrication technology allows a minimum feature of 3 μm.

Design-1 offers an expansion of 23.9% compared to cylindrical prisms which can be elevated to 51% if the minimum feature can be reduced to 3 μm.

Design 1

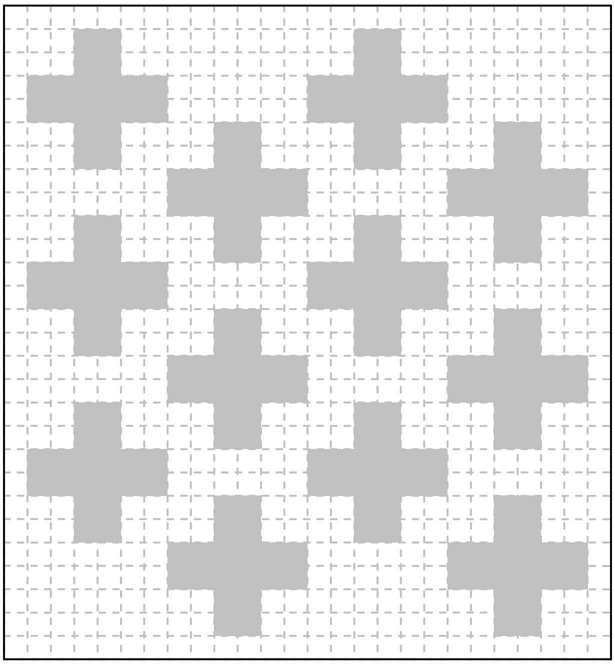

Figure 4.40 – Cross Design 1

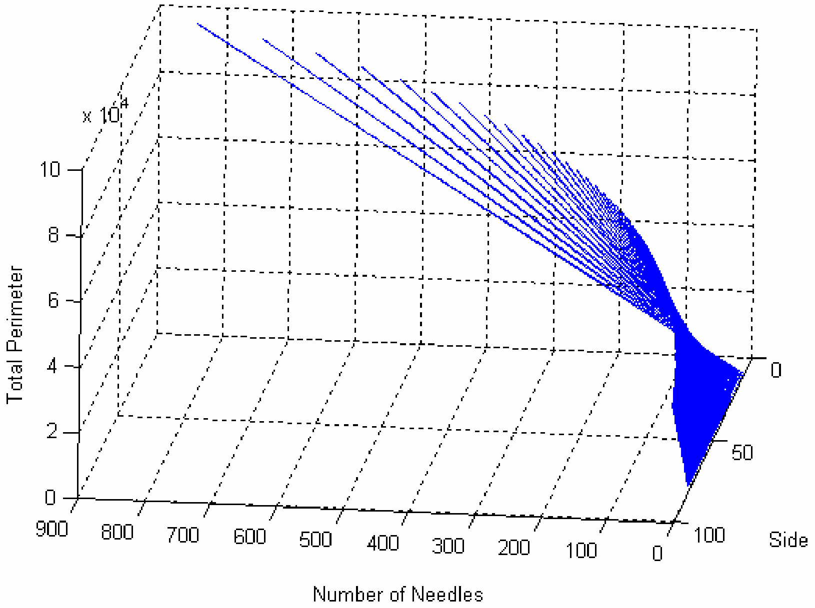

Figure 4.41 – Effect of needle dimensions and number of needles

Table 4.13 – Design 1 optimal results

Cross 1				
nN_{Max}	A_{Tot}	P_{Tot}	nS	Side
200	997920	61776	198	26
400	997785	79356	389	17
600	998775	90324	579	13
800	999180	96624	732	11
1000	999600	99960	833	10

Design 2

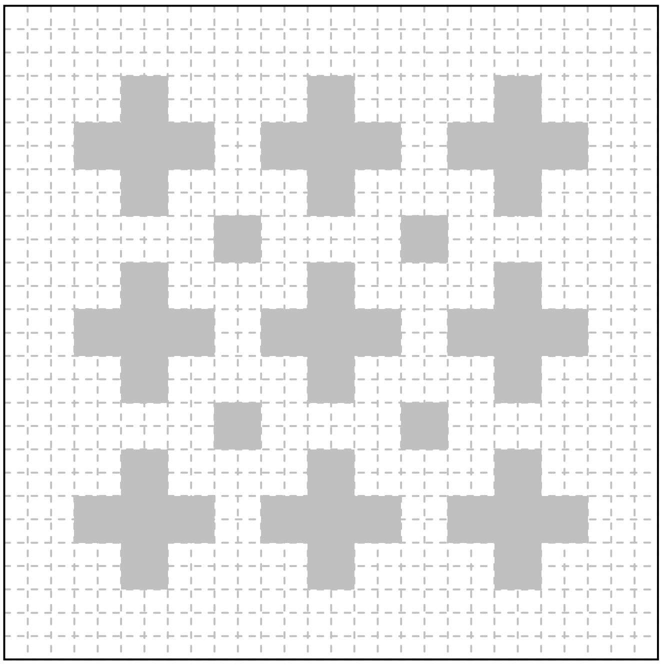

Figure 4.42 – Cross Design 2

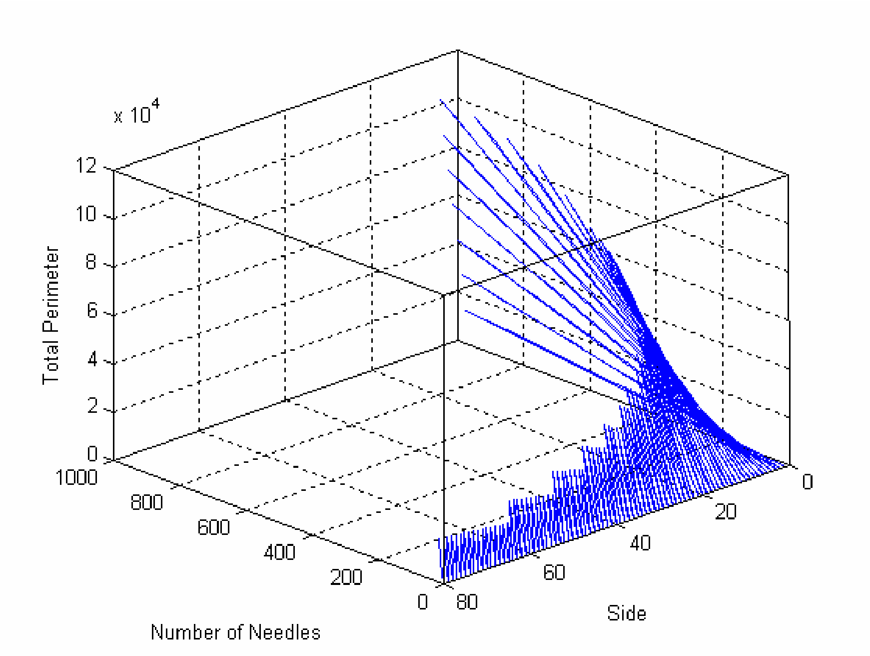

Figure 4.43 – Effect of needle dimensions and number of needles

Table 4.14 – Design 2 optimal results

Cross 2					
nN_{Max}	A_{Tot}	P_{Tot}	nN	nS	nN_{Max}
Cross 2	200	960400	60560	196	20
	400	960400	81172	400	13
	600	978121	91124	529	11
	800	1000000	98040	625	10
	1000	1000000	98040	625	10

Design 3

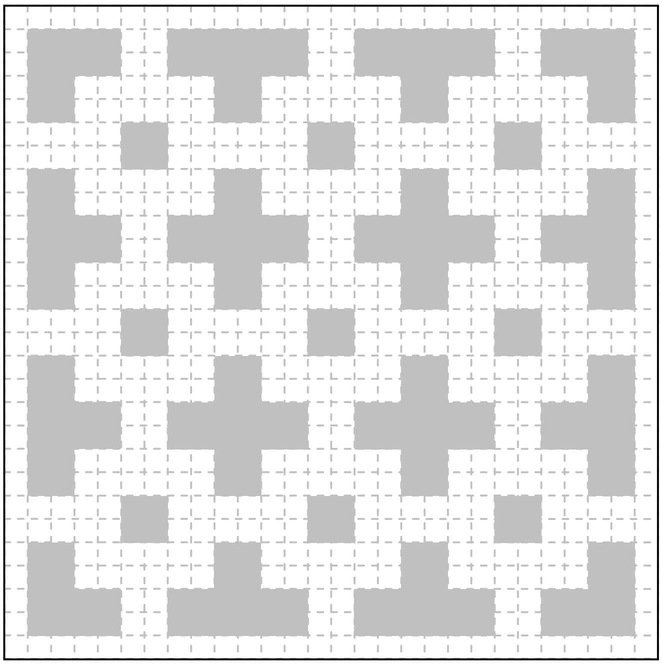

Figure 4.44 – Cross Design 3

Table 4.15 – Design 3 optimal results

Cross 3					
nN_{Max}	A_{Tot}	P_{Tot}	nN	nS	nN_{Max}
Cross 3	200	956484	69192	196	18
	400	956484	88752	400	12
	600	1000000	97196	484	11
	800	1000000	97196	484	11
	1000	1000000	97196	484	11

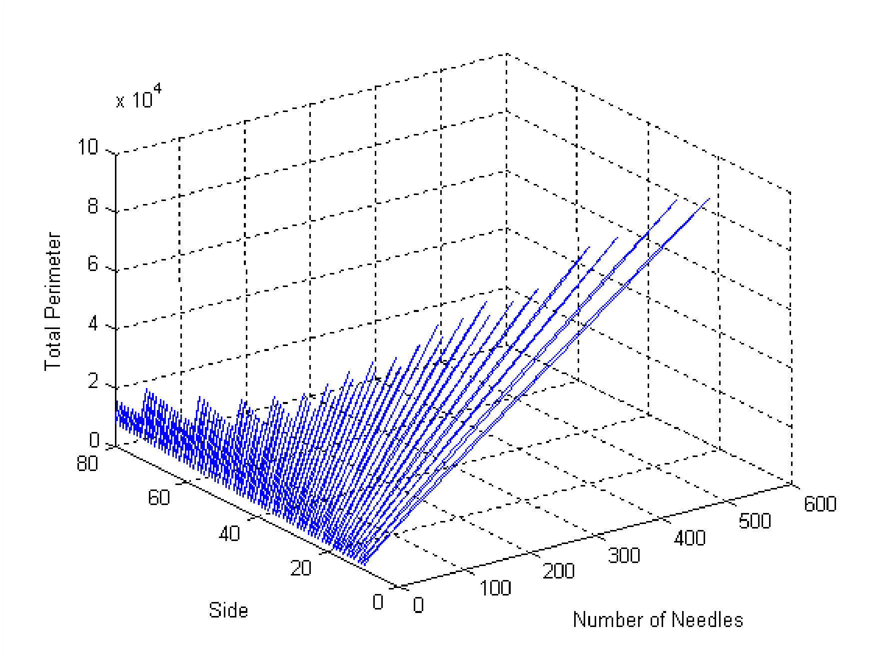

Figure 4.45 – Effect of needle dimensions and number of needles

4.5.13 Section summary

Different geometries were explored and analyzed in pursue of the optimal electrode parameters. The problem was formulated and modeled using two different optimization tools for verification purpose. The first analysis was executed on GAMS and repeated using a customized Matlab based optimizer crated for the electrode design optimization process.

The total perimeter was found to be a function of the product needle-count and needle-radius. As the electrode base area increases, it can accommodate more needles and consequently, the perimeter will expand.

Table 4.16 summarizes the maximum perimeter results for a range of maximum number of needles, minimum feature size and electrode base area. The cylindrical prisms are taken as a reference as it offers the smallest perimeter and in the same time it has the simplest geometry.

Table 4.16 – Summary of geometrical optimization results

Geometry	nN_{Max}	Side/ Rin_{Min}	D_{Min}	W	A_{Tot}	P_{Tot}	nN	Side - Rin
Cross 3	200	10 - 5	10	1e3	956484	69192	196	18
Cross 3	400	10 - 5	10	1e3	956484	88752	400	12
Cross 3	600	10 - 5	10	1e3	1e6	97196	484	11
Cross 2	800	10 - 5	10	1e3	1e6	98040	625	10
Cross 1	1E3	10 - 5	10	1e3	999600	99960	833	10
Cross 3	200	1 - 3	3	1e3	931225	76880	196	20
Cross 3	600	1 - 3	3	1e3	974169	124848	576	12
Cross 3	1E3	1 - 3	3	1e3	938961	152100	961	9

In this section, the optimum geometrical solutions were identified for different electrode dimensions and base areas. The mechanical analysis will decide whether the optimal geometrical solution is valid, otherwise, it will be ruled out and the electrical performance will have to be compromised for mechanical strength which will be studied in sections 4.6, 4.7 and 4.8.

Part 4 – Mechanical requirements

4.6 Forces acting on the electrode

4.6.1 Introduction

When an electrode penetrates through the skin, it experience different forces. The free body diagram of a needle in action is shown in figure 4.46. The three forces exerted on the needle are identified as:

1. Tip force
2. Friction force
3. Clamping force

The tip force is the reaction acting on the needle's tip in the axial direction, and during penetration; it is the cutting force and its value depends on the shape of the tip. The friction force is exerted on the side walls of the shaft in the axial direction and can be basically determined as the scalar product of the normal force acting on the surface and the coefficient of friction. Finally, the clamping force is the force that acts on the side walls of the needle's shaft but in the normal direction. The clamping force is exerted by the compressed tissue on the needle's walls and as the needle penetrates deeper, the contact area increases and the force increases accordingly.

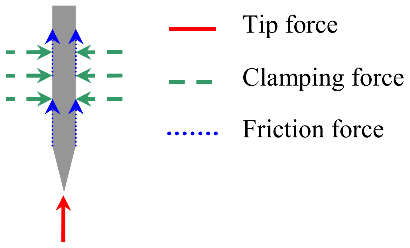

Figure 4.46 – Forces acting on the needle

4.6.2 Insertion force

The needle insertion force should overcome the total axial force acting on the needle which is the sum of the tip and the friction forces. Experimental data was analyzed from previous research dealing with needles and micro-needles [95] [96] [97], the values are listed in table 4.17. Using interpolation of experimental results [95] [96] [97], the insertion force is estimated to be 0.010 N per needle in the array.

Table 4.17 – Experimental values for needle insertion force

Number of needles	Radius/Side	Length	Insertion force
1	10 µm	500 µm	0.078 N
400	80 µm	180 µm	10 N (0.025N/needle)
1	710 µm	12.7 mm	1 N

4.7 Analytical buckling analysis

4.7.1 Introduction

During insertion, the micro-electrode can undergo mechanical failure through two modes, buckling and fracture [98]. When the electrode penetrates the skin, the maximum principal stress on the needles is axial. Studying the forces and reactions exerted on the needles during skin penetration is required to evaluate the critical loads which will cause mechanical failure and the needles' minimum dimensions which will offer the required mechanical strength.

The stresses and buckling loads are evaluated using classical analytical approaches [99]. Also, finite element analysis is used to model and anlayse the electrode using Ansys.

4.7.2 Buckling analysis

When an axial load is applied to a long and slender column such that the force equilibrium is disturbed and diverges into an instable state, buckling will occur which is bending of the column in a pattern that will prevent the needle form penetrating into the skin and will eventually lead to mechanical failure and fracture. Buckling occurs when the applied force exceeds the critical load which induces equilibrium instability. The value of the critical load is a function of the support and load configurations for the specific structure. If the critical buckling load is less than the axial force of insertion, the needles will buckle and break.

The most critical time is just before penetrating the skin where the axial load and the effective length are at their maximum values [100]. Buckling occurs with large loads, where a small disturbance would cause a column to bend sideways with an indefinitely large displacement. Moreover, buckling encourages further buckling, thus it is progressive and catastrophic. An eccentric load will cause a decrease in strength, since there will be a bending moment and a curvature from the start.

Long structures are more elastic than shorter ones and tend to bend when an axial load *P* is applied and will be subjected to buckling. While in the case of shorter structures; compression failure is more dominant. Rankine's formula [101] combined these results empirically to give a maximum load P_{Cr_Max} by the formula:

$$\frac{1}{P_{Cr\_Max}} = \frac{1}{P_{Cr\_Buckling}} + \frac{1}{P_{Cr\_Compression}} \tag{4.44}$$

The critical load using this formula will be less than either $P_{Cr\_Buckling}$ or $P_{Cr\_Compression}$

Critical load and Euler's formula

The analytical approach to evaluate the critical load for elastic members starts with Euler's simple non-conservative general equation 4.45 [102]:

$$E.I_x.\upsilon''+P.\upsilon \tag{4.45}$$

where,

E: Young's modulus

I_x: second moment of inertia

υ'': second derivative of lateral deflection

P: axial load

υ: lateral deflection

Buckling occurs when equation 4.46 has singularities, and these singularities take place when P is a multiple of the critical buckling load P_{CR}. Euler's equation expresses the critical load as follows:

$$P_{Cr}=\frac{\pi.E.I_x}{L^2} \tag{4.46}$$

where,

P_{CR}: critical buckling load

L: length

If there is an eccentric load or inelastic condition involved, buckling occurs at a lower axial load or in a non-specific pattern and the length has to be corrected and replaced by the effective length. Thus, Euler's formulae will be:

$$P_{Cr}=\frac{\pi.E.I_x}{L_{eff}^2} \tag{4.47}$$

where,

L_{eff}: distance between zero moment points (figure 4.47) and its value can be determined from table 4.18

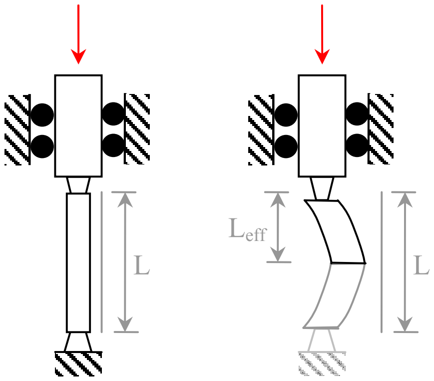

Figure 4.47 – Evaluating column's effective length

Table 4.18 – Boundary conditions and effective length values

Boundary Conditions	Theoretical Effective Length	Engineering Effective Length	Buckling Mode Shape
Fixed -Free	2.L	(1.2).L	$1\text{-Cos}\left(\pi.x/2.L\right)$
Fixed -Pinned	(0.699).L	(0.734).L	$1\text{-Cos}\left(\pi.x/L\right)$
Fixed- Fixed	(0.5).L	(0.65).L	$1\text{-Cos}\left(2.\pi.x/L\right)$
In practice, the Effective Length Constant is increased by a approximately 10 - 20 %			

As Euler's load is inversely proportional to the square of the needle length; then it is suitable only for long columns where the slenderness ratio > critical slenderness ratio. Thus for short needles, the critical load calculated using Euler's formula can exceed the compressive yield load of the material. Therefore, buckling will occur at lower loads and the results have to be corrected by J. B. Johnson's formula.

Slenderness ratio

The slenderness ratio is the effective length of the column divided by its radius of gyration and it classifies the compression members into short, intermediate and long. It is represented by:

$$S=\frac{L_e}{r_G} \qquad (4.48)$$

(5)

Short Column: 0 < S < 60
Intermediate Column: 60 < S < 120
Long Column: 120 < S < 300

$$r_G = \sqrt{\frac{I_x}{A}} \tag{4.49}$$

S: slenderness ratio

r: radius of gyration which is the distance from an axis which, if the entire cross sectional area of the object (beam) were located at that distance, it would result in the same moment of inertia that the object (beam) possesses.

A: cross-section area

I: moment of inertia

The critical slenderness ratio is given by:

$$S_{Cr} = \sqrt{\frac{2.\pi^2.E}{\sigma_y}} \tag{4.50}$$

Compressive yield stress:

$$\sigma_y = \frac{2.\pi^2.E}{S_{Cr}^2} = 2.\sigma_{Cr} \tag{4.51}$$

If the slenderness ratio > critical slenderness ratio, then the needle is treated as a long column and the Euler buckling formula is applicable. On the other hand, if slenderness ratio < critical slenderness ratio, then the needle is treated as a short column and Johnson's formula is used.

Johnson's formula

As the critical buckling load is inversely proportional to the square of the needle's length, thus the critical load will increase remarkably for short needles and it can exceed the compressive yield load. Johnson's formula is best suited for short and thick columns as it relates both the material yield stress and the critical load calculated using Euler's formula, thus it considers the compressive forces acting on the column as well as buckling forces. Defining the maximum load for failure by compression, the critical buckling load can be calculated as:

$$P_{Cr\_Compression} = A.\sigma_y \tag{4.52}$$

where,

σ_y : compressive yield stress

A: area

If the compression is more dominant than buckling, Johnson's formula is used to evaluate the critical load [103]:

$$P_{Cr}=\sigma_y.A\left[1-\left(\frac{S^2}{4.\pi^2.E}\right).\sigma_y\right] \tag{4.53}$$

σ_y : compressive yield stress

S: slenderness ratio

A: cross-section area

L_e: distance between zero moment points

In the case of inelastic behavior, the constant of proportionality E_t (tangent modulus) is used to replace the modulus of elasticity E. E_t is the slope of the stress-strain diagram beyond the proportional limit. Where within the linearly elastic range, $E = E_t$.

4.7.3 Support (Boundary) conditions

When the needle penetrates the skin, the support conditions can be classified as fixed-fixed or fixed-pinned. The needle’s upper end is fixed to the electrode base while its lower tip is piercing through the skin. Due to the friction between the needle tip and the skin, the supporting condition can be considered either rotating or fixed depending on the friction. The boundary conditions coefficients are illustrated in figure 4.48.

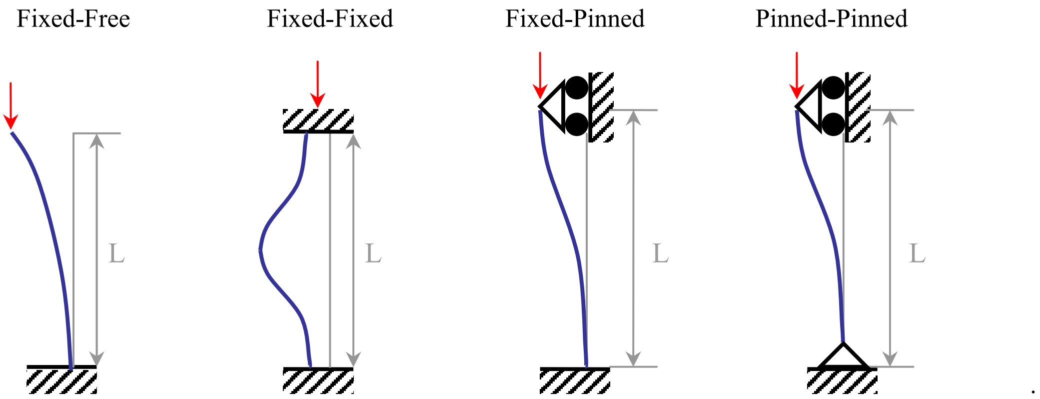

Figure 4.48 – Buckling tip conditions

Penetration forces

The normal force is estimated to be 1N, which is about the force needed to push an elevator button. This is 10 times more than the insertion force for each needle in the electrode (section 4.6), and this will be taken as a worse case scenario design criteria to evaluate safe dimensions for the electrode needles.

4.7.4 Material properties

The mechanical analysis is carried for different materials, silver and gold for being inert and readily biocompatible, then silicon and SU-8 as substrates to be coated with a metal layer afterwards. The physical properties of these materials are listed in table 4.19 [104] [105] [106] [107].

Table 4.19 – Physical properties of candidate materials

Material	Electrical resistivity [$10^{-8}\Omega$/m]	Modulus of elasticity [GPa]	Poisson ratio	Shear modulus [GPa]	Density [g/cm^3]	Yield stress [MPa]	Ultimate stress [MPa]	Electrode potential [V]
Silver	1.6	83	0.37	30	10.5	54	170	+0.799
Gold	2.2	72	0.44	27	19.3	54	108	+1.5
Silicon	100000	47	-	-	2.33	-	-	N/A
SU8	-	4.02	0.22	0.009	-	19	34	N/A

4.7.5 Structural properties

The moments of inertia for different needle geometries are presented here and will be used in structural analysis to evaluate the critical loading conditions:

Circular needles:

$$I_x = \frac{\pi . R^4}{4} \tag{4.54}$$

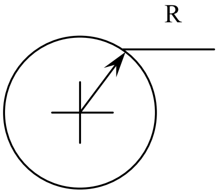

Equilateral triangular needles:

$$I_x = \frac{a.h^3}{36} = \left(\frac{\sqrt{3}}{2}.a\right)^2.\frac{a}{36} = \frac{\sqrt{3}}{96}.a^4 \qquad (4.55)$$

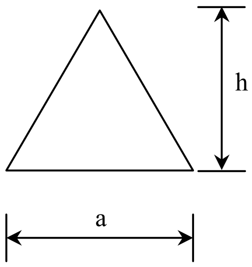

Hollow equilateral triangular needles:

$$I_x = I_{x\text{-Outer}} - I_{x\text{-Inner}} \qquad (4.56)$$

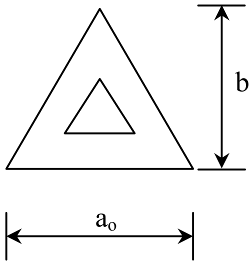

Cross needles:

$$I_x = \frac{29}{12}.a^4 \qquad (4.57)$$

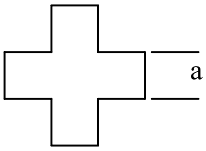

Square needles:

$$I_x = \frac{a^4}{12} \qquad (4.58)$$

4.7.6 Critical load analysis

Four electrode layouts are chosen from the output of the geometrical optimization process for analysis. Critical loads are calculated and compared for different needle dimensions and electrode parameters.

Analytical analysis

The analytical approach to evaluate the critical buckling load is illustrated as a flow chart in figure 4.49.

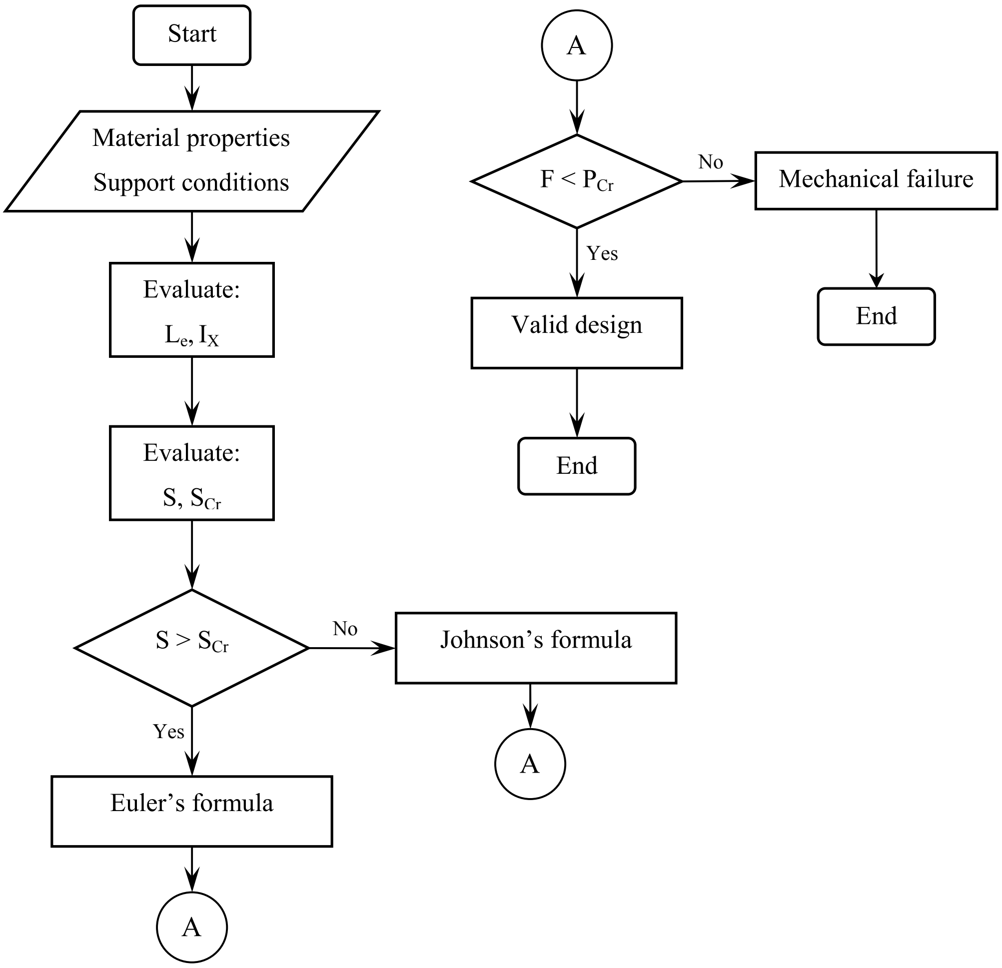

Figure 4.49 – Flowchart for critical buckling load estimation

4.7.7 Evaluating minimum dimensions

Buckling analysis is used to calculate the minimum dimensions for different cross-sections that can handle the exerted forces without failure. The outcome of these calculations is applied in the optimizer as mechanical constraints to define the lower boundaries for the needles' dimensions. Fixed-free loading condition is considered the worst case and thus suffices evaluating the minimum needle dimensions. Detailed steps for silver needles are presented in appendix D.

4.7.8 Results

The slenderness ratio calculated for the different needles is less than the critical slenderness ratio thus the needles are treated as axially loaded short and thick columns. Using Euler's formula, the critical load calculated exceeds the compressive yield stress of the material and consequently, buckling will occur at lower loads. Thus; J. B. Johnson's formula is used to correct the results. The minimum dimensions for silver electrodes are demonstrated in table 4.20.

Table 4.20 – Minimum dimensions for Silver needles

Geometry	Fixed – Free	
	Euler	Johnson
Circle	14.4723	76.7886
Solid triangle	37.1739	207
Cross	10.9271	60.866
Square	25.3574	136.103

Table 4.21 – Minimum dimensions for Gold needles

Geometry	Fixed – Free	
	Euler	Johnson
Circle	15	77
Solid triangle	38	207
Cross	11	61
Square	25.75	137

Table 4.22 – Minimum dimensions for Silicon needles

Geometry	Fixed – Free
	Euler
Circle	16.68
Solid triangle	43
Cross	13
Square	29

Table 4.23 – Minimum dimensions for SU-8 needles

Geometry	Fixed – Free	
	Euler	Johnson
Circle	31	130
Solid triangle	79	349
Cross	23	103
Square	54	230

4.8 Shear and stress analysis

4.8.1 Introduction

Stress is the internal force exerted by one part of an elastic body upon the adjoining part, and strain is the deformation or change in dimension occasioned by stress. When the needles of the electrode penetrate the skin, they will experience forces dominated by axial stresses. These axial stresses will cause mechanical failure if the structure geometry and material properties can not handle the resultant stresses. Hence, stress analysis is required to evaluate the mechanical performance of the electrode.

4.8.2 Definitions

Stress is the internal distribution of forces within a body that balance and react to the loads applied. A normal stress is the stress at a point that is oriented perpendicular to the planes on which it acts. Shear stress is a stress state in which the shape of a material tends to change by sliding forces. Permanent deformation is attained at yield stress [108]. Metal deformation is proportional to the imposed loads over a range of loads. Since stress is proportional to load and strain is proportional to deformation, this implies that stress is proportional to strain. Hooke's Law is the statement of that proportionality. The constant, E, is the modulus of elasticity, Young's modulus or the tensile modulus and is the material's stiffness. If a material obeys Hooke's Law it is elastic.

Ultimate strength

Yield strength is the point at which material exceeds the elastic limit and will not return to its origin shape or length if the stress is removed. This value is determined by evaluating a stress-strain diagram produced during a tensile test.

Poisson's ratio

The ratio of the lateral to longitudinal strain is Poisson's ratio

4.8.3 Normal stresses

If the compressive stress acting on the electrode is greater than its compressive yield stress σ_y, then the needles will be damaged and the electrode will fail mechanically. Accordingly, the purpose of this analysis is to determine the minimum dimensions of the needles that will be able to handle the applied forces.

The stress is calculated for each needle in the electrode as follows:

$$\sigma = -\frac{F}{A} \pm \frac{M_x}{I_x}.y < \sigma_y \tag{4.59}$$

(4.60)

where,

F: normal force acting on the needle

A: cross-section area

P_{Hz}: horizontal force

L: length of the needle

I_X: moment of inertia

y: distance between the centroid and the maximum shear point

Because the compressive yield stress of silver is less than its tensile yield stress, the maximum compressive stress will be only considered:

Maximum compressive stress:

$$\sigma_{\text{Compressive}} = -\frac{F}{A} - \frac{M_X}{I_X}.y < \sigma_{y-\text{Compressive}} \tag{4.61}$$

Again, the normal force used in the analyses is 0.1 N which is 10 multiples of the actual insertion force required for each needle in the electrode. Compressive stress will be calculated for a range of P_{Hz} values starting with 40 N which is equivalent to applying 4 Kg.f per electrode. This is the force that acts on the electrode in case if being pulled accidentally while attached to the scalp. In case of 400 needles per electrode, P_{Hz} is 0.1 N per needle. Detailed analysis is presented in appendix E.

4.8.4 Results

Buckling analysis imposed more strict conditions on the minimum dimensions than the shear analysis. Shear analysis results for applying 0.1N per spike are summarized in table 4.24. Detailed analysis and results are presented in appendix E.

Table 4.24 – Shear analysis results

Geometry	Safety factor	
	1	1.5
Circle	50 µm	58 µm
Triangle	176 µm	203 µm
Cross	48 µm	55 µm
Square	126 µm	145 µm

4.8.5 Discussion

Silver exhibits dominant mechanical performance among other candidate materials but it is almost identical to gold provided that the noble metals used are ordinary without special physical treatment which can improve the mechanical performance with added cost. Silver will be used for the electrode because it is more economic than gold. Feeding the values in table 4.20 (which resemble the minimum dimensions for silver spikes with different geometries) back into the optimizer; the optimal geometry can be identified for two bases areas using 1000µ and 3000µ base side lengths with an industrial constraint of 30µ as the minimum feature and minimum spike spacing. And it can be seen that Cross-1 architecture yields the highest value for the total perimeter and will used for the electrode layout fulfilling the design guideline and specification for mechanical structure requirements and maximizing the contact area.

Table 4.25 – Optimal geometrical dimensions of silver electrodes fulfilling mechanical requirements

1000µm x 1000µm base area				
Geometry	Number of needles	Radius/Side	Perimeter	Area consumption
Circle	37	77	17900.8	98.38%
Triangle	34	207	21094.3	98.58%
Cross-1	32	60.8	23347.2	97.05%
Square	36	136	19584	99.20%
3000µm x 3000µm base area				
Circle	338	77	163526	99.86%
Triangle	310	207	192330	99.87%
Cross-1	296	60.8	215962	99.74%
Square	326	136	177344	99.81%

4.9 Finite element analysis

4.9.1 Introduction

The complete mechanical analysis requires identifying the support and boundary conditions and exploring the effects of friction between skin and the tip of a needle. Therefore, a finite element electrode model is created and simulated using ANSYS which includes friction analysis. The analysis simulated the needle poking and penetration though skin as well as the forces affecting an array of needles. Using the results of skin stress distribution and deformed shape, penetration was verified. Furthermore, Engrasp ETBX column buckling tool was used for verifying the analytical approach for buckling analysis.

4.9.2 Simple compression and buckling

The first phase in the finite element analysis studied the compression of a single needle without regarding the interaction with skin. The outcome of this analysis is compared to the analytical results to verify the finite element method and model.

4.9.3 Modeling and meshing

Referring to the geometric optimization and analytical buckling analysis in sections 4.5 and 4.7, the optimal geometry was determined to be a cross with a side length of 62µm. This was modeled and analyzed. The 3D models are meshed using Solid-95 elements with mesh size of 3µm. This is the minimum element size allowed by the ANSYS license which limits the elements to 128000. The meshed model is shown in figure 4.50.

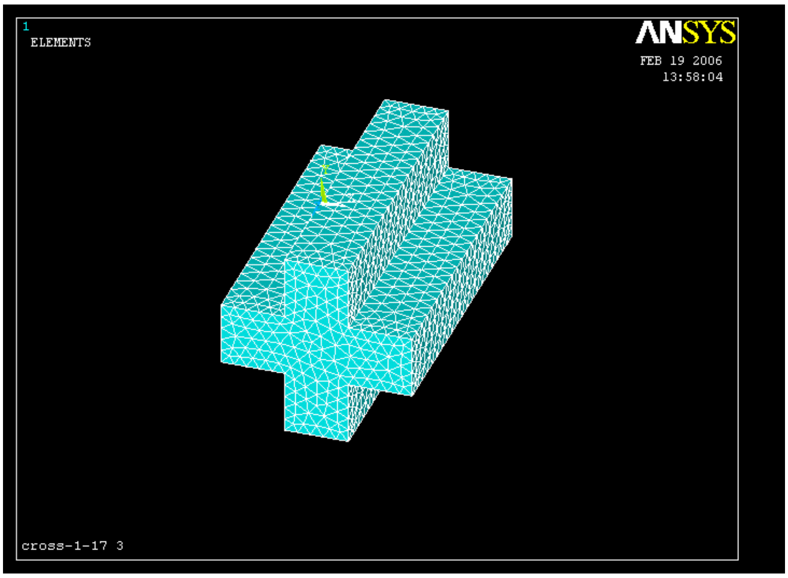

Figure 4.50 – Meshed cross needle

The Solid95 element type is defined by 20 nodes and is suitable for structural solid elements. It has three degrees of freedom per node defining translations in the nodal x, y, and z directions. This element may have any spatial orientation and allows tetrahedral, pyramidal and prism shapes. Solid95 (figure 4.51) has plasticity, creep, stress stiffening, large deflection, and large strain capabilities [109].

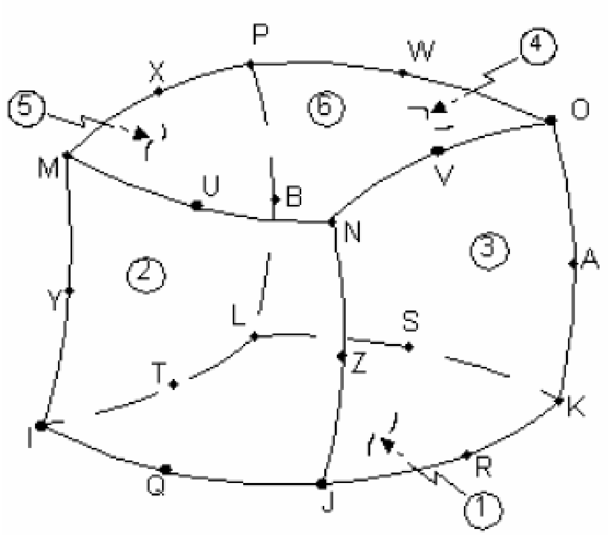

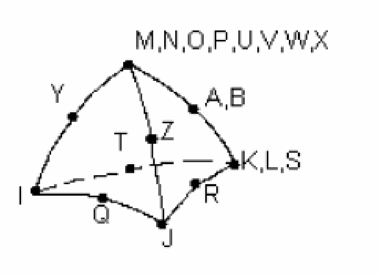

(Tetrahedral Option)

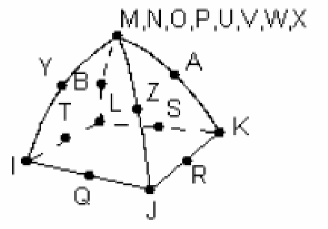

(Pyramid Option)

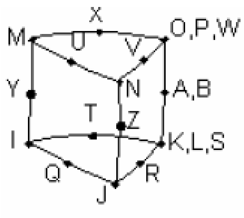

(Prism Option)

Figure 4.51 – Finite element Solid-95

4.9.4 Needles support, loading and boundary conditions

Three different supporting conditions were simulated in this phase. The boundary conditions for these configurations are as follows:

The fixed-free configuration is the simplest and represents the worst case scenario where buckling can occur at lower values compared to other configurations. The boundary and load conditions are as follows:

- The top surface of the needle is perfectly fixed and all its degrees of freedom are restricted.

- The lower end of the needle is completely free to move in all directions.
- Load is applied at the lower tip area in the form of pressure equivalent to 1N:

$$\text{Pressure}=\frac{1}{A} \tag{4.78}$$

Boundary and load condition for fixed-fixed configuration:

- The top surface of the needle is perfectly fixed and all degrees of freedom are restricted.
- The lower end of the needle is restricted to move in the Z direction.
- Load is applied at the lower tip area in the form of displacement equivalent to 1N.

$$\text{Displacement}=\frac{L}{A.E}=5.014\text{x}10^{-8}\text{m} \tag{4.79}$$

where:

L: length of needle

A: area of needle

E: modulus of elasticity = stress/strain

Boundary and load condition for fixed-pinned configuration:

- The top surface of the needle is perfectly fixed and all degrees of freedom are restricted.
- The lower end of the needle is restricted to move in the Z direction or symmetrically about the center of the upper surface to allow a rotational degree of freedom.
- Load is applied at the lower tip area in the form of pressure equivalent to 1N.

The reason for loading with a 1 N load ix explained in the following section.

4.9.5 Results

The critical buckling loads using Engrasp ETBX with different loading conditions are consistent with the classical analytical approach. The results are listed in table 4.26:

Table 4.26 – Critical buckling loads

62µ Cross		
Support	P_{CR} analytical	Engrasp ETBX
Fixed-Free	1.15N	1.456139N
Fixed-Pinned	1.49249N	1.4929N
Fixed-Fixed	1.49214N	1.495524N

4.9.6 Buckling analysis in ANSYS

There are two different methods to run a buckling analysis using ANSYS. The Eigen buckling based on Euler's formula is systematic but is preceded by several processes to obtain data required for developing the buckling solution. After a model is created, meshed and loaded, simple compression analysis is performed to produce the stiffness matrix. Then Lanczos' algorithm is used to expand the stiffness matrix to find its singularities which represent the modes of buckling. Finally, the output of this step is the mode shape and the critical load expressed as a factor of an initial load which is taken to be unity (1N). Results of Eigen buckling analysis were not consistent with the analytical approach and the explanation was because Eigen buckling analysis does not include Johnson's correction formula for short beams. Thus, non-linear structure analysis was used.

The loaded model in figure 4.52 shows the pressure applied to the top surface of the needle with a value of 53MPa corresponding to a force of 1N. The deformed shape and the Z direction displacement in figure 4.53 and 4.54 respectively show the maximum deformation of 8.7µm. Finally, the von misses stress diagram in figure 4.55 estimates the stresses to have a value of 56MPa with a maximum value of 92MPa concentrated at the corners.

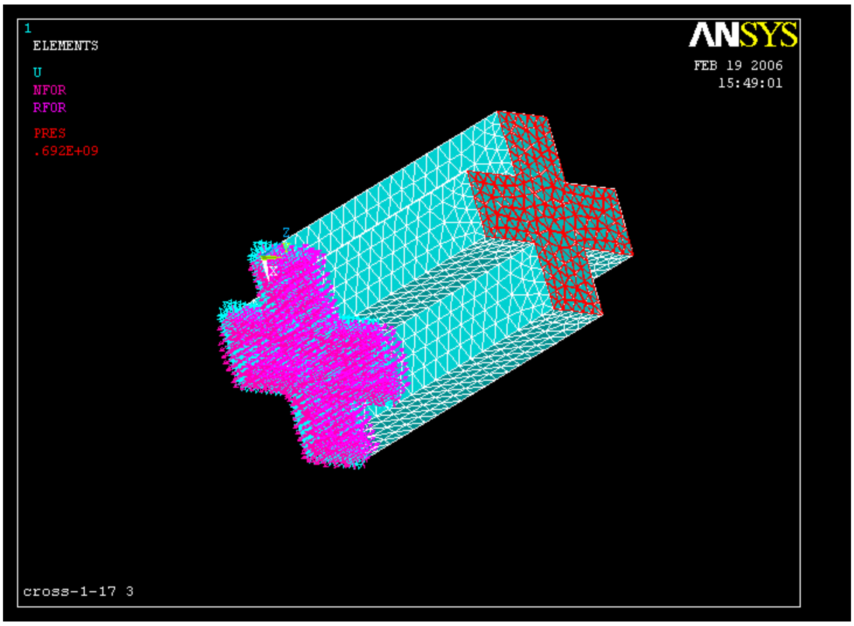

Figure 4.52 – Loaded model

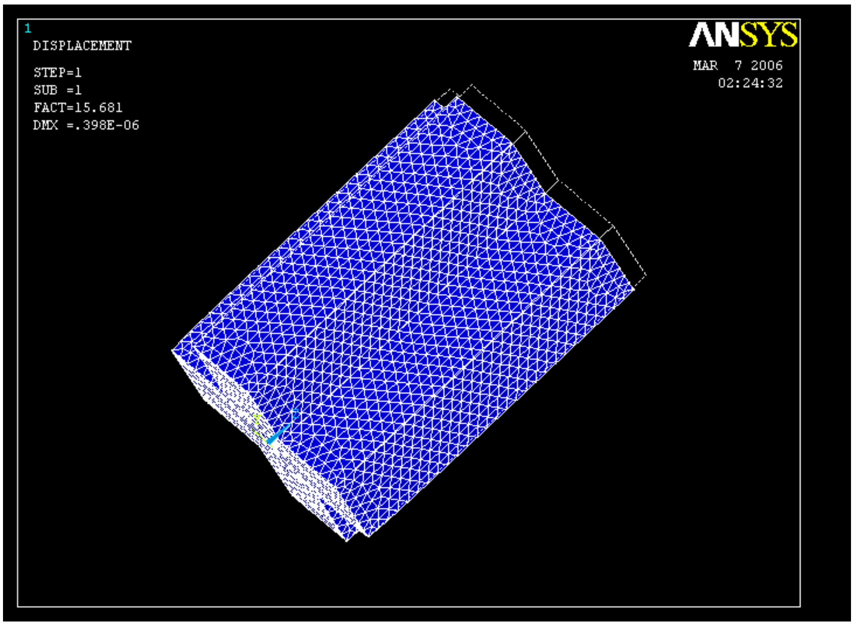

Figure 4.53 – Deformed shape of cross needle

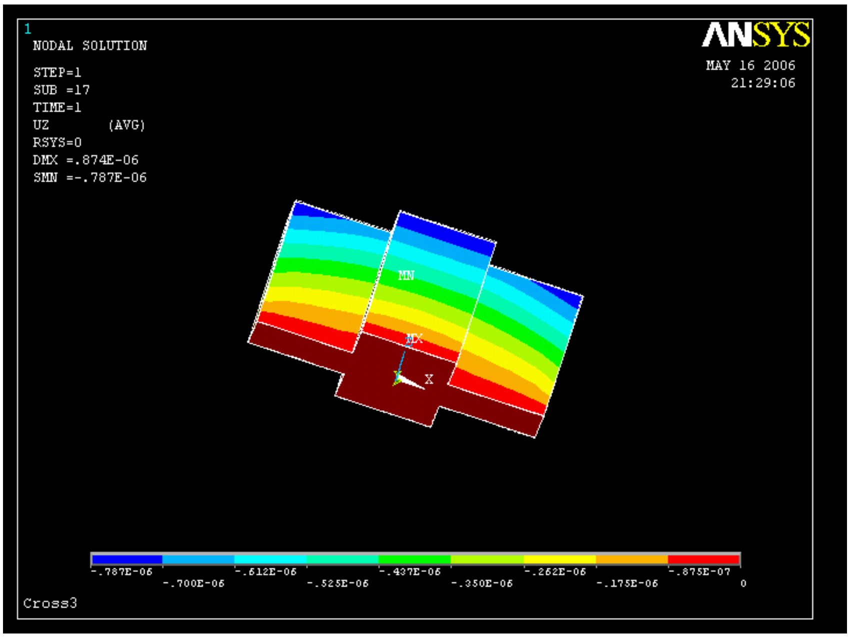

Figure 4.54 – Z direction displacement

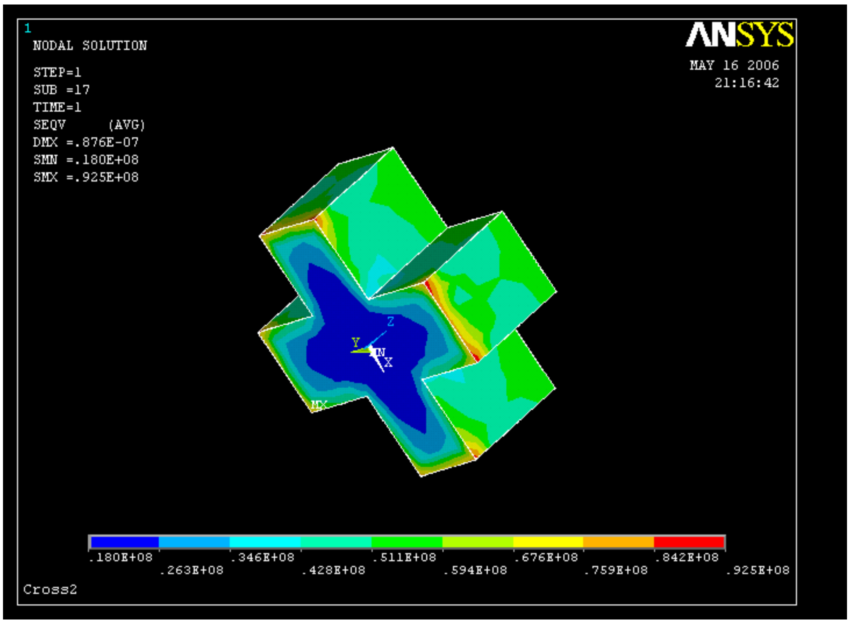

Figure 4.55 – Von misses stresses

4.9.7 Effect of friction

In order to determine the appropriate loading condition, friction between the needle and a steel disc is analyzed. Pressing the needle against a rigid surface will not deform the surface and this will reveal the effects of friction on the contact surface. The coefficient of friction was estimated to be 0.26 which was derived from a steel-nylon interface [110]. Finally the results are compared with the buckling analysis results of a single needle with different loading states to conclude the best match.

The contact interface was identified and configured using ANSYS contact wizard. To make use of the symmetry, one quarter of the system was modeled and symmetric boundary conditions were applied. The needle-disc model is shown in figure 4.56, the bottom surface of the disc is constrained from displacement in all directions and pressure is applied to the top surface of the needle which is allowed displacement only in the Z direction. The mesh size used is 5µm and the mesh was refined at the contact surface.

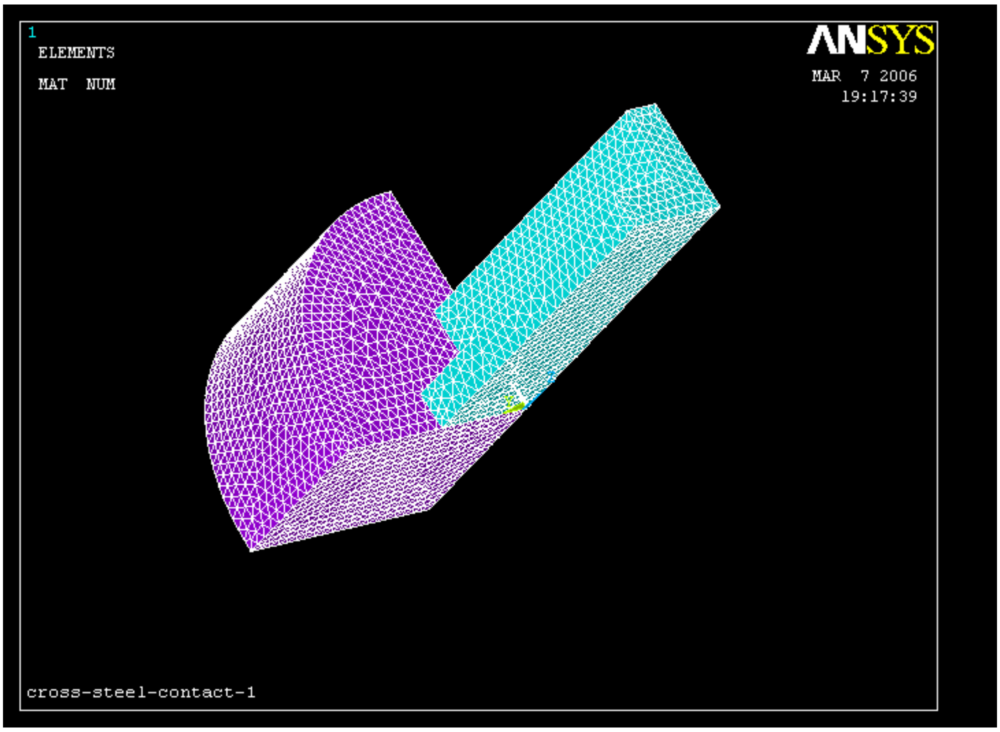

Figure 4.56 – Meshed model for quarter of a needle in contact with stratum corneum

4.9.8 Results

The results are very close to the fixed-fixed supporting condition which will be considered the case for the skin penetration analysis.

4.9.9 Skin penetration simulation

A model for the human skin was created for simulating needle penetration and showing the skin deformation. The outcome of this simulation evaluates the ultimate elongation of skin, which will determine whether penetration has occurred.

4.9.10 Skin model

The human skin is complex organ made up of multiple distinct layers that vary in structure and function. Mechanically, it exhibits non-homogeneous, anisotropic, non-linear and visco-elastic characteristics. Studying the skin properties in vivo is difficult, thus the useful data is mostly in vitro. Hendricks [110] provided data representing the mechanical properties of the different layers of the human skin which can be used to create a skin model. The mechanical properties of human skin vary between different persons even of the same gender and age. Using data from Hendricks [110] and Oomens [111] [112], a skin mechanical model was created and the mechanical properties for the integument layers are listed in table 4.27. The stratum corneum represents the challenging barrier having the highest modulus of elasticity. Simulating skin penetration and skin mechanical response based on the skin physical properties was performed using FEM skin model and single spike, the contact surface element is presented in figure 4.57.

Table 4.27 – Mechanical properties of skin layers

Layer	Thickness [µm]	Young's modulus [MPa]
Stratum corneum	20	12000
Viable epidermis	130	16
Dermis	1100	12

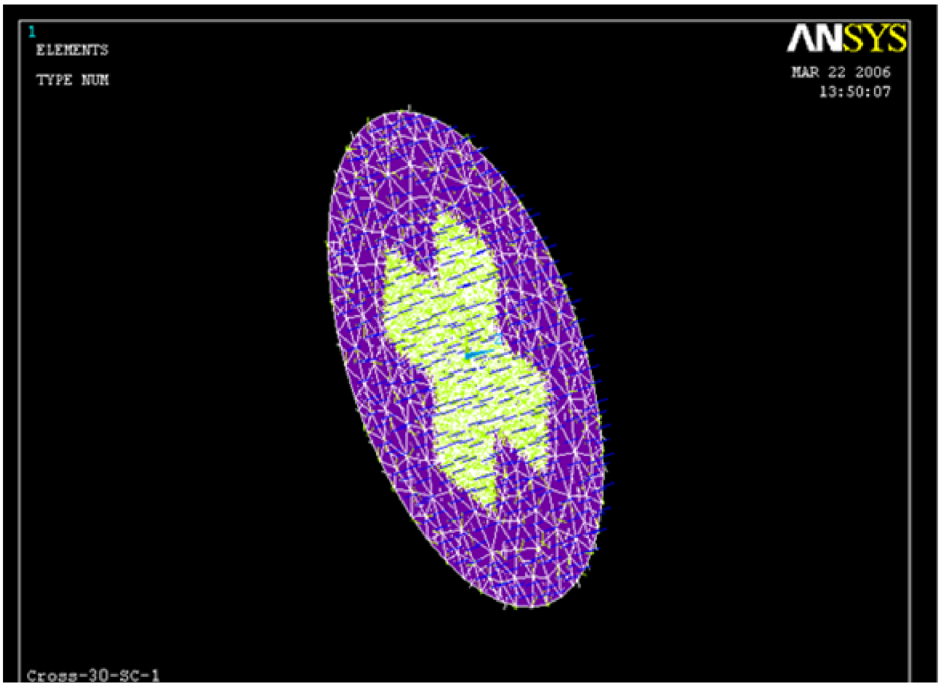

Figure 4.57 – Skin-electrode contact surface

Applying the appropriate boundary conditions and a displacement load on the poking spike, skin penetration was simulated. The resulting skin strain contour and deformed shape in figures 458 through 4.63 determined that skin was successfully penetrated. The analysis of the skin poking model gives the contour of strain. By knowing maximum elongation of skin, the penetration force can be obtained.

4.9.11 Discussion and results

In this section, the mechanical structure of the geometrical architecture proposed by section according to the design constraints was analyzed for mechanical failure. The aim of this analysis is to evaluate the smallest dimensions that provide the required mechanical strength represented by the design specifications in the form of maximum loading forces. This involved a buckling analysis and shear stress analysis. Analytical methods are used and a finite element model was created to study the interaction between the needle and skin. At this point, the design procedure is completed and the next chapter analyzes the electrode-skin interface to build the electrode circuit model.

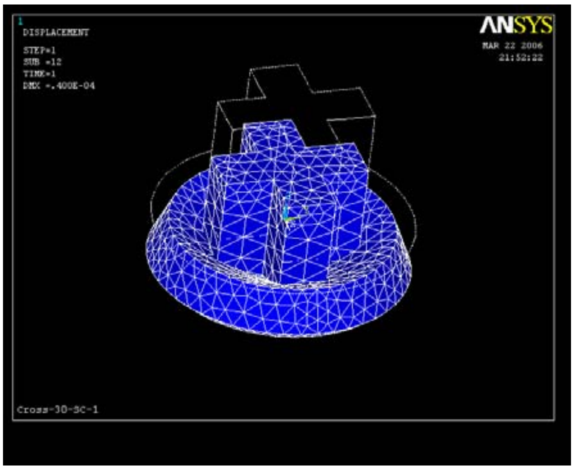

Figure 4.58 – Skin deformation, view 1

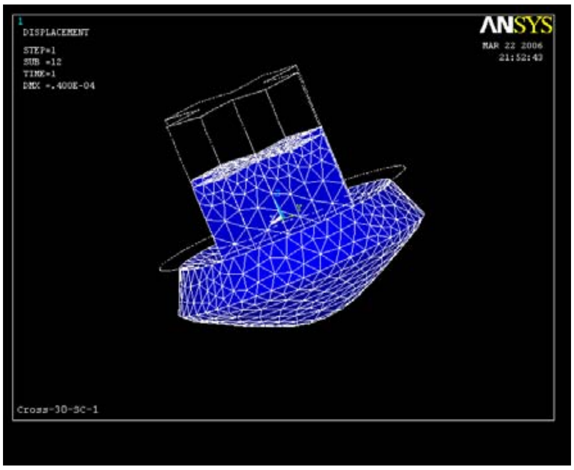

Figure 4.59 – Skin deformation, view 2

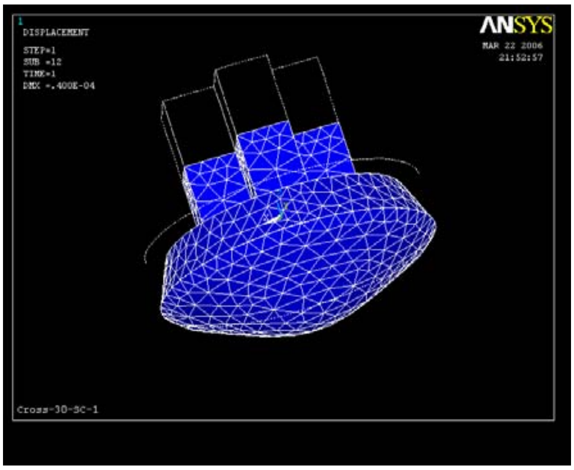

Figure 4.60 – Skin deformation, view 3

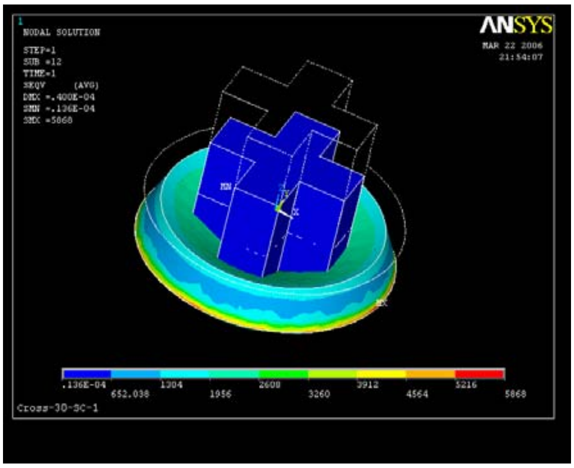

Figure 4.61 – Von misses stress, view 1

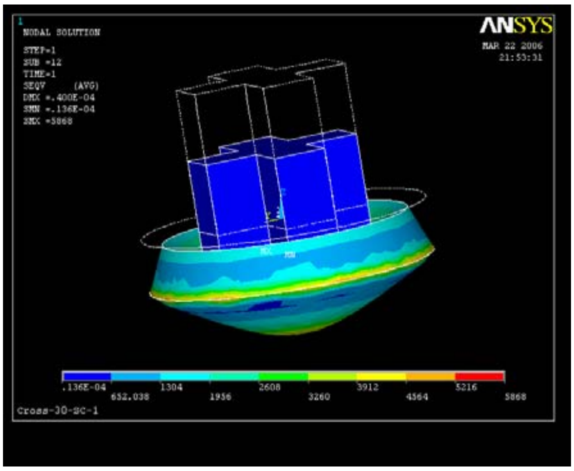

Figure 4.62 – Von misses stress, view 2

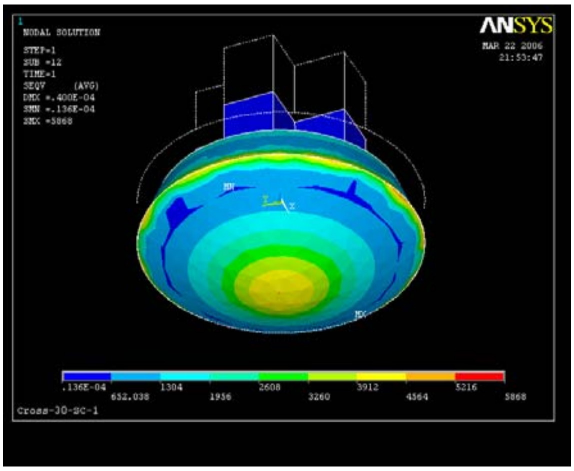

Figure 4.63 – Von misses stress, view 3

Conclusion

In this chapter, the different parameters influencing the electrode design are explored and the constraints constituting the design specifications were formulated as follows:

- Low electrode impedance < 5KΩ
- Maximum axial force per spike is 0.01N
- Maximum horizontal force per spike is 0.1N (4 Kg.f per electrode with 400 spikes)
- Good mechanical adhesion without gel
- Biocompatibility for prolonged recording > 6 hours, causing minimum tissue response
- Small number of channels and recording spots
- Fast and easy application and cleaning, neither gel nor skin preparation are allowed

- High immunity to electromagnetic interference

Chapter 5

Electrical Analysis

5.1 Skin-electrode interface

5.1.1 Introduction

In an electrochemical system, the characterization and modeling of the electrode-electrolyte interface is required for evaluating the equivalent circuit impedance. Which in turn is crucial for the amplifier design as the value and nature of the impedance will influence the amplifier circuit performance. If the potential-measuring device draws no current, then the potential between electrode terminals will be representative of the potential presented to the electrode. Thus the amplifier input impedance should be high enough to limit the drawn current.

This section outlines briefly the theory of the electrode application and the equivalent circuit representing the electrode-electrolyte interface is formulated.

5.1.2 Electrode application

When the electrode is immersed in the solution, metallic ions will be discharged from the metal into the solution, while some of the ions in the solution will start combining with the metallic electrodes. As this process goes on, the electrons on the metallic electrode will build up a negative charge which will create a barrier which prevents further ionization of metallic atoms into the electrolyte [113]. In the same time, positive charges in the electrolyte will emphasize this effect. Eventually, equilibrium state is reached and the charge gradient built up creates electrode potential (half-cell potential). A double layer which acts as a capacitor is formed due to the migration of ions whose ionic differences cause the electrode (V_e) [114].

When the metal electrode comes in contact with the skin, no signal can be detected unless current flows from the skin to the metal through the electrode-skin interface. With current flowing, the half-cell voltage changes causing electrode over-potential or polarization. Polarization is the result of direct current passing through the metal-electrolyte interface and this is a source of DC offset voltage. If two electrodes are made of different metals and are immersed in the same electrolytic solution, each electrode will exhibit its own half-cell potential (V_{ea} and V_{eb}) and a galvanic cell is created and its potential depends on the half cell electrodes, temperature, electrolyte concentration and the chemical reactions at the interfaces. A net potential difference (V_{ed}) is created forming the electrode DC offset which causes electronic current (I_e) to flow through both electrodes as well as through the input circuit of the amplifier to which they are connected. The resulting current is often mistaken for physiological events.

The half cell potentials can be written as [114]:

$$E_{\frac{1}{2}A} = E^{o}_{A^{n+}} - \frac{R.T}{n.F}.\ln A_{A^{n+}} \tag{5.1}$$

$$E_{\frac{1}{2}B} = E^{o}_{B^{n+}} - \frac{R.T}{n.F}.\ln A_{B^{n+}} \tag{5.2}$$

where,

E^{O}: electrode potential

R: gas constant

T: temperature

F: Faraday’s constant

n: valence

A: metal ion activity in the electrolyte

Thus to minimize the effect of DC offset voltage, similar metals will be used for the electrodes to pull the galvanic cell potential down to zero. But because the bioelectric electrodes are placed in different electrolytes, a slight residual potential will be created which is not stable and induces artifacts and generates DC offset at the inputs of the amplifiers. This requires DC suppression at the amplifiers inputs.

5.1.3 Electrode-electrolyte interface

Exchange of ions at the electrode-electrolyte interface results in a charge distribution at the electrode-electrolyte interface. A simple distribution was defined by Helmholtz in the form of a double layer, where a layer of ions are deposited on the surface of the electrode and a layer of opposite charged ions is formed in the electrolyte. The double layer creates a capacitive effect [115] and the thermal motion of ions forms a diffuse layer of ions and this was represented by Gouy’s arrangement.

5.1.4 Electrochemical impedance spectroscopy (EIS)

Electrochemical impedance spectroscopy (EIS) is required to fully describe the electrode-electrolyte interface electrical characteristics. Potentiostatic frequency scanning was used for impedance measurements utilizing frequency response analysis (FRA) where a series of AC waves with various frequencies are super imposed to a DC bias potential and applied to the electrochemical system. The resulting AC current is measured followed by plotting the real and imaginary impedance components on a Nyquist plot. Finally, analysis is used to match the model parameters which cause the best agreement between a model's impedance spectrum and the measured spectrum using chi-square technique.

Modeling the electrode-skin interface using EIS required creating an electrolyte which matches the ionic concentrations of the extra-cellular fluids. This electrolyte was used for the electrochemical impedance spectroscopy (EIS) experiment while silver rods were used as reference and active electrodes. According to the extra-cellular fluid composition in table 5.1, an electrolyte with ionic concentration close to that of the extra-cellular fluid was prepared using distilled water as a base medium and salts as sources of ions. The organic compounds including proteins and enzymes couldn't be added to the electrolyte and they will not add to the conductivity of the solution. Salt concentrations were converted from meq/L to grams according to the molecular weight of each of them as listed in table 5.2.

Table 5.1 – Concentration of electrolytes in body liquids

Cations (meq/L)			Anions (meq/L)		
	Extracellular	Intracellular		Extracellular	Intracellular
Na^+	142	10	Cl^-	103	4
K^+	4	140	HCO_3^-	24	10
Ca^{2+}	5	10^{-4}	protein-	16	36
Mg^{2+}	2	30	$HPO_4^{2-}+SO_4^{2-}+$ organic acids	10	130
H^+	$4x10^{-5}$	$4x10^{-5}$			
Sum	153	180	Sum	153	180

Sodium-chloride was used as a source for sodium and chloride ions. 142meq/L of soidium-chloride was required to get 142meq/L of Na^+ ions; in a 100mL electrolyte this is equivalent to $823.6x10^{-3}$ grams of sodium-chloride salt. For monovalent ions, 1 equivalent = 1 Mol, while 1 equivalent of divalent ions equals ½ Mol

NaCl:
(142 [milliMol/L]) x (0.1 [L]) x (1) x (22.98+35.45 [g/Mol]) = 829.706 milligrams

KCl:
(4 [milliMol/L]) x (0.1 [L]) x (1) x (39.098+35.45 [g/Mol]) = 29.8192 milligrams

$MgSO_4$:
(7 [milliMol/L]) x (0.1 [L]) x (1/2) x (24.3050+32.066+15.9994 [g/Mol]) = 25.329 milligrams

Table 5.2 – Molecular weights of extra-cellular fluid ions

	Molecular weight [g/Mol]
Sodium Na^+	22.9898
Chloride Cl^-	39.098
Potassium K^+	39.4527
Calcium Ca^{++}	40.078
Magnesium Mg^{++}	24.3050
Sulphur S^{++}	32.066
Oxygen O^{++}	15.9994

Table 5.3 – Ionic concentration of electrolyte and extra-cellular fluid

Ion	Average concentration in Extracellular fluid	Concentration in test electrolyte
Na^+	142	142
K^+	4	4
Ca^{++}	5	0
Mg^{++}	2	7
Cl^-	103	146
SO_4^{--}	10	7

Potentiostatic frequency scanning and circuit matching was done using Autolab frequency response analyzer and the experimental setup is shown in figures 5.1 through 5.3. The voltage signal used was 150mV scanning through a frequency range starting at 0.5Hz and increases in 1000 steps to reach a maximum value of 1 KHz. The measured impedance was plotted and the Nyquist plot is shown in figure 5.4.

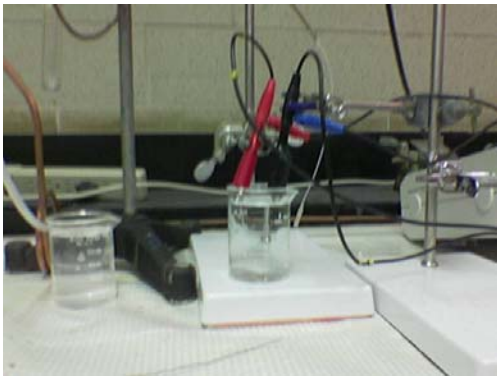

Figure 5.1 – Electrochemical cell used in EIS

Figure 5.2 – Electrochemical cell used in EIS

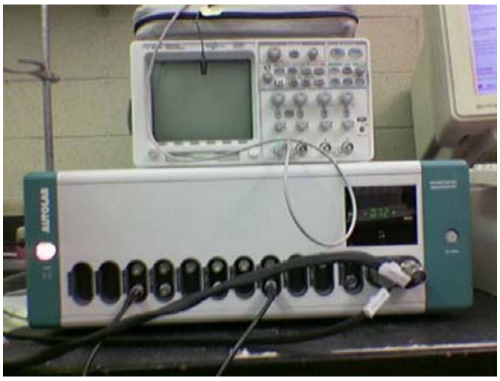

Figure 5.3 – Autolab FRA

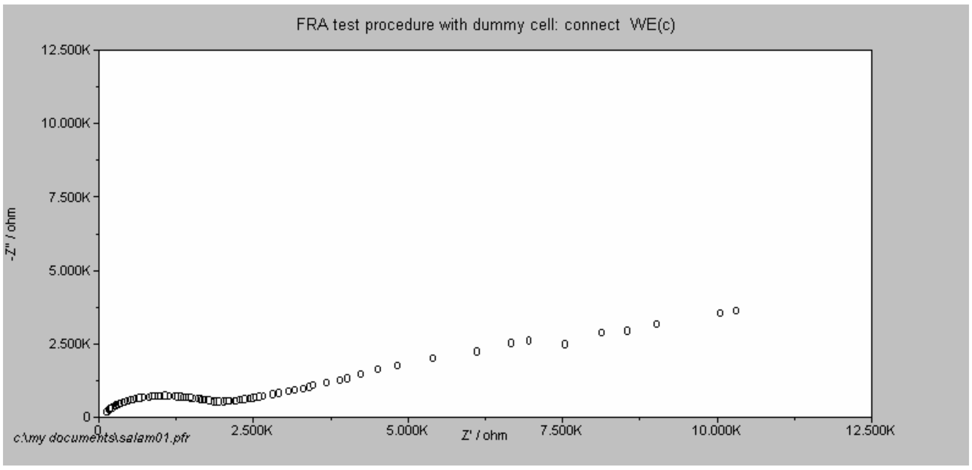

Figure 5.4 – EIS Nyquist plot for the skin-electrode interface

The sources of ionic currents and potentials in the human body are the electrochemical reactions which are influenced by the enzyme activity as well. These conditions can not be replicated in a lab experiment, and thus electric stimulation was used by superimposing 2VDC to the applied signal to initialize chemical reactions. This evolved to a water electrolysis setting, and consequently the nature of the electrode-interface was altered rendering the results to be approximate.

If the excitation signal can be expressed as a function of time given as:

$$E(t)=E_o.\cos(\omega.t) \tag{5.3}$$

then the current I_t can be expressed as:

$$I(t)=I_o.\cos(\omega.t-\Phi) \tag{5.4}$$

and the impedance of the system will be:

$$Z=\frac{E(t)}{I(t)}=\frac{E_o.\cos(\omega.t)}{I_o.\cos(\omega.t-\Phi)} \tag{5.5}$$

Using Eulers relationship,

$$e^{(j.\Phi)}=\cos(\Phi)+j.\sin(\Phi) \tag{5.6}$$

The impedance is then represented as a complex number,

$$Z=\frac{E}{I}=Z_o.e^{(j.\Phi)}=Z_o\left(\cos(\Phi)+j.\sin(\Phi)\right) \tag{5.7}$$

The impedance can be represented on Nyquist plot as in figure 5.5 which matches the response of the circuit shown in figure 5.6.

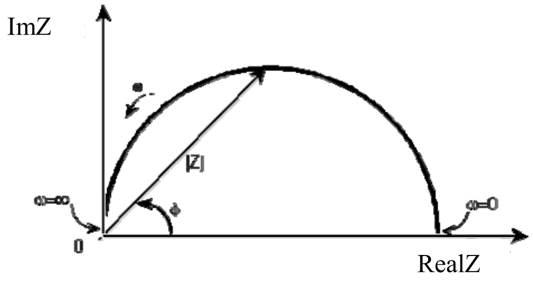

Figure 5.5 – Nyquist plot for a shunt RC circuit

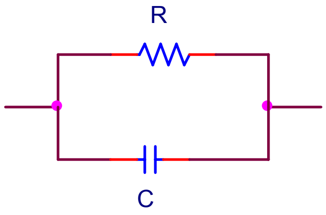

Figure 5.6 – Electrode-electrolyte interface model using a shunt RC circuit

Elements of the electrochemical equivalent circuit are illustrated in appendix F.

5.1.5 Skin-electrode interface model circuit

Different circuits were used to model the skin-electrode interface; the circuits and their curve fitting results are illustrated in the following section [116] [117].

Randles cell

The Randles cell is a simple cell which includes electrolyte resistance, a double layer capacitor and a charge transfer or polarization resistance as shown in figure 5.7. The result of curve fitting is shown in figure 5.8 and the component values and percentage error are listed in table 5.4.

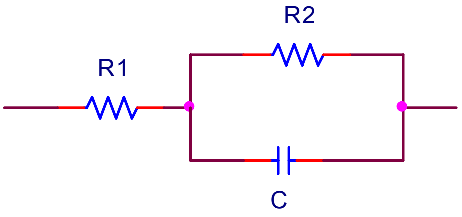

Figure 5.7 – Randles circuit model

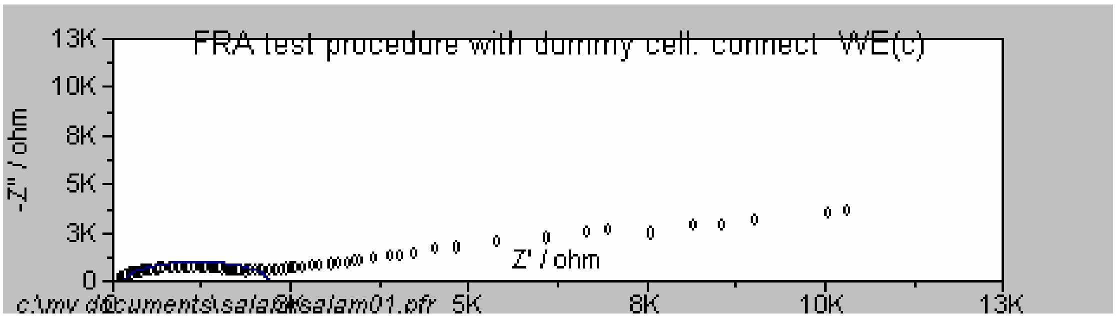

Figure 5.8 – Experimental vs. Randles circuit Nyquist plot

Table 5.4 – Randles circuit element values

Element	Value	Percentage error
R1	167.9	15.2 %
R2	2.027K	5.23 %
C	1.178u	7.119 %

Mixed kinetic and diffusion control

This circuit (figure 5.9 can represent the charge diffusion and the Nyquist plot (figure 5.10) is divided into two parts identified as the kinetic control and mass transfer control. The kinetic control is represented by the semicircle which plots the high frequency measurements corresponding to the faradic charge-transfer behavior. The polarization resistance is equal to the intercept segment of the semi circle with the real impedance axis. On the other hand, mass transfer control is the straight line at low frequencies and corresponds to the linear diffusion process of oxidized and reduced species and is realized by the Warburg impedance.

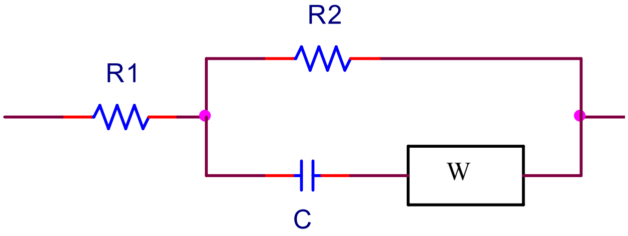

Figure 5.9 – Warburg impedance interface model

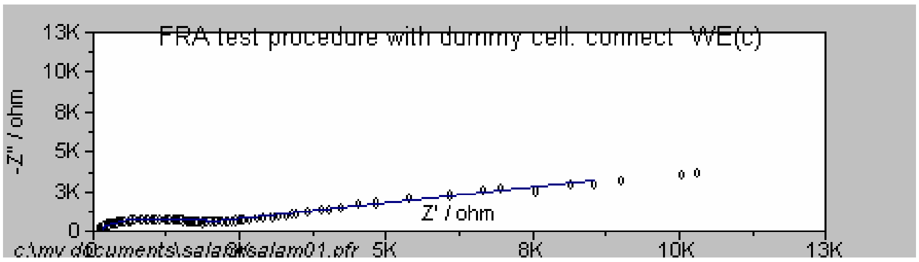

Figure 5.10 – Experimental vs. Mixed Kinetic and Diffusion Control circuit Nyquist plot

Table 5.5 – Mixed Kinetic and Diffusion Control circuit element values

Element	Value	Percentage error
R1	139.4	1.9 %
R2	1.371K	0.85 %
C1	0.965u	0.85 %
W	$1.42\text{x}10^{-4}$	2.53 %

Equivalent Circuit for a Failed (Porous) Coating

The following circuit in figure 5.11 is used for modeling aged coated surfaces where the coat is degraded. Usually, this model is used to evaluate the quality of a coating. The coating capacitance is represented by C_1 and R_2 is the resistance of ion conducting paths that develop in the coating. Though, these paths may not be physical pores filled with electrolyte.

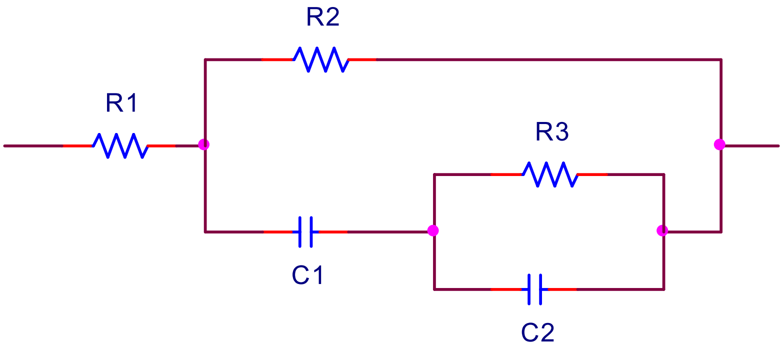

Figure 5.11 – Porous coating circuit model

The response of this network plotted on Nyquist is characterized by the two semicircles as shown in figure 5.12.

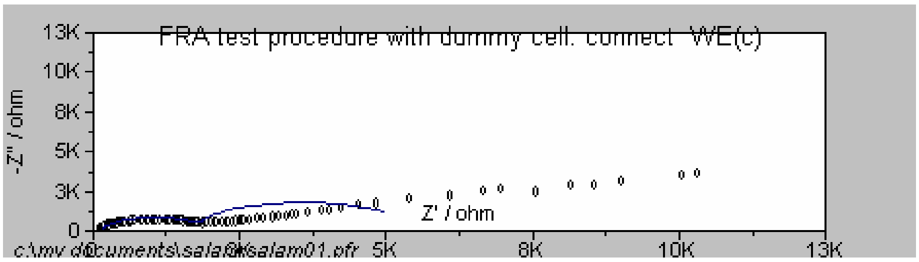

Figure 5.12 – Experimental vs. Porous coating circuit Nyquist plot

Table 5.6 – Porous coating circuit element values

Element	Value	Percentage error
R1	153.4	10.049 %
R2	1.759K	4.457 %
R3	3.49K	11.753 %
C1	1.055u	4.45 %
C2	32.3u	9.88 %

Randles Cell with CPE

Another version of Randles circuit where the capacitor representing the double layer is replaced by a CPE can be used to model the non-linearities in the interface.

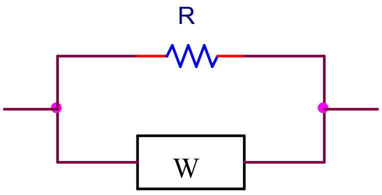

Figure 5.13 – Randles Cell with CPE

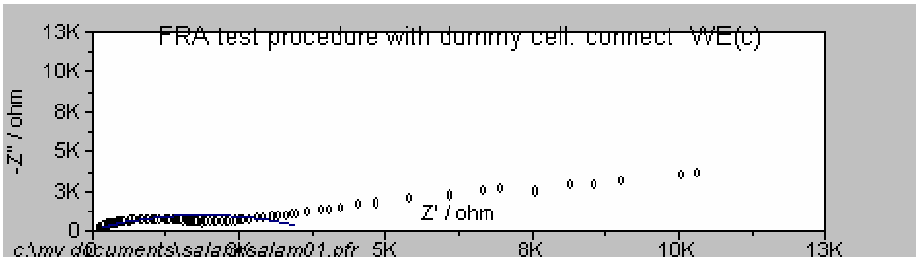

Figure 5.14 – Experimental vs. modified Randles circuit Nyquist plot

Table 5.7 – Modified Randles circuit element values

Element	Value	Percentage error
R1	100	0 %
R2	3.78K	7.4 %
Q	1.655×10^{-7}	41.409 %
α	0.6134	3.822 %

Two Time Constants equivalent circuit

Another model was created using a combination of shunt-series networks can be used to model the interface.

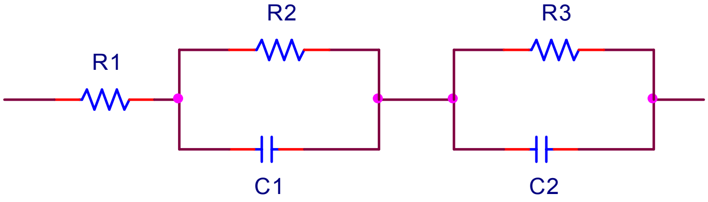

Figure 5.15 – Two Time Constants equivalent circuit

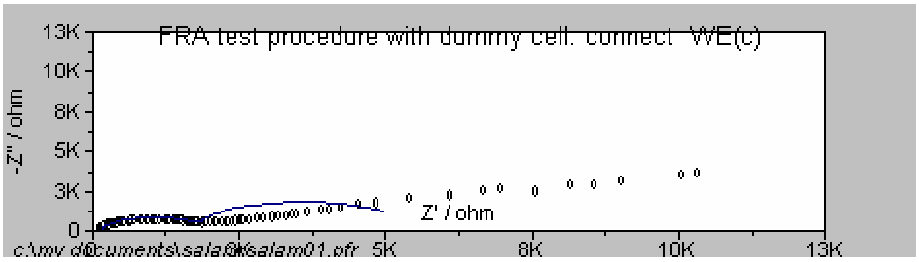

Figure 5.16 – Experimental vs. Two Time Constants circuit Nyquist plot

Table 5.8 – Two Time Constants circuit element values

Element	Value	Percentage error
R1	153.4	10.05 %
R2	1.647K	4.02 %
R3	3.6K	11.38 %
C1	1.091u	4.5 %
C2	32.4u	9.8 %

5.1.6 Discussion

The result of above discussion shows that the skin-electrode interface can be modeled as a mixed kinetic and diffusion control using Warburg impedance element as shown in figure 5.9. This equivalent circuit will be integrated in the skin-electrode model to create the system equivalent circuit.

5.2 Skin-Electrode circuit model

5.2.1 Introduction

The last step in this analysis is to create the circuit model of the electrode-skin system and evaluate the impedance which constitutes the source impedance as seen by the amplifier.

5.2.2 Electrode equivalent circuit

The conventional circuit used to model the electrode-gel and gel-skin interfaces is shown in figure 5.17. This system has two interfaces each containing a double layer which is mainly capacitive.

Using dry spiked electrode, the system electrical structure is changed and the two interfaces are replaced by a single electrode-electrolyte interface representing the interaction between the electrode and extra-cellular fluid. The equivalent circuit for the dry electrode proposed in this thesis is compiled from the skin electric model in section 4.2.4 and the electrochemical impedance spectroscopy experimental results in section 5.1.5. The circuit model is sketched in figure 5.18 where there only exists a single double layer interface and the skin impedance is void of the stratum corneum.

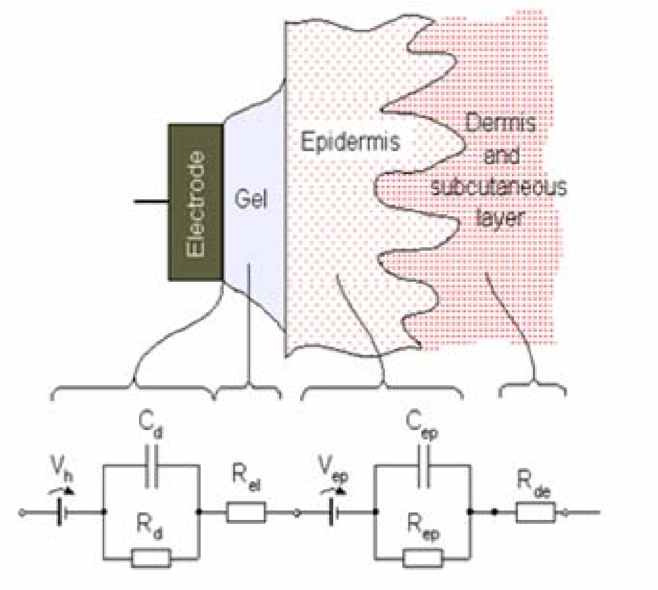

Figure 5.17 – Wet electrode system equivalent circuit [45]

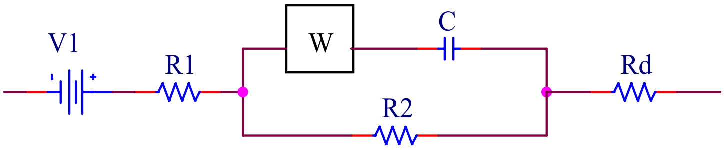

Figure 5.18 – Spiked array electrode equivalent circuit model

Table 5.9 – Spiked array electrode equivalent circuit values circuit element values

Element	Value
R1	139.4
R2	1.371K
C	0.965u
W	$1.42\text{x}10^{-4}$
V1	N/A
Rd	100

5.2.3 Bioamp considerations

The electrode-electrolyte impedance is a function of frequency and current density. This implies that the input stage of the bioamplifier coupled to the electrode has to have impedance sufficiently high to keep the drawn current at its minimal. Moreover, polarization voltage which can be regarded as DC offset voltages required DC suppression at the inputs of the amplifier. Suppressing the polarization voltage is not affected by the common mode rejection ratio as the magnitude of the polarization voltage differs between electrodes due to the difference in the electrolyte composition at each electrode spot.

5.3 Conclusion

The electrode-skin interface impedance was evaluated experimentally using Potentiostatic frequency scanning and the Nyquist plot of the real and imaginary impedance was used to create the circuit model. The circuit model is shown in figure 5.18. The proposed electrode exhibits low impedance which is much lower than the conventional wet electrodes.

Chapter 6

Micro-fabrication

6.1 Introduction

The purpose of this recipe is to fabricate a square array of metallic micro-needles according to the layout generated by the design optimization technique. Different technologies can be used and the recipe targets an economic fabrication process based on micro-molding and electroplating.

6.2 Creating the micro-mold

A polymer micro-mold is fabricated using SU-8 epoxy substrate on a silicon wafer using photolithography and wet etching procedures. Prior to filling the mold with a metal by electroplating, a metallic seed layer is deposited on the mold by sputtering. Finally, a lead wire is attached to the back of the electrode base and the mold is stripped using wet etching.

6.3 Why SU-8

SU-8 is a negative photoresist epoxy polymer, developed at IBM-Watson Research Center [118] and was adopted for MEMS devices and micro-fabrication and it is known for its mechanical stability, biocompatibility, and suitability for fabricating high aspect ratio features [119] [120] [121]. It is polymerized by cationic photo-polymerization and exhibits high transparency at wavelengths above 340 nm. These make it an inexpensive alternative to LIGA process [122]. It is suitable for making electroplating molds, injection molding masters and embossing masters for structures with high aspect ratio [123] [124].

The main setback in using SU-8 is stripping where SU-8 is difficult to remove using ordinary methods. This makes it more suitable for permanent structures where it is imaged, cured and left in place [121].

SU-8 is also sensitive to electron beam exposure and has several advantages in some applications when compared to the most widely used e-beam resist, polymethyl methacrylate (PMMA):

First, SU-8 has a much higher sensitivity which greatly reduces the time required to expose a given pattern.

Second, cross-linked (fully exposed) SU-8 is an optically transparent epoxy that is chemically and physically durable. For many applications these properties eliminate the need for a dry-etch pattern transfer into a more durable substrate.

Finally, at electron beam voltages in the 10 – 30 kV range, SU-8 bas a much lower contrast than PMMA, which for analog profiles reduces surface roughness due to shot noise of the electron source. One important difference that must be kept in mind is that SU-8 is a negative tone resist while PMMA is a positive tone resists [123].

6.4 Process

Fabrication process includes two stages, the SU-8 mold is first made in the α-SiDIC class 1000 clean room, then sputtering and electroplating was done in the CIRFE class 1000 clean room and lab.

An 80µm film of SU-8 in spin coated using Laurell spinner on silicon and glass wafers then soft-baked to evaporate the solvent. Soft-baking was ramped to avoid formation of crust and bubbles. This step was repeated twice; where in each step a 40µm thick layer was formed. This technique avoids having solvent gradient through the SU-8. Edge bead formation was prevented by partial coating of the wafer. UV exposure was according to a doze which depends on the polymer layer thickness and was done along with mask alignment on Carl SUSS mask aligner. SU-8 epoxy is cross-linked by UV exposure and heating, and different post-exposure bake (PEB) patterns were experimented until the optimal pattern was identified which minimizes the residual stresses and hardens the SU-8 mold. This was followed by developing the sample in SU-8 developer on a wet bench and this step fixes the mold structure and strips the void where the spikes will be formed by electroplating.

Fabrication steps are illustrated in figures 6.1 through 6.14.

Different structures were manufactured including 30µm, 50µm and 1000µm square spikes and, 30µm and 60µm cross spikes to test the fabrication process. Finally, the mold was created and sputtered using Intelvac Nanochrome Deposition System. These steps were successfully accomplished by the time the thesis was written and the following steps involve electroplating, wire attachment using conductive epoxy and plasma deposition of antifouling film were not yet completed.

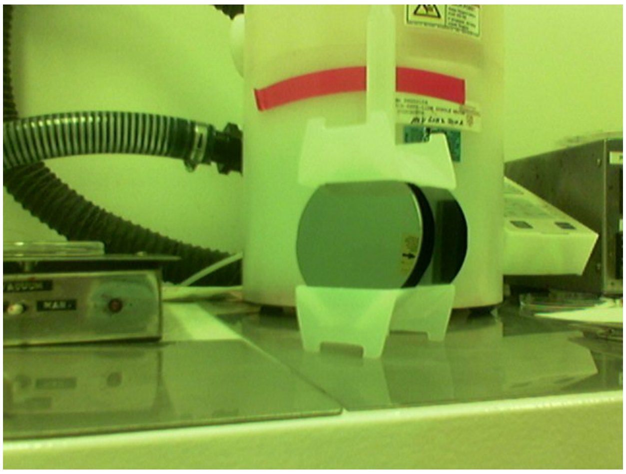

Figure 6.1 – Substrate

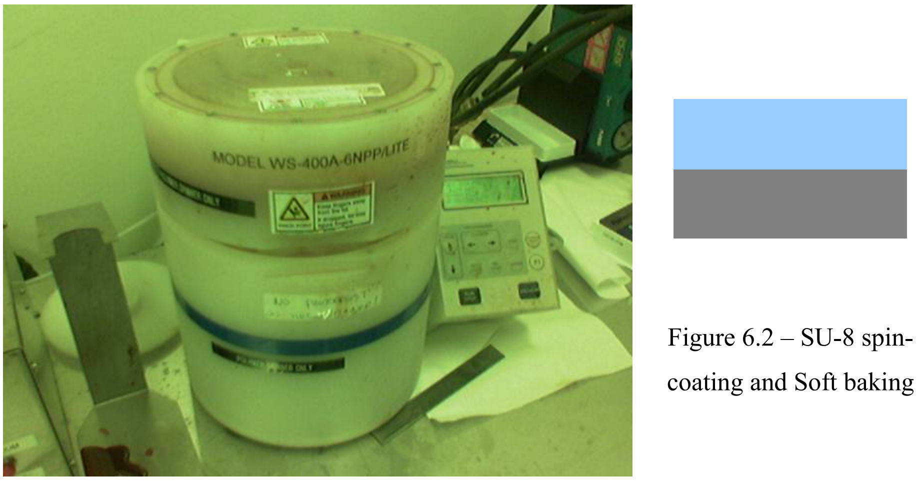

Figure 6.2 – SU-8 spin-coating and Soft baking

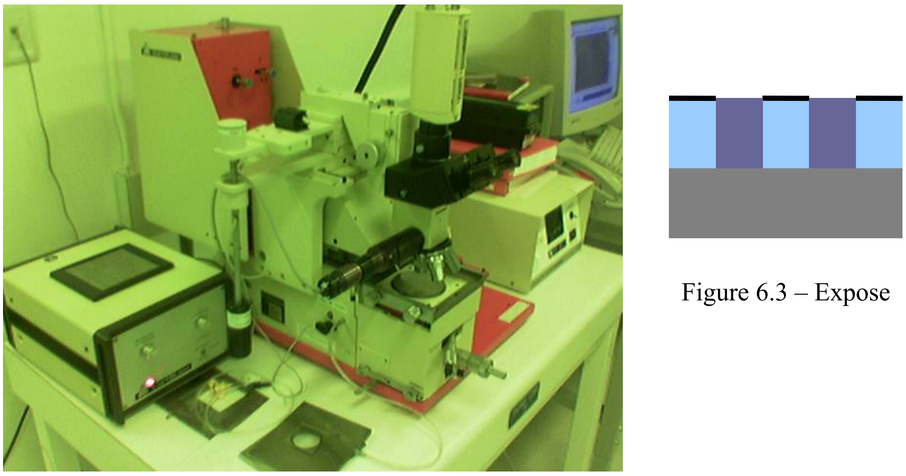

Figure 6.3 – Expose

Figure 6.4 – PEB and Develop

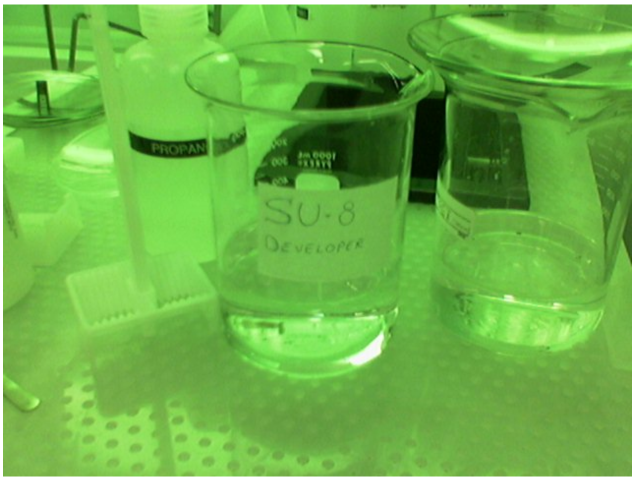

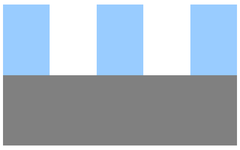

Figure 6.5 – Wet etching SU-8

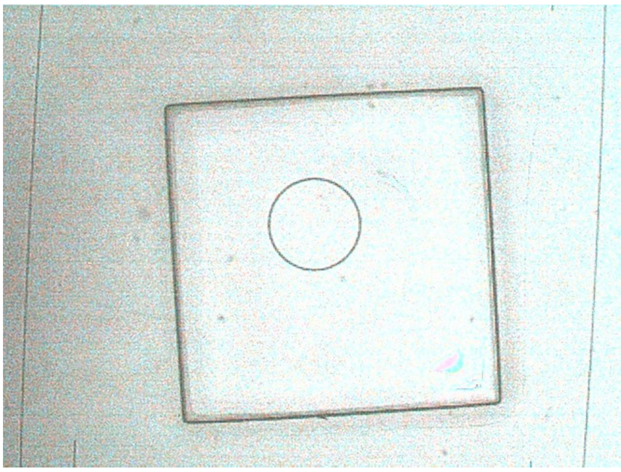

Figure 6.6 – 40 µm deep Square grove with 1000µm side length

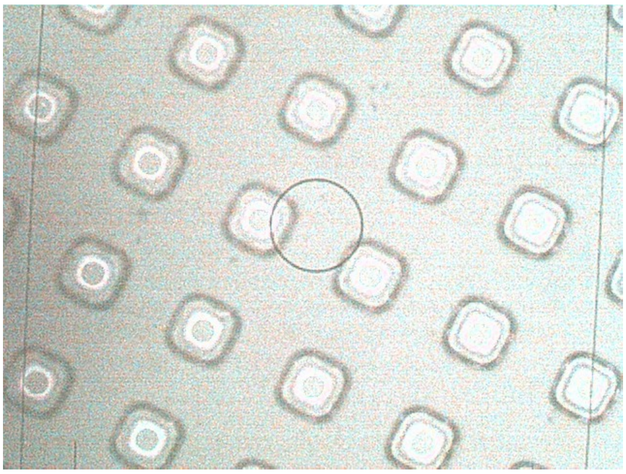

Figure 6.7 – 40 µm deep Square groves with 50µm side length and 50µm spacing

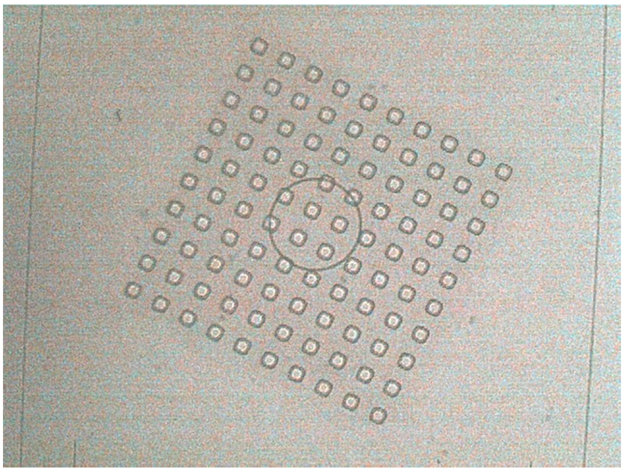

Figure 6.8 – 40 µm long SU-8 spikes with 30µm side length and 50µm spacing

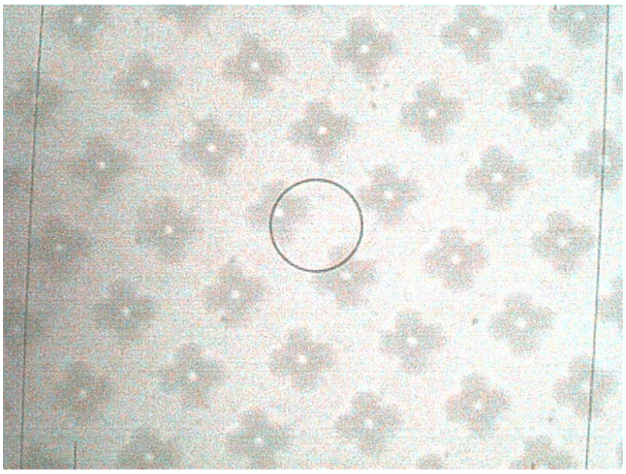

Figure 6.9 – 80 µm Cross groves with 30µm side length

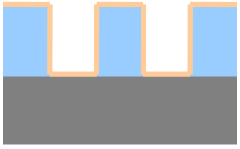

Figure 6.10 – Sputter Cu seed layer

Figure 6.11 – Electroplating

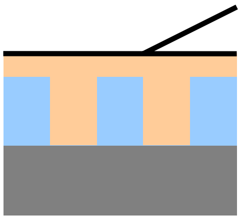

Figure 6.12 – Attach wire

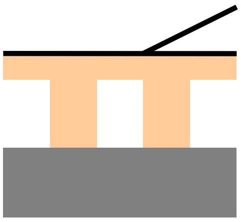

Figure 6.13 – SU-8 lift off

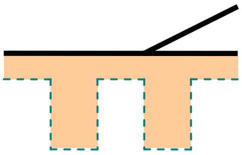

Figure 6.14 – Anti-fouling coating by plasma deposition

6.5 Conclusion

In this chapter the fabrication process is explained and some fabrication attempts are shown. SU-8 can be used for making the mold, but it is not suitable for creating the needles as according to the mechanical constraints, large spike dimensions is required to handle the insertion forces.

Chapter 7

Conclusions and Future work

7.1 Conclusion

Emerging applications involving electrophysiological measurements encourages improving the current technologies as well as developing new techniques to satisfy the design specifications.

The thesis objective is the design and optimization of spiked array dry EEG electrodes customized for portable long-term recording for application in narcolepsy assistive device which requires real-time monitoring of the EEG spectrum for predicting narcolepsy attacks. Current electrode technologies including wet and dry surface electrodes are customized for short term clinical recording and do not exhibit the required characteristics that can satisfy the design specifications.

The design specifications for electrodes used in portable narcolepsy assistive device can be briefed as follows:

- Low electrode impedance, below 5KΩ
- Good mechanical adhesion without gel, suitable for portable applications
- Low sensitivity to electrode displacement artifacts
- Biocompatibility and suitable for prolonged recording causing minimum tissue response
- Small number of channels and recording spots
- Fast and easy application and cleaning, neither gel nor skin preparation are allowed
- High immunity to electromagnetic interference
- Maximum axial force per spike is 0.01N
- Maximum horizontal force per spike is 0.1N (4 Kg.f per electrode with 400 spikes)

Starting with section 2.3, the EEG spectrum was chosen as the signal of interest for the application. According to the electrical properties of the EEG spectrum which is characterized by extremely low voltage levels and low frequency content (sections 2.2.2, 2.2.3); it is required to minimize the electrode impedance and use high gain single stage bio-amplifier to improve the signal to noise ratio. In order to overcome the electromagnetic interference, differential recording was used (sections 2.2.10 and 2.2.11). Choosing the recording spots depends on the application; in the case of narcolepsy prediction and based on clinical information, two channels are required and distant recording spots are preferred to overcome the skull resistivity (section 2.2.12), thus spots C3/A2 are used for channel 1 and O2/A1 for channel 2.

Due to the limitations of wet electrode technology (short term clinical recording and the need for skin preparation), it is not suitable for this application (sections 3.3 and 3.4). On the other hand, the dry electrode design proposed in this thesis can potentially satisfy the design specifications in terms of long-term recording together and suitability for portable recording.

Based on the physiological constraints and skin anatomy in section 4.1, the spike length is chosen to be 80µm, which will place the electrode in contact with the viable skin layers but will avoid contact with the dermis where the blood capillaries and nerve endings exist. This will avoid pain and bleeding while applying the electrode. Long term interaction with the skin invokes tissue reaction, cytotoxic responses and protein adhesion (sections 4.3 and 4.4), accordingly; silver was chosen as it exhibits the required biocompatibility and inertness during long-term skin contact.

Different geometries were explored and analyzed in pursue of the optimal electrode architecture that maximizes the total spike perimeter which is directly proportional to the contact surface area (section 4.5). Using the custom designed optimizer; the total perimeter was found to be a function of the product needle-count and needle-radius. As the electrode base area increases, it can accommodate more needles and consequently, the perimeter will expand.

Two electrode designs with different base area were proposed, the first electrode has a base side area of 1000µm x 1000µm and the other was 3000µm x 3000µm square. The minimum feature size was limited by the fabrication technology to 30µm. The Cross-1 electrode design provided the largest surface area of contact and was chosen for implementation. The smallest electrode dimensions are listed in table 4.25 where the mechanical analysis in sections 4.6 through 4.8 showed that the minimum side length for Cross-1 architecture silver electrodes is 60.8µm while for triangle prism is 207µm.

Using the design optimization methodology, the proposed electrode designed is compared to another design proposed in [24] and [62] in table 7.1. This electrode is made of an array of silicon cylindrical prisms coated with a silver layer. The spikes are 40µm in diameter with a spacing of 100µm. optimizing the electrode design and layout will expand the contact surface area by a factor of 2.39 and 2.4 in the case of 2000µm and 4000 µm base side lengths, respectively. Looking at this result from another perspective, the same contact surface area can be achieved by a smaller electrode. Thus a 2000µm x 2000µm electrode can be replaced by a 1290µm x 1290µm electrode and a 4000µm x 4000µm electrode can be replaced by a 2580µm x 2580µm electrode decreasing the area by a factor of 2.4 in both cases.

The fabrication technique used in this thesis fulfills the size and economic constraints of the design specifications where only single step emulsion mask is needed to realize the required dimensions and spike spacing. As well as it is suitable for mass production.

Table 7.1 – Comparing the proposed design methodology to other design approaches

Geometry	Base width	Needles	Radius/Side	Total perimeter	Area usage
Circle	2000	157	40	39458	99.88%
Cross-1	2000	127	62	94488	99.13%
Circle	4000	628	40	157834	99.88%
Cross-1	2000	511	62	380184	99.90%

Finally, the electrode-skin interface electric model is presented in section 5.2.2, which shows that the proposed electrode design exhibits lower impedance than the wet electrode.

Finally, the candidate design for implementation with the portable EEG monitoring based narcolepsy assistive device is shown in figure 4.40 and the equivalent electrical model in figure 5.18 and table 5.9. This design meets the design specifications in terms of the mechanical and electrical performance as well as being biocompatible and suitable for long term recording with the minimal tissue response.

7.2 Future work

A clinical trial is required for testing the electrode and measuring the electrode-skin impedance. Future work in sub-dermal EEG electrodes will focus on two main activities. The first involves developing a cost effective fabrication protocol capable of offering smaller features and suitable to meet the design specifications. Second, integrating the electrode and the bio-amplifier on the same substrate to cut the size and improve the signal quality.

Appendix A

Applications - Narcolepsy assistive device

A.1 Introduction

Narcolepsy is a chronic neurological disorder of sleep regulation characterized by uncontrollable recurring episodes of daytime sleep and cataplexy. The episodes may last from few minutes up to a complete hour and are accompanied by intrusion of the dreaming state -known as the rapid eye movement sleep- into the waking state [25] [125]. The exact cause of narcolepsy is currently unknown, but some theories and studies relate narcolepsy to the lack of hypocretin peptides in the brain which are neurotransmitters in the hypothalamus involved in regulating sleep [125].

An undiagnosed patient potentially will be suffering from narcolepsy drawbacks that will hinder the daily activities and normal flow of life. Referring to a survey carried by the UK narcolepsy patient association based to the Beck Depression Inventory (BDI), degrees of depression are common among narcolepsy patients [127]. This is an expected evolution to a series of social, educational, psychological, and financial difficulties experienced by narcoleptics [128] [129] [130] [131] [132].

A.2 Narcolepsy symptoms

In brief, the key symptoms of narcolepsy are excessive daytime sleepiness, cataplexy, sleep paralysis and hypnagogic hallucinations.

The following points highlight the symptoms elaborately:

- Excessive daytime sleepiness (EDS): A state of involuntary sleepiness and extreme exhaustion which interferes with normal activities regardless of the sleeping habits. The EDS attack may be a microsleep lasting for few seconds or as long as an hour.
- Cataplexy: A sudden attack of muscle weakness and loss of muscle tone aroused by strong emotional response.
- Sleep paralysis: Momentary inability to move or speak while falling asleep or waking up which is similar to a cataplectic attack affecting the entire body.
- Hypnagogic sleep paralysis: Brief episodes of paralysis occurring when falling asleep.
- Hypnopompic sleep paralysis: Brief episodes of paralysis occurring when waking up.
- Hypnagogic hallucinations: Vivid hallucinations occurring at the onset of sleep.
- Hypnopompic hallucinations: Vivid hallucinations occurring after waking up.

It is clear that the symptoms of this encephalon disorder may hinder the patient from enjoying a normal and productive life. Also the nature of the symptoms makes the patient not able to provide the physician with detailed information regarding the progress of the illness. This stalls the conventional treatment practices and accordingly; the device software extracts the required objective information to provide first hand data to the physician.

A.3 EEG spectrum and narcolepsy diagnosis

Narcolepsy symptoms are common with other disorders as well, and the uncertainty is resolved by recording the brain's electrical activity using electroencephalography (EEG) which is performed in a sleep laboratory. The EEG spectrum of narcolepsy is characterized by the presence of REM-type sleep activity right after falling asleep, rather than later in the sleep cycle as it normally does.

A.4 A narcolepsy cure

At the time of writing this thesis, no cure was yet developed for narcolepsy, nevertheless; the behavioral and medical therapy can manage the symptoms and reduce their intensity and rate of occurrence. As a matter of fact, excessive daytime sleeping (EDS) and cataplexy (which are the main sources of disability) can both be controlled with drug treatment. Using central nervous system stimulants-amphetamines to control EDS has effective results, but side effects are inherent in pharmacological treatment and impose many undesired risks; for instance, amphetamines impose a potential risk of abuse. A non-amphetamine drug was recently approved by the FDA for treating EDS; in the end, the patient is likely to develop tolerance to these types of medication [133].

The proposed solution is a technological treatment for the narcolepsy patients in the form of a portable device that undergoes real-time sleep and alertness monitoring and analysis. This device is remarkably different from vigilance monitoring systems [134] [135] in terms of the expanded tasks and capabilities. The system is customized to be used by narcolepsy patients, thus the primary task is to assist narcolepsy patients through providing real-time monitoring of the electroencephalogram (EEG) spectrum, and responding to the sleep and awareness states of the patient by issuing alerts in case of a potential narcolepsy attack, finally eliciting the objective data required by the treating physician.

A.5 Narcolepsy assistive device

A.5.1 General review of the device tasks

Data acquisition

As mentioned before, diagnosing narcolepsy is based on EEG monitoring and analysis, thus the first stage of the device is EEG recording.

EEG signal conditioning

The detected signal is very low in amplitude (20µ – 200 µV); therefore single step high voltage gain amplification is required to keep the distortion to minimum.

Sleep detection

Artificial intelligence algorithms perform the sleep analysis and detection in real-time to provide warnings for potential attacks and extract objective information required by the physician without the intervention of the patient to ensure first-hand accurate data which will help in improving the medical treatment, assessment and drug administration. The sleep detection algorithms are adaptable to increase reliability and avoid issuing future false alarms. The algorithm has to adapt to each patient's signal levels and patterns which are dependant on parameters such as gender and age. Details about the software layer will not be discussed as it is not a part of this thesis.

Data logging

The device has a serial port connection to upload the data to the physician's PC.

A.5.2 Device design

The device is designed to be portable and the architecture is optimized for minimizing power consumption and size, as well as keeping the cost at minimal while not compromising performance and reliability.

Referring to the device block diagram in figure A.1, the signal flow starts with recording the EEG spectrum where dry electrodes are used to convert the bioelectric potentials into an electric current which is fed into the signal conditioning circuit for amplification and limiting the signal bandwidth to reduce the noise content. Filtering the 50 and 60Hz mains interference is not required because the device is running on batteries. Dry electrodes are more suitable in this application than wet gel electrodes due to long operation time and ease of use where no skin preparation is required. The following step is the digitization of the EEG signals; sigma-delta ADCs showed good performance, but the final design is built using a 10 bits Nyquist rate ADC integrated in the microcontroller which is also the master CPU of the device. This cuts the part count and the cost as well as the power consumption. After analogue to digital conversion, the processing unit feeds the EEG stream into the digital signal processor which is dedicated for executing the sleep detection, classification and staging algorithms. Finally, the user interface displays the information produced by the expert system software briefing the patient about the current state and warning of potential attacks, besides to operational information like a loose electrode and battery status. Finally, an interface circuit connects the device to the physician's PC via a serial port to download the objective information required treatment. The expert system software along with the sleep algorithms resides in the digital signal processor memory while the operating system firmware is stored in the microcontroller's flash memory.

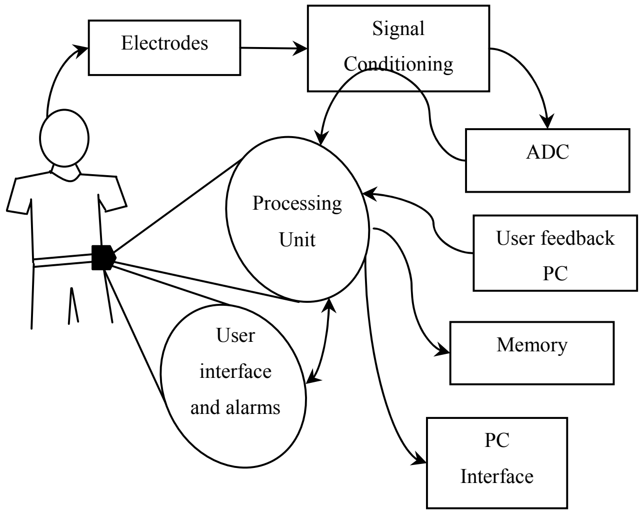

Figure A.1 – Device block diagram

Appendix B

10-20 system electrode placement

Electrode placement is relative to different reference points identified as nasion (the top of the nose), inion (bony lump at the base of the skull on the midline at the back of the head), right and left pre-auricular points. Based on these points, the skull perimeters are measured in the transverse and median planes and recording spots are determined by dividing these perimeters into 10% and 20% intervals. Another three electrodes are placed as shown in figure 2.2 [16] [136]. In addition, intermediate 10% electrode positions (figure B.1) are standardized by the American Electroencephalographic Society18.

Scalp locations are designated by an abbreviation using letters that refer to cerebral regions and numbers for relative locations where even numbers indicate right sided locations and odd numbers refer to left sided locations. Moreover, low numbers are closer to the midline and high numbers are more lateral. An electrode placed on the midline is referred to by the letter ‘z’ which stands for zero displacement.

The letter indicates the location on the cortical lobe above which the electrode lies:

- Fp: frontal pole
- F: frontal
- C: central
- T: temporal
- P: parietal
- O: occipital

Combinations of two letters indicate intermediate locations, for example: FC lies in between frontal and central electrode locations and PO is in between parietal and occipital electrode locations.

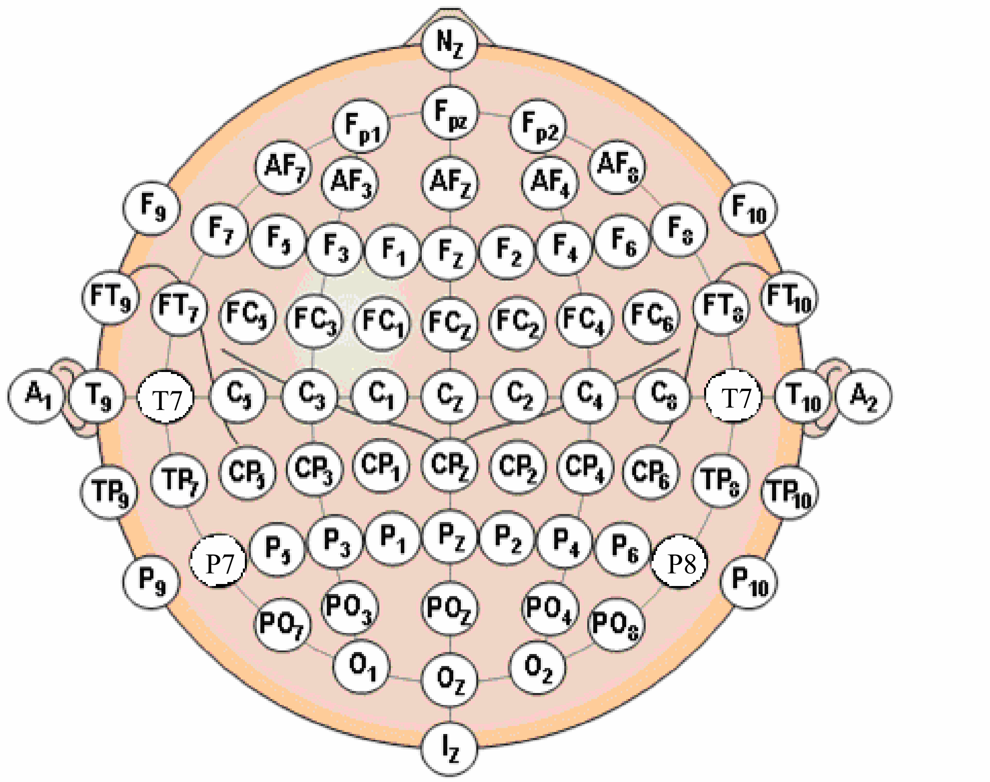

Figure B.1 – Location of the standard intermediate 10% electrodes [7]

Appendix C

Corrosion

C.1 Chemistry of corrosion

Metal corrosion is caused by different reactions including:

1. Ionization: in an acidic environment, a metal will form cations:

$M \rightarrow M^+ + e^-$

2. Oxidation: reaction with oxygen:

$M + O_2 \rightarrow MO_2$

3. Hydroxylation: reaction of a metal with water in an alkaline environment:

   $2M + O_2 + 2H_2O \rightarrow 2M(OH)_2$

4. Reaction: ordinary reactions with other ions

C.2 Forms of corrosion [60]

The insertion of a metallic structure in an ionic solution invokes reactions which yields the release of metallic cations in the ionic solution. The electrode will experience the following forms of corrosion:

1. Uniform attack

The presence of electrodes in an environment lacking equilibrium concentrations of their constituent ions leads to corrosive interaction with the ambient ionic solutions. This type of corrosion is measured in terms of surface recession (mils per year). On Pourbaix diagram (will be discussed in a following section), this occurs in the corrosion region as well as in the passivation region in the form of oxide/hydroxide dissolution.

Equation 4.1 describes the uniform attack as a function of contact area (A), alloy density (D), time of exposure (T) and weight loss (w):

$$\text{mpy} = \frac{534.\text{w}}{\text{D.A.T}} \qquad \text{(C.1)}$$

2. Crevice corrosion

It depends on the structure geometry, and is agitated by static non-flowing conditions which increase the concentration of the metal ions. Due to the micro-dimension and presence of vias, the electrode is susceptible to crevice corrosion.

3. Stress and fatigue corrosion

Chemical activity is amplified by tensile stresses. The fabrication steps are adjusted to decrease the residual stresses during soft and post-exposure baking.

Other forms of corrosion defined by Fontana, 1986 include

4. Galvanic corrosion

It is the result of contact between two different metals in an ionic solution. The two metals will have different potentials for a certain pO_2 (pH and potential combination on Pourbaix diagram). The less noble metal will lose ions under uniform attack and will be the anode while the more noble metal will be the cathode and will attract electrons.

The lead connecting wire attached to the back of the electrode is present outside of the body thus it is not in contact with the ionic media; therefore it will not influence galvanic carrion. Furthermore, using identical metals for the electrodes inhibits this form of corrosion.

5. Pitting corrosion

Scratches and handling damage causes another form of crevice corrosion know as pitting corrosion. It is remarkable in points of stress concentrations and can invoke cracks.

6. Erosion corrosion

This is caused by friction due to relative movement between a fluid and a surface. It also aggravates corrosion of other forms by sweeping away the high concentration of ions that inhibit the corrosion.

Appendix D

Analytical buckling analysis

A: Fixed-Free boundary condition

The fixed-free boundary condition is tighter than fixed-fixed condition, thus it will be used as a worst case scenario.

Effective length:

$L_e = (2.1).L$

Case 1: Solid triangular prism – general case

$$\text{Area} = 3.\left(R_{In}\right)^2.\tan\left(60\right) = \frac{\sqrt{3}}{4}.a^2$$

$$\text{Perimeter} = 6.R_{In}.\tan\left(60\right) = 3.a$$

$$\therefore a = 2.\sqrt{3}.R_{in}$$

a: triangle side length

R_{in}: inradius of the triangle

Moving the origin to the centroid:

Center of area from origin:

x = a/2

y = a.Sin(60)

$y_1 = y/3$

$y_2 = 2.y/3$

Moment of inertia about x-axis:

$$I_X = \frac{a.h^3}{36} = \left(\frac{\sqrt{3}}{2}.a\right)^3.\frac{a}{36} = \frac{\sqrt{3}}{96}.a^4 = \frac{3\sqrt{3}.R^4}{2}$$

The slenderness ratio:

$$r = \sqrt{\frac{I_x}{A}} = \frac{R}{\sqrt{2}} = \frac{a}{2\sqrt{6}}$$

L = 80μm

$$S = \frac{L_e}{r} = \frac{823.029x10^{-6}}{a} = \frac{237.588x10^{-6}}{R}$$

Silver:

The critical slenderness ratio:

$$S_{Cr} = \sqrt{\frac{2.\pi^2.E}{\sigma_y}} = 174.184$$

Euler's formula:

$$P_{Cr\_Buckling} = \frac{\pi^2.E_{Titanium}.I_X}{L_e^2} = 5.23659x10^{17}.a^4 N$$

$$P_{Cr\_Buckling} = 5.23659x10^{17}.a^4 > 1$$

$$\therefore a > 37.1739\mu m$$

J. B. Johnson's formula:

$$P_{Cr\_Buckling} = \sigma_y.A.\left[1 - \left(\frac{S^2}{4.\pi^2.E}\right).\sigma_y\right] = 2.33827x10^7.a^2.\left(1 - \frac{1.11631x10^{-11}}{a^2}\right) N$$

$$P_{Cr\_Buckling} = 2.33827x10^7.a^2.\left(1 - \frac{1.11631x10^{-11}}{a^2}\right) > 1$$

$$\therefore a > 207\mu m$$

Testing the slenderness ratio:

P_{CR_Euler}: S=2.14 < S_{Cr}

$P_{Cr\_Johnson}$: S=3.97599 < S_{Cr}

$P_{Cr\_Johnson}$ is the valid value.

Case 2: Hollow triangular prism – general case

$$\text{Area}_{\text{Outer}} = 3.\left(R_{\text{In}}\right)^2.\tan\left(60\right) = \frac{\sqrt{3}}{4}.a_o^2$$

$$\text{Perimeter} = 6.R_{\text{In}}.\tan\left(60\right) = 3.a_o$$

$$\therefore a_o = 2.\sqrt{3}.R_{\text{in}-o}$$

a: triangle side length

R_{in}: inradius of the triangle

Moment of inertia about x-axis:

$$I_X = \frac{a.h^3}{36} = \left(\frac{\sqrt{3}}{2}.a_o\right)^3.\frac{a}{36} = \frac{\sqrt{3}}{96}.a_o^4 = \frac{3\sqrt{3}.R_o^4}{2}$$

The slenderness ratio:

$$r = \sqrt{\frac{I_x}{A}} = \frac{R_o}{\sqrt{2}} = \frac{a_o}{2\sqrt{6}}$$

L = 80μm

$$S = \frac{L_e}{r} = \frac{823.029\text{x}10^{-6}}{a} = \frac{237.588\text{x}10^{-6}}{R}$$

Silver:

The critical slenderness ratio:

$$S_{Cr} = \sqrt{\frac{2.\pi^2.E}{\sigma_y}} = 174.184$$

Euler's formula:

$$P_{Cr\_Buckling} = \frac{\pi^2.E_{\text{Titanium}}.I_X}{L_e^2} = 5.23659\text{x}10^{17}.a^4\text{N}$$

$$P_{Cr\_Buckling} = 5.23659\text{x}10^{17}.a^4 > 1$$

$$\therefore a_o > 37.1739\mu m$$

J. B. Johnson's formula:

$$P_{Cr\_Buckling} = \sigma_y.A.\left[1-\left(\frac{S^2}{4.\pi^2.E}\right).\sigma_y\right] = 2.33827x10^7.a^2.\left(1-\frac{1.11631x10^{-11}}{a^2}\right)N$$

$$P_{Cr\_Buckling} = 2.33827x10^7.a^2.\left(1-\frac{1.11631x10^{-11}}{a^2}\right) > 1$$

$$\therefore a_o > 207\mu m$$

Testing the slenderness ratio:

P_{CR_Euler}: S=2.14 < S_{Cr}

$P_{Cr\_Johnson}$: S=3.97599 < S_{Cr}

$P_{Cr\_Johnson}$ is the valid value.

Case 3: Solid cylindrical prism – general case

$$\text{Area} = \pi.\left(\text{R}\right)^2$$

$$\text{Perimeter} = 2.\pi.\text{R}$$

Moment of inertia about x-axis:

$$\text{I}_\text{X} = \frac{\pi.\text{R}^4}{4}$$

The slenderness ratio:

$$\text{r} = \sqrt{\frac{\text{I}_\text{x}}{\text{A}}} = \frac{\text{R}}{2}$$

L = 80μm

$$\text{S} = \frac{\text{L}_\text{e}}{\text{r}} = \frac{336\text{x}10^{-6}}{\text{R}}$$

Silver:

The critical slenderness ratio:

$$\text{S}_{\text{Cr}} = \sqrt{\frac{2.\pi^2.\text{E}}{\sigma_\text{y}}} = 174.184$$

Euler's formula:

$$\text{P}_{\text{Cr\_Buckling}} = \frac{\pi^2.\text{E}_{\text{Titanium}}.\text{I}_\text{X}}{\text{L}_\text{e}^2} = 2.27955\text{x}10^{19}.\text{r}^4\text{N}$$

$$\text{P}_{\text{Cr\_Buckling}} = 2.27955\text{x}10^{19}.\text{r}^4 > 1$$

$$\therefore \text{r} > 14.4723\mu\text{m}$$

J. B. Johnson's formula:

$$\text{P}_{\text{Cr\_Buckling}} = \sigma_\text{y}.\text{A}.\left[1 - \left(\frac{\text{S}^2}{4.\pi^2.\text{E}}\right).\sigma_\text{y}\right] = 1.69646\text{x}10^8.\text{r}^2.\left(1 - \frac{1.86052\text{x}10^{-12}}{\text{r}^2}\right)\text{N}$$

$$P_{Cr\_Buckling} = 1.69646x10^{8}.r^{2}.\left(1 - \frac{1.86052x10^{-12}}{r^{2}}\right) > 1$$

$$\therefore r > 76.7886\mu m$$

Testing the slenderness ratio:

P_{CR_Euler}: S=23.2168 < S_{Cr}

$P_{Cr\_Johnson}$: S=4.37565 < S_{Cr}

$P_{Cr\_Johnson}$ is the valid value.

Case 4: Cross prism – general case

$$Area = 5.a^2$$

$$Perimeter = 12.a$$

a: Side length

Moment of inertia about x-axis:

$$\mathrm{I_X} = \frac{29.a^4}{12}$$

The slenderness ratio:

$$r = \sqrt{\frac{I_x}{A}} = \sqrt{\frac{29}{60}}.a$$

L = 80μm

$$S = \frac{L_e}{r} = \frac{241.650x10^{-6}}{a}$$

Silver:

The critical slenderness ratio:

$$S_{Cr} = \sqrt{\frac{2.\pi^2.E}{\sigma_y}} = 174.184$$

Euler's formula:

$$P_{Cr\_Buckling} = \frac{\pi^2.E_{Titanium}.I_X}{L_e^2} = 7.01417x10^{19}.a^4 N$$

$$P_{Cr\_Buckling} = 7.01417x10^{19}.a^4 > 1$$

$$\therefore a > 10.9271\mu m$$

J. B. Johnson's formula:

$$P_{Cr\_Buckling} = \sigma_y.A.\left[1-\left(\frac{S^2}{4.\pi^2.E}\right).\sigma_y\right] = 2.7x10^8.a^2.\left(1-\frac{9.62342x10^{-13}}{a^2}\right)N$$

$$P_{Cr\_Buckling} = 2.7x10^8.a^2.\left(1-\frac{9.62342x10^{-13}}{a^2}\right) > 1$$

$$\therefore a > 60.866\mu m$$

Testing the slenderness ratio:

P_{CR_Euler}: S=22.1147 < S_{Cr}

$P_{Cr\_Johnson}$: S=3.9702 < S_{Cr}

$P_{Cr\_Johnson}$ is the valid value.

Case 5: Square prism – general case

$$\text{Area} = a^2$$

$$\text{Perimeter} = 4.a$$

a: Side length

Moment of inertia about x-axis:

$$I_X = \frac{a^4}{12}$$

The slenderness ratio:

$$r = \sqrt{\frac{I_x}{A}} = \frac{a}{2\sqrt{3}}$$

L = 80μm

$$S = \frac{L_e}{r} = \frac{581.969x10^{-6}}{a}$$

Silver:

The critical slenderness ratio:

$$S_{Cr} = \sqrt{\frac{2.\pi^2.E}{\sigma_y}} = 174.184$$

Euler's formula:

$$P_{Cr\_Buckling} = \frac{\pi^2.E_{Titanium}.I_X}{L_e^2} = 2.41868x10^{18}.a^4 N$$

$$P_{Cr\_Buckling} = 2.41868x10^{18}.a^4 > 1$$

$$\therefore a > 25.3574 \mu m$$

J. B. Johnson's formula:

$$P_{Cr\_Buckling} = \sigma_y.A.\left[1-\left(\frac{S^2}{4.\pi^2.E}\right).\sigma_y\right] = 2.7x10^8.a^2.\left(1-\frac{9.62342x10^{-13}}{a^2}\right)N$$

$$P_{Cr\_Buckling} = 2.7x10^8.a^2.\left(1-\frac{9.62342x10^{-13}}{a^2}\right) > 1$$

$$\therefore a > 136.103\mu m$$

Testing the slenderness ratio:

P_{CR_Euler}: S=22.1147 < S_{Cr}

$P_{Cr\_Johnson}$: S=3.9702 < S_{Cr}

$P_{Cr\_Johnson}$ is the valid value.

B: Fixed-Pinned boundary condition

Effective length:

L_e = (0.734).L

Case 1: Solid triangular prism – general case

$$\text{Area} = 3.\left(R_{In}\right)^2 . \tan\left(60\right) = \frac{\sqrt{3}}{4}.a^2$$

$$\text{Perimeter} = 6.R_{In} . \tan\left(60\right) = 3.a$$

$$\therefore a = 2.\sqrt{3}.R_{in}$$

a: triangle side length

R_{in}: inradius of the triangle

Moving the origin to the centroid:

Center of area from origin:

x = a/2

y = a.Sin(60)

y_1 = y/3

y_2 = 2.y/3

Moment of inertia about x-axis:

$$I_X = \frac{a.h^3}{36} = \left(\frac{\sqrt{3}}{2}.a\right)^3 . \frac{a}{36} = \frac{\sqrt{3}}{96}.a^4 = \frac{3\sqrt{3}.R^4}{2}$$

The slenderness ratio:

$$r = \sqrt{\frac{I_x}{A}} = \frac{R}{\sqrt{2}} = \frac{a}{2\sqrt{6}}$$

L = 80µm

$$S = \frac{L_e}{r} = \frac{288x10^{-6}}{a} = \frac{83.0426x10^{-6}}{R}$$

Silver:

The critical slenderness ratio:

$$S_{Cr} = \sqrt{\frac{2.\pi^2.E}{\sigma_y}} = 174.184$$

Euler's formula:

$$P_{Cr\_Buckling} = \frac{\pi^2.E_{Titanium}.I_X}{L_e^2} = 4.28642x10^{18}.a^4 N$$

$$P_{Cr\_Buckling} = 4.28642x10^{18}.a^4 > 1$$

$$\therefore a > 21.9774\mu m$$

J. B. Johnson's formula:

$$P_{Cr\_Buckling} = \sigma_y.A.\left[1 - \left(\frac{S^2}{4.\pi^2.E}\right).\sigma_y\right] = 2.33827x10^7.a^2.\left(1 - \frac{1.36691x10^{-12}}{a^2}\right)N$$

$$P_{Cr\_Buckling} = 2.33827x10^7.a^2.\left(1 - \frac{1.36691x10^{-12}}{a^2}\right) > 1$$

$$\therefore a > 207\mu m$$

Testing the slenderness ratio:

P_{CR_Euler}: S=13.1044 < S_{Cr}

$P_{Cr\_Johnson}$: S=1.3913 < S_{Cr}

$P_{Cr\_Johnson}$ is the valid value.

Case 2: Hollow triangular prism – general case

$$\text{Area} = 3.\left(R_{In}\right)^2.\tan\left(60\right) = \frac{\sqrt{3}}{4}.a_o^2$$

$$\text{Perimeter} = 6.R_{In}.\tan\left(60\right) = 3.a_o$$

$$\therefore a_o = 2.\sqrt{3}.R_{in-o}$$

a: triangle side length

R$_{in}$: inradius of the triangle

Moment of inertia about x-axis:

$$I_X = \frac{a.h^3}{36} = \left(\frac{\sqrt{3}}{2}.a\right)^3.\frac{a}{36} = \frac{\sqrt{3}}{96}.a^4 = \frac{3\sqrt{3}.R^4}{2}$$

The slenderness ratio:

$$r = \sqrt{\frac{I_x}{A}} = \frac{R_o}{\sqrt{2}} = \frac{a_o}{2\sqrt{6}}$$

L = 80µm

$$S = \frac{L_e}{r} = \frac{288x10^{-6}}{a_o} = \frac{83.0426x10^{-6}}{R_o}$$

Silver:

The critical slenderness ratio:

$$S_{Cr} = \sqrt{\frac{2.\pi^2.E}{\sigma_y}} = 174.184$$

Euler's formula:

$$P_{Cr\_Buckling} = \frac{\pi^2.E_{Titanium}.I_X}{L_e^2} = 4.28642x10^{18}.a^4N$$

$$P_{Cr\_Buckling} = 4.28642x10^{18}.a^4 > 1$$

$$\therefore a_o > 21.9774\mu m$$

J. B. Johnson’s formula:

$$P_{Cr\_Buckling} = \sigma_y.A.\left[1-\left(\frac{S^2}{4.\pi^2.E}\right).\sigma_y\right] = 2.33827x10^7.a^2.\left(1-\frac{1.36691x10^{-12}}{a^2}\right)N$$

$$P_{Cr\_Buckling} = 2.33827x10^7.a^2.\left(1-\frac{1.36691x10^{-12}}{a^2}\right) > 1$$

$$\therefore a_o > 207\mu m$$

Testing the slenderness ratio:

P_{CR_Euler}: S=13.1044 < S_{Cr}

$P_{Cr\_Johnson}$: S=1.3913 < S_{Cr}

$P_{Cr\_Johnson}$ is the valid value.

Case 3: Solid cylindrical prism – general case

$$\text{Area} = \pi.r^2$$

$$\text{Perimeter} = 2.\pi.r$$

Moment of inertia about x-axis:

$$I_X = \frac{\pi.r^4}{4}$$

The slenderness ratio:

$$r = \sqrt{\frac{I_x}{A}} = \frac{r}{2}$$

L = 80μm

$$S = \frac{L_e}{r} = \frac{117.44x10^{-6}}{r}$$

Silver:

The critical slenderness ratio:

$$S_{Cr} = \sqrt{\frac{2.\pi^2.E}{\sigma_y}} = 174.184$$

Euler's formula:

$$P_{Cr\_Buckling} = \frac{\pi^2.E_{Titanium}.I_X}{L_e^2} = 1.86593x10^{20}.r^4 N$$

$$P_{Cr\_Buckling} = 1.86593x10^{20}.r^4 > 1$$

$$\therefore r > 8.5561\mu m$$

J. B. Johnson's formula:

$$P_{Cr\_Buckling} = \sigma_y.A.\left[1 - \left(\frac{S^2}{4.\pi^2.E}\right).\sigma_y\right] = 2.7x10^8.r^2.\left(1 - \frac{2.27294x10^{-13}}{r^2}\right)N$$

$$P_{Cr\_Buckling} = 2.7x10^{8}.r^{2}.\left(1 - \frac{2.27294x10^{-13}}{r^{2}}\right) > 1$$

$$\therefore r > 19.5891\mu m$$

Testing the slenderness ratio:

P_{CR_Euler}: S=13.7259 < S_{Cr}

$P_{Cr\_Johnson}$: S=5.99517 < S_{Cr}

$P_{Cr\_Johnson}$ is the valid value.

Case 4: Cross prism – general case

$$\text{Area} = 5.a^2$$

$$\text{Perimeter} = 12.a$$

a: Side length

Moment of inertia about x-axis:

$$I_X = \frac{29.a^4}{12}$$

The slenderness ratio:

$$r = \sqrt{\frac{I_x}{A}} = \sqrt{\frac{29}{60}}.a$$

L = 80μm

$$S = \frac{L_e}{r} = \frac{84.4623x10^{-6}}{a}$$

Silver:

The critical slenderness ratio:

$$S_{Cr} = \sqrt{\frac{2.\pi^2.E}{\sigma_y}} = 174.184$$

Euler's formula:

$$P_{Cr\_Buckling} = \frac{\pi^2.E_{Titanium}.I_X}{L_e^2} = 5.74146x10^{20}.a^4 N$$

$$P_{Cr\_Buckling} = 5.74146x10^{20}.a^4 > 1$$

$$\therefore a > 6.46018\mu m$$

J. B. Johnson's formula:

$$P_{Cr\_Buckling} = \sigma_y.A.\left[1 - \left(\frac{S^2}{4.\pi^2.E}\right).\sigma_y\right] = 2.7x10^8.a^2.\left(1 - \frac{1.17565x10^{-13}}{a^2}\right)N$$

$$P_{Cr\_Buckling} = 2.7x10^{8}.a^{2}.\left(1-\frac{1.17565x10^{-13}}{a^{2}}\right) > 1$$

$$\therefore a > 60.859\mu m$$

Testing the slenderness ratio:

P_{CR_Euler}: S=13.0743 < S_{Cr}

$P_{Cr\_Johnson}$: S=1.38784 < S_{Cr}

$P_{Cr\_Johnson}$ is the valid value.

Case 5: Square prism – general case

$$\text{Area} = a^2$$

$$\text{Perimeter} = 4.a$$

a: Side length

Moment of inertia about x-axis:

$$I_X = \frac{a^4}{12}$$

The slenderness ratio:

$$r = \sqrt{\frac{I_x}{A}} = \frac{a}{2\sqrt{3}}$$

L = 80μm

$$S = \frac{L_e}{r} = \frac{203.412x10^{-6}}{a}$$

Silver:

The critical slenderness ratio:

$$S_{Cr} = \sqrt{\frac{2.\pi^2.E}{\sigma_y}} = 174.184$$

Euler’s formula:

$$P_{Cr\_Buckling} = \frac{\pi^2.E_{Titanium}.I_X}{L_e^2} = 1.97981x10^{19}.a^4 N$$

$$P_{Cr\_Buckling} = 1.97981x10^{19}.a^4 > 1$$

$$\therefore a > 14.9915 \mu m$$

J. B. Johnson’s formula:

$$P_{Cr\_Buckling} = \sigma_y.A.\left[1-\left(\frac{S^2}{4.\pi^2.E}\right).\sigma_y\right] = 54x10^6.a^2.\left(1-\frac{6.81882x10^{-13}}{a^2}\right)N$$

$$P_{Cr\_Buckling} = 54x10^6.a^2.\left(1-\frac{6.81882x10^{-13}}{a^2}\right) > 1$$

$$\therefore a > 136.085\mu m$$

Testing the slenderness ratio:

P_{CR_Euler}: S=22.1147 < S_{Cr}

$P_{Cr\_Johnson}$: S=3.9702 < S_{Cr}

$P_{Cr\_Johnson}$ is the valid value.

Appendix E

Shear and stress analysis

Cases 1 and 2: Solid triangular prism

$$\text{Area} = \frac{\sqrt{3}}{4}.a^2 \tag{4.62}$$

a: triangle side length

Moment of inertia about x-axis:

$$I_X = \frac{a.h^3}{36} = \left(\frac{\sqrt{3}}{2}.a\right)^3.\frac{a}{36} = \frac{\sqrt{3}}{96}.a^4 \tag{4.63}$$

Maximum compressive stress:

$$\sigma_{\text{Compressive}} = -\frac{0.1}{\left(\frac{\sqrt{3}}{4}.a^2\right)} - \frac{P_{\text{Hz}}.80\mu}{\frac{\sqrt{3}}{96}.a^4}.\left(\frac{2}{3}.\frac{\sqrt{3}}{2}.a\right) \tag{4.64}$$

$$\left|\sigma_{\text{Compressive}}\right| < \sigma_{\text{y-compressive}} \tag{4.65}$$

Table E.1 – Solid triangular prism

P_{Hz} (per needle)	Silver	
	Unity	1.5
0.1 N	176 µm	203 µm
0.05 N	144 µm	167 µm
0.025 N	119 µm	139 µm

Case 3: Solid cylindrical prism

$$\mathrm{Area} = \pi.\left(\mathrm{R}\right)^2 \tag{4.66}$$

Moment of inertia about x-axis:

$$\mathrm{I_X} = \frac{\pi.\mathrm{R}^4}{4} \tag{4.67}$$

Maximum compressive stress:

$$\sigma_{\mathrm{Compressive}} = -\frac{1}{\left(\pi.\mathrm{R}^2\right)} - \frac{\mathrm{P_{Hz}}.80\mu}{\frac{\pi}{4}.\mathrm{R}^4}.\left(\frac{1}{2}.\mathrm{R}\right) \tag{4.68}$$

$$\left|\sigma_{\mathrm{Compressive}}\right| < \sigma_{\mathrm{y-compressive}} \tag{4.69}$$

Table E.2 – Solid cylindrical prism

$\mathrm{P_{Hz}}$ (per needle)	Silver	
	Safety factor	
	Unity	1.5
0.1 N	50 µm	58 µm
0.05 N	42 µm	48 µm
0.025 N	35 µm	42 µm

Case 4: Cross 1 prism

$$\mathrm{Area} = 5.\mathrm{a}^2 \tag{4.70}$$

Moment of inertia about x-axis:

$$\mathrm{I_X} = \frac{29.\mathrm{a}^4}{12} \tag{4.71}$$

Maximum compressive stress:

$$\sigma_{\text{Compressive}} = -\frac{1}{5.a^2} - \frac{P_{Hz}.80\mu}{\frac{29}{12}.a^4}.\left(\frac{3}{2}.a\right) \tag{4.72}$$

$$\left|\sigma_{\text{Compressive}}\right| < \sigma_{y-\text{compressive}} \tag{4.73}$$

Table E.3 – Cross 1 prism

P_{Hz} (per needle)	Silver	
	Safety factor	
	Unity	1.5
0.1 N	48 µm	55 µm
0.05 N	39 µm	46 µm
0.025 N	33 µm	38 µm

Case 5: Square prism

$$\text{Area} = a^2 \tag{4.74}$$

Moment of inertia about x-axis:

$$I_X = \frac{a^4}{12} \tag{4.75}$$

Maximum compressive stress:

$$\sigma_{\text{Compressive}} = -\frac{1}{a^2} - \frac{P_{Hz}.80\mu}{\frac{a^4}{12}}.a \tag{4.76}$$

$$\left|\sigma_{\text{Compressive}}\right| < \sigma_{y-\text{compressive}} \tag{4.77}$$

Table E.4 – Square prism

P_{Hz} (per needle)	Silver	
	Safety factor	
	Unity	1.5
0.1 N	126 µm	145 µm
0.05 N	103 µm	118 µm
0.025 N	84 µm	98 µm

Appendix F

Elements of the electrochemical equivalent circuit

Electrolyte Resistance

The electrolyte can be modeled as a resistive element [137] whose value is a function of the ionic concentration, type of ions, temperature and the geometry of the area though which current flows. In a bounded area with area A and length l carrying a uniform current the resistance is defined as:

$$R = \rho.\frac{\ell}{A} \tag{E.1}$$

But in electrochemical cells, current distribution along the electrolyte area is not uniform. Thus to calculate the solution resistance, it is required to determine the current flow path and the geometry of the electrolyte that carries the current.

Double layer Capacitance

The double layer created at the electrode-electrolyte interface has a thickness in the order of angstroms and can be realized as a capacitor or a constant phase element as well [138]. When modeled as a capacitor, it is estimated to be approximately 30μF per cm^2 of electrode area.

Polarization resistance

A polarized electrode has a potential that changes its open circuit value, this causes current flow through the interface due to electrochemical reactions that occur at the electrode surface and the amount of current is controlled by the kinetics of the reactions and the diffusion of reactants both towards and away from the electrode.

The open circuit potential is controlled by the equilibrium between two electrochemical reactions which generate cathodic and anodic currents. The open circuit potential is reached when the cathodic and anodic currents are equal and it is known as mixed potential while the value of the current for either of the reactions is known as the corrosion current. This is the case for corrosion electrodes.

The potential of the cell is related to the current by Butler-Volmer equation [139]:

$$I = I_{corr} \cdot \left(10^{\frac{(E-E_{OC})}{\beta_\alpha}} - 10^{\frac{-(E-E_{OC})}{\beta_c}} \right) \quad \text{(E.2)}$$

where,

I is the measured cell current in amps,

I_{corr} is the corrosion current in amps,

E_{oc} is the open circuit potential in volts,

β_α is the anodic Beta coefficient in volts/decade,

β_c is the cathodic Beta coefficient in volts/decade.

Charge transfer Warburg impedance [137]

Warburg impedance is a result of diffusion which is more effective at low frequencies because the diffusing reactants diffuse farther than in the case of high frequencies and the Warburg impedance increases.

In the case of an infinite thickness diffusion layer, Warburg impedance can be formulated as:

$$Z_\omega = \sigma.(\omega)^{-\frac{1}{2}}.(1-j) \quad \text{(E.3)}$$

$$|Z_\omega| = \frac{\sqrt{2}.\sigma}{\omega^{\frac{1}{2}}} \quad \text{(E.4)}$$

And the Warburg coefficient defined as:

$$\sigma = \frac{R.T}{n^2.F^2.A.\sqrt{2}} \cdot \left(\frac{1}{C_o.\sqrt{D_o}} + \frac{1}{C_o.\sqrt{D_R}} \right) \quad \text{(E.5)}$$

where:

F = Faraday’s constant

A = surface area of the electrode

ω = radial frequency

D_O = diffusion coefficient of the oxidant

D_R = diffusion coefficient of the reductant

n = number of electrons transferred

C = bulk concentration of the diffusing species (moles/cm^3)

A bounded diffusion layer has low frequency impedance expressed as:

$$Z_o = \sigma.\omega^{-\frac{1}{2}}.(1-j).\tanh\left(\delta.\left(\frac{j.\omega}{D}\right)^{\frac{1}{2}}\right) \qquad \text{(E.6)}$$

where,

δ: Nernst diffusion layer thickness

D: an average value of the diffusion coefficients of the diffusing species

σ: Warburg coefficient

Constant phase element

Biomaterials are more complicated to be modeled by simple RC elements and the double layer capacitor act like a constant phase element (CPE). This is increasingly true as the complexity of a circuit model grows. In short, CPE can provide useful modeling element, even if the true nature of the system is unknown [116].

The impedance of a capacitor can be written in as:

$$Z = A.(j.\omega)^{-\alpha} \qquad \text{(E.7)}$$

And in this case, the constant $A = 1/C$ and the exponent $\alpha = 1$. For a constant phase element, the exponent α is less than one. Due to the non-linear response and non-ideal behavior of the double layer, it can be realized by CPE and α can be evaluated experimentally.

Bibliography

1. Plonsey R., *Bioelectric Phenomena*., McGraw-Hill, 1969.
2. Geselowitz D. B., On bioelectric potentials in an inhomogeneous volume conductor. Biophysics Journal 1967, 1-11.
3. Stratton J. A., *Electromagnetic Theory*, McGraw-Hill 1941.
4. Schwan H. P., Kay CF, *Specific resistance of body tissues*. Circ. Res. 1956, 664-670.
5. Smyth W. R., *Static and Dynamic Electricity*, McGraw-Hill 1968.
6. Geselowitz D. B., The concept of an equivalent cardiac generator, Biomedical Scientific Instrumentation 1963, vol. 1, 325-330.
7. Malmivuo, Jaakko, *Bioelectromagnetism : principles and applications of bioelectric and biomagnetic fields*, Oxford University Press, 1995
8. Robert Plonsey, Roger C. Barr, *Bioelectricity, a quantum approach*, Plenum press, 1988
9. Leslie Cromwell, Fred J. Weibell, Erich A. Pfeiffer, *Biomedical instrumentation and measurement*, Prentice Hall, 1980.
10. Joseph J. Carr, John M. Brown, *Introduction to biomedical equipment technology*, Prentice Hall, 2001.
11. Willis J. Tompkins, John G. Webster, *Microcomputer based medical instrumentation,*
12. R. D. Bickford, *Electroencephalography: Encyclopedia of Neuroscience*, Birkhãauser 1987.
13. Leslie Cromwell, Fred J. Weibell, Erich A. Pfeiffer, *Biomedical instrumentation and measurement*, Prentice Hall, 1980.
14. Apple H. P., Burgess R. C., An analysis of the use of active electrodes in electroencephalogram ambulatory monitoring, *Postgrad Medical Journal* 1976, 79-85.
15. Li-Chern Pan, Po- Wei Lin, Fan-Gang Tseng; Chun Lin, Surface biopotential monitoring by needle type micro electrode array, *Proceedings of IEEE Sensors*, 2002, vol. 1, 221 - 224.
16. R Oostenveld, P Praamstra, The five percent electrode system for high-resolution EEG and ERP measurements, *Clinical Neurophysiology*, 2001, 713-719.
17. Jasper H. H., Report of the Committee on Methods of Clinical Examination in Electroencephalography. *Electroencephalography Clinical Neurophysiology* 1958, 370-371.
18. Rush S., Driscoll D. A., EEG-electrode sensitivity - An application of reciprocity. *IEEE Transactions Biomedical Engineering BME* 1969, 15-22.
19. J. Jossinet, G. Kardous, Physical study of the sensitivity distribution in multi-electrode systems, *Clinical Physics Physiological Measurements*, 1987, Vol. 8, 33-37.
20. Puikkonen J., Malmivuo J. A., Theoretical investigation of the sensitivity distribution of point EEG-electrodes on the three concentric spheres model of a human head - An application of the reciprocity theorem. *Tampere University Technical, Institute of Biomedical Engineering Reports* 1987, 71.
21. Suihko V., Malmivuo J. A., Eskola H., Distribution of sensitivity of electric leads in an inhomogeneous spherical head model, 1993
22. Malmivuo, J.; Suihko, V.; Eskola, H., Sensitivity distributions of EEG and MEG measurements, *IEEE Transactions Biomedical Engineering* 1997, vol. 4, 196 – 208.
23. S. Gabran, Results of micro-electrodes survey, University of Waterloo Medical Instrumentation Analysis and Machine Intelligence M IAMI, 2005.
24. Griss, P., Tolvanen-Laakso, H.K., Merilainen, P., Stemme, G., Characterization of micromachined spiked biopotential electrodes, *IEEE Transactions on Biomedical Engineering* 2004, vol. 49, 597 – 604.
25. S. R. I. Gabran, E. F. El-Saadany, M. M. A. Salama, Narcolepsy Assistive Device, *European Conference on Emergent Aspects in Clinical Data Analysis EACDA* 2005.
26. S. Aronson, L. A. Geddes, Electrode potential stability, *IEEE transactions on biomedical engineering BME 1985,* 987-988.

27. N. F. Hodge, 1/f noise in the conductance of ions in aqueous solutions, *Physiology letter* 1970, vol. 33, 987-988.
28. P. Griss, P. Enoksson, HK Tolvanen-Laakso, P. Merilainen, S. Ollmar, and G. Stemme, Micro-machined Electrodes for Bio-potential Measurements, Journal of Microelectromechanical Systems MEMS 2001.
29. Peter L. Williams, Roger Warwick, Mary Dyson, Lawrence H. Bannister, *Gray's anatomy*, Churchill livingstone, 1989.
30. J. Robert McClintic, *Human anatomy*, Mosby 1983.
31. S. Henry,D.V. McAllister,M.G. Allen, and M. R. Prausnitz, Micro-machined Needles for the Transdermal Delivery of Drugs, *11th Annual International Conference on Micro Electro Mechanical Systems* 1998, 494–497.
32. Griss, P., Enoksson P., Tolvanen-Laakso H., Merilainen P., Ollmar S., Stemme G., Spiked bio-potential electrodes, *The 13th Annual International Conference on Micro Electro Mechanical Systems MEMS* 2000, 323-328.
33. S. Grimnes and O. G. Martinsen, *Bio-impedance and bioelectricity basics*, Academic press 2000.
34. , Gerard J. Tortora, *Principles of human anatomy*, John Wiley and Sons 1998.
35. Kent M. Van De Graaff, *Human anatomy*, W. C. Brown Publishers 1984.
36. Eyuboglu B. M., Pilkington T. C., Wolf P. D., Estimation of tissue resistivities from multiple-electrode impedance measurements, *Physics in medicine and biology* 1994.
37. Adams T., and J. A. Vaughan, Human eccrine sweat gland activity and palmar skin resistance., *Journal of Applied Physiology* 1965, 980-983.
38. Caton J. R., P. A. Mole, W. C. Adams, D. S. Heustis, Composition analysis by bioelectrical impedance: effect of skin temperature, *Medical Science Sports Exercise* 1998, 489-491.
39. Missenard, F. A., Temperature moyenne de la peau humaine en fonction de l'ambiance, Archives des Sciences Physiologiques 1973, 45-50.
40. Smith, D. C. E., Effects of skin blood flow and temperature on skin-electrode impedance and offset potential: measurements at low alternating current density, *Journal of Medical Engineering Technology* 1992, 112-116.
41. A Searle and L Kirkup, Real time impedance plots with arbitrary frequency components, Department of Applied Physics, University of Technology, Sydney, Australia.
42. D. K. Swanson and J. G. Webster, *Biomedical Electrode Technology*, Academic Press 1974, 117-128.
43. Javier Rosell, Josep Colominas, Pere Riu, Ramon Pallas-Areny, John G. Webster, Skin impedance from 1 Hz to 1 MHz, *IEEE Transactions on Biomedical Engineering* 1988, 649-651.
44. Thomas C. Ferreea, Phan Luua, Gerald S. Russella, Don M. Tucker, Scalp electrode impedance, infection risk, and EEG data quality, Clinical Neurophysiology 2001, 536-544.
45. Webster, *Medical instrumentation application and design*, Wiley 1998.

46. Rush S., Driscoll D. A., EEG-electrode sensitivity - An application of reciprocity. *IEEE Transactions in Biomedical Engineering BME* 1969, 15-22.
47. Barber D. C., Brown B. H., Applied potential tomography, Journal of Physics Engineering 1984, 723-33.
48. Geddes LA, Sadler C, The specific resistance of blood at body temperature. Medical and Biological Engineering 1969, 336-339.
49. Plonsey R., *Bioelectric Phenomena*, McGraw-Hill 1969.
50. Rush S, Abildskov JA, McFee R, Resistivity of body tissues at low frequencies. *Circulation research*, 40-50.
51. Epstein B. R., Foster K. R., Anisotropy in the dielectric properties of skeletal muscle. *Medical & biological engineering & computing* 1983, 51-55.
52. Geddes L. A., Baker L. E., The specific resistance of biological material - A compendium of data for the biomedical engineering and physiologist, Medical *& biological engineering* 1967, 271-293.
53. Saha S, Williams PA, Electric and dielectric properties of wet human cortical bone as a function of frequency, *IEEE Transactions on Biomedical Engineering* 1992, 1298-1304.
54. Anderson J. M., Langone J. J., Issues and perspectives on the biocompatibility and immunotoxicity evaluation of implanted controlled release systems, *Journal of Control* 1999, 107–113.
55. G. Voskerician, M. S. Shive, R. S. Shawgo, H. von Recum, Biocompatibility and biofouling of MEMS drug delivery devices, *Biomaterials* 2003, 2405-2412.
56. Spector M., Cease C., Tong-Li X., The local tissue response to biomaterials, *Critical Reviews in Bio-Compatibility* 1989, 269–295.
57. Wokalek H., Ruh H., Biological response to materials, Journal of Biomaterial Applicaitons 1991, 337–362.
58. Titanium alloys in surgical implants, Luckey / Kubi, editors, ASTM special technical publications, 1981
59. Bothe R. T., Beaton L. E., Davenport H. A., Reaction of bone to multiple metallic implants, *Surgical Gynecology and Obstetrics* 1940, chapter 71, 598-602
60. Jonathan Black, *Biological performance of materials*, Marcel Dekker.
61. Titanium alloys for biomaterial application: an overview, Bannon, B. P., and Mild, E. E., Titanium alloys in medical implants, ASTM STP 796, H. A. Luckey and Fred Kubli, Jr., Eds., American Society for Testing and Materials, 1983, pp. 7-15
62. Griss, P.; Enoksson, P.; Tolvanen-Laakso, H.; Merilainen, P.; Ollmar, S.; Stemme, G., Spiked biopotential electrodes, *The Thirteenth Annual International Conference on Micro Electro Mechanical Systems MEMS* 2000, 323-328.
63. Clifford D. Ferris, *Introduction to bio-electrodes*, Plenum press, 1974
64. Measurement and analysis of monophasic action potentials using fractally coated electrodes, *Biomedizinische Technik Biomedical engineering* 1971, 160-167.
65. K. T. Oh, H. M. Shim, K. N. Kim, Properties of titanium-silver alloys for dental application, *Journal of Biomedical Materials Research* 2005.

66. Anja Metzger, Biocompatibility of silver-modified polyester for antimicrobial protection of prosthetic valves Biocompatible coatings on titanium implants, Restore Medical Inc.
67. Leventhal G. S., Titanium, a metal for surgery, *Journal of bone and joint surgery* 1951, pp. 473.
68. Laing, P. G., Furguson, A. B., Hodge, E. F., Biomedical materials in surgery, *Biomedical materials research* 1960, Vol. 1, pp. 135
69. Rhinelander, F. W., Journal *of biomedical materials research*, John Wiley & Sons 2004.
70. Turner J. N., Shain W., Szarowski D. H., Anderson M., Martins S., Isaacson M., Craighead H., Cerebral astrocyte response to micromachined silicon implants, Exp Neurol 1999; p. 33–49.
71. Edell D. J., Toi V. V., McNeil V. M., Clark L. D., Factors influencing the biocompatibility of insertable silicon microshafts in cerebral cortex, *IEEE Transactions in Biomedical Engineering* 1992; p. 635–643.
72. Dario P., Carrozza M. C., Benvenuto A., Menciassi A., Microsystems in biomedical applications, *Journal of Micromechanical Micro-engineering* 2000, p.235–244.
73. http://www.argentumsolutions.com
74. Douglas J. Wood, *The Characterization of Particulate Debris Obtained from Failed Orthopedic Implants*, San José State University, College of Materials Engineering, Spring 1993
75. Thomas A. Horbett, Biological Activity of Adsorbed Proteins And Biocompatibility, *Journal of Biomaterials Science, Polymer Edition* 2002, 367-390.
76. T.A. Horbett, Protein adsorption on biomaterials in biomaterials: Interfacial phenomena and applications, *American chemical society* 1982.
77. M.Stelzle, R. Wagner, W. Jagermann, R. Frohlich, Ultrathin organic films for biocompatible low impedance pacemaker electrodes, *Proceedings of the 18th annual international conference of the IEEE on bridging disciplines for biomedicine*, vol. 1, 1997, p.114.
78. Turner J. N., Shain W., Szarowski D. H., Anderson M., Martins S., Isaacson M., Craighead H., Cerebral astrocyte response to micromachined silicon implants, *Experimental neurology* 1999, 33–49.
79. Edell D. J., Toi V. V., McNeil V. M., Clark L. D., Factors influencing the biocompatibility of insertable silicon microshafts in cerebral cortex, *IEEE Transactions on Biomedical Engineering* 1992, 635–643.
80. Dario P., Carrozza M. C., Benvenuto A., Menciassi A., Microsystems in biomedical applications, Journal of Micromechanical Micro engineering 2000, 235–244.
81. Y. Vickie Pan, Yael Hanein, Deborah Leach-Scampavia, Karl F. Böhringer, Buddy D. Ratner, Denice D. Denton, A precision technology for controlling protein adsorption and cell adhesion in bioMEMS, *The 14th IEEE International Conference on Micro Electro Mechanical Systems* 2001, 435 – 438.
82. B. D. Ratner and A. S. Hoffman, Thin Films Grafts, and Coatings, *An Introduction to Materials in Medicine,* Academic Press 1996.
83. H. Ma, J. Hyun N. Nath, A. Chilkoti, Surface engineering strategies for control of protein and cell interactions, *European Conference on Cells and Materials* 2003, vol. 6, pp. 16.
84. Y. Vickie Pan, Yael Hanein, Deborah Leach-Scampavia, Karl F. Böhringer, Buddy D. Ratner, Denice D. Denton, Micromachining of Non-fouling Coatings for Bio-MEMS Applications, *Sensors and Actuators* 2001.
85. Lipscomb R. C., Clemmens J., Hanein Y., Holl M. R., Vogel V., Ratner B. D., Denton D. D., Bohringer K. F., *2nd Annual International IEEE-EMB Special Topic Conference on Microtechnologies in Medicine & Biology 2002*, 21–26.
86. Elbert D. L., Self-assembly and steric stabilization at heterogeneous biological surfaces using adsorbing block copolymers, *Chemistry and Biology* 1998, 177-183.
87. J. M. Harris, *Poly-ethylene glycol chemistry, Bio-technical and bio-medical applications*, Plenum 1992.
88. Sharma S., Johnson R. W., Desai T. A., Poly(ethylene glycol) interfaces for the control of biofouling in silicon-based Microsystems, *2nd Annual International IEEE-EMB Special Topic Conference on Microtechnologies in Medicine & Biology* 2002, 41–45.

89. Y. V. Pan, Y. Hanein, D. Leach-Scampavia, Plasma-polymerized coatings for bio-MEMS applications, *Journal of Sensors and Actuators* 2001, 49-54.
90. G. P. Lopez, B. D. Ratner, C. D. Tidwell, C. L. Haycox, R. J. Rapoza and T. A. Horbett, Glow Discharge Plasma Deposition of Tetraethylene Glycol Dimethyl Ether for Fouling-Resistant Biomaterial Surfaces, *Journal of Biomedical Materials* 1992.
91. M. N. Mar, B. D. Ratner, and S. S. Yee, An Intrinsically Protein-Resistant Surface Plasmon Resonance Biosensor Based Upon a RF-Plasma-Deposited Thin Film, *Sensors Actuators* 1999.
92. H. B. Lu, J. Homola, Y. V. Pan, B. D. Ramer, C. T. Campbell, and S. S. Yee, Surface Functionalization for Self-referencing Surface Plasmon Resonance Biosensors by RF-plasma-deposited Thin Films and Self-assembled Monolayers, *Society for Biomaterials Transactions of the 6th World Biomaterials Congress* 2000, p.151.
93. K. F. Böhringer, Surface Modification and Modulation in Microstructures: Controlling Protein Adsorption, Monolayer Desorption, and Micro-Self-Assembly, *Journal of Micromechanical Microengineering* 2003.
94. Boyce, J., Dobkin, D., Drysdale, R. and Guibas, L., Finding External Polygons, *Society of Industrial and Applied Mathematics SIAM .Journal of Computatiing SICOMP* 1985, vol 14, 134–147.
95. Shankar Chandrasekaran, Bruno Fraizer, Characterization of surface micromachined metallic microneedles, *Journal of Microelectromechanical Systems* 2003, vol. 12, 289–295.
96. S. Henry, D. V. McAllister, M. G. Allen, M. R. Prausnitz, Micromachined needles for the transdermal delivery of drugs, *The 11th Annual International Workshop on Micro Electro Mechanical Systems* 1998, 494–498.
97. H. Kim, *Fabrication and analysis of plastic hypodermic needles by micro injection molding*, masters thesis, Georgia Institute of technology, 2004.
98. J. M. Gere, S. P. Timoshenko, *Mechanics of Materials*, Stanley Thornes Ltd 1999.
99. Joseph Edward Shigley, *Mechanical Engineering Design*, McGraw Hill 2001.
100. H. Kim, J. S. Colton, Fabrication and analysis of plastic hypodermic needles, *Journal of Medical Engineering & Technology* 2005, Taylor & Francis, Volume 29.
101. A. Perez-Duarte, S. van der Veen, Pechiney Rhenalu, Issoire, France; R. Muzzolini and J. Ehrstrom, On Material Models for Static Sizing of Compression Driven Airframe Structure, *43rd AIAA/ASME/ASCE/AHS/ASC Structures, Structural Dynamics, and Materials Conference*, 2002
102. R. C. Hibbler, *Mechanics of Materials*, Macmillan 1991.
103. Fabrication and analysis of plastic hypodermic needles by micro injection molding, H Kim, Masters thesis, Georgia Institute of technology, 2004
104. George V. Smith, *Metallurgy and metallurgical engineering series, properties of metals at elevated temperatures*, McGraw Hill 1950.
105. metals1
106. metals2
107. metals3
108. Plastic design library, Fatigue and tribological properties of plastics and elastomers, 1995, pp. 325-327
109. Ansys Inc. Online help for Ansys Release 7.0 Theory reference, shape functions of 3D solids.
110. Hendricks F. M., Mechanical Properties of Different Layers of Human Skin, Dept. of Materials Technology, Eindhoben Univ. of Technology, http://www.bmt.tue.nl/pdf/postersonderzoekdag2001/fhendriks.pdf
111. Oomens, C. W. J., Deformation Analysis of a Supported Buttock Contact, Bioengineering Conference ASME 2001, Vol. 50.
112. F. M. Hendriks, D. Brokken, J. T. W. M. van Eemeren, C. W. J. Oomens, F. P. T. Baaijens, J. B. A. M. Horsten, A numerical experimental method to characterize the non-linear mechanical behaviour of human skin, *Skin Research and Technology* 2003.
113. Stephen K. Lower, *Electrochemistry*, Simon Fraser University.
114. McKenna, *Theoretical electrochemistry*, Macmillan and Co. 1939.
115. H. D. Abruña, *Electrochemical interfaces*, VCH Publishers 1991.
116. Donald Sawyer, Julian Roberts, *Experimental electrochemistry for chemists*, John Wiley and Sons 1974.
117. Allen Bard, Larry Faulkner, *Electrochemical methods*, John Wiley and Sons 1980.

118. R. Ruhmann, K. Pfeiffer, M. Falenski, F. Reuther, R. Engelke and G. Grützner, SU-8 - a high performance material for MEMS applications, MicroChem, www.microchem.com
119. Sang Jeen Hong, Seungkeun Choi, Yoonsu Choi, Allen M., May G. S., Characterization of low-temperature SU-8 photoresist processing for MEMS applications, *IEEE Conference and Workshop on Advanced Semiconductor Manufacturing ASMC* 2004, 404–408.
120. Jian L., Loechel B., Scheunemann H. U., Bednarzik M., Desta Y. M., Goettert J., Fabrication of Ultra Thick, Ultra High Aspect Ratio Microcomponents by Deep and Ultra Deep X-ray Lithography, International Conference on MEMS, NANO and Smart Systems 2003, 10-14.
121. NANO^{TM} SU-8 negative tone photoresist formulations 2-25, MicroChem, www.microchem.com
122. Roberts K., Williamson F., Cibuzar G., Thomas L., The fabrication of an array of microcavities utilizing SU-8 photoresist as an alternative `LIGA' technology, *Proceedings of the Thirteenth Biennial University/Government/Industry Microelectronics Symposium* 1999, 139-141.
123. Williamson F., Shields E. A., SU-8 as an electron beam lithography resist, *Proceedings of the 15th Biennial University/Government/Industry Microelectronics Symposium* 2003, 57-60.
124. J. Thaysen, A. D. Yalēinkaya, R. K. Vestergaard, S. Jensen, M. W. Mortensen, P. Vettiger, A. Menon, SU-8 based piezo-resistive mechanical sensor, *15th IEEE International Micro Electro Mechanical Systems Conference MEMS* 2002.
125. S. Gabran, E. F. El-Saadany, M. M. M. Salama, Hardware Design Phase of Portable Narcolepsy Assistive Device, *UW Medical instrumentation analysis and machine intelligence MIAMI Biomedical engineering workshop* 2005.
126. Ling Lin, Juliette Faraco, Robin Li, Hiroshi Kadotani, William Rogers, Xiaoyan Lin, Xiaohong Qiu,* Pieter J. de Jong, Seiji Nishino, and Emmanuel Mignot, The Sleep Disorder Canine Narcolepsy is Caused by a Mutation in the Hypocretin, Cell press, Vol. 98, 365–376, August 6, 1999.
127. Bruck D., The impact of narcolepsy on psychological health and role behaviours: negative effects and comparisons with other illness groups, *Sleep Medicine* 2001, vol. 2, 437-446.
128. National Institute of Neurological Disorders and Strokes
129. Beusterien K. M., Rogers A. E., Health-Related Quality of Life Effects of Modafinil for Treatment of Narcolepsy, *Sleep journal* 1999, vol. 6, 757-765.
130. Kellerman H., *Sleep Disorders: Insomnia and Narcolepsy*, Brunner/Mazel Inc. 1981.
131. Broughton W. A., Broughton R. J., Psychosocial Impact of Narcolepsy, *Sleep journal* 1994, vol. 17, 45-49.
132. Goswami M., The influence of clinical symptoms on quality of life in patients with narcolepsy, *Journal of Neurology* 1998, 31-36
133. Fry J. M., A portable device for alertness detection, Journal of Neurology 1998, 43-48.
134. Kirk B. P., LaCourse J. R., Vigilance monitoring from the EEG power spectrum with a neural network, *Proceedings of the 19th Annual International Conference of the IEEE Engineering in Medicine and Biology society 1997*, 1218–1219.
135. Amditis Á., Polychronopoulos Á., Bekiaris Å., Antonello P. C., System architecture of a driver's monitoring and hypovigilance warning system, Intelligent Vehicle Symposium 2002, 527-532.
136. Sharbrough F, Chatrian G. E., Lesser R. P., Lüders H., Nuwer M., Picton T. W., American Electroencephalographic Society Guidelines for Standard Electrode Position Nomenclature, *Journal of Clinical Neurophysiology* 1991, 200-202.
137. Bard and Faulkner, *Electrochemical Methods, Fundamentals and Applications*, Wiley 2000.
138. J. R. Macdonald, *Impedance Spectroscopy*, John Wiley, 1987.
139. L. A. Geddes, *Electrodes and the measurement of bio-electric events*, Wiley Interscience 1972.